DEVELOPMENT OF A COUPLED TWO-FLUID PLASMA GAS-KINETIC SCHEME (TFPGKS)

A Dissertation

by

STEVEN EDWARD ANDERSON

Submitted to the Office of Graduate and Professional Studies of
Texas A&M University
in partial fulfillment of the requirements for the degree of

DOCTOR OF PHILOSOPHY

Chair of Committee,   Sharath S. Girimaji
Committee Members,   Adonios Karpetis
                                      Kentaro Hara
                                      David Staack
                                      Christopher Pope
Head of Department,   Rodney Bowersox

May 2018

Major Subject: Aerospace Engineering

ABSTRACT

The study and characterization of plasma flows is of significant interest in many disciplines of engineering and science. Of particular interest is the study and development of plasma-based electric propulsion devices. Plasma flows can exhibit complex behavior depending upon parameter regime and the interaction with applied and induced electromagnetic fields. Further, due to their typically extreme environments, space plasma flows are difficult to investigate with terrestrial experiments. The complexity of plasma flow governing equations typically renders analytical solutions impossible for all but the simplest problems. Thus, the development of more capable physical models and numerical tools for computer simulation is an important research focus. Over the last two decades, the Gas-Kinetic Scheme (GKS) has been demonstrated to be a highly capable solver for a wide range of gas-dynamics flows, from incompressible to rarefied and hypersonic. Further, it has also been shown to work well for ideal, resistive, and Hall magnetohydrodynamics.

This dissertation aims to develop the theoretical framework for a gas-kinetic scheme for a singly-charged ion-electron two-fluid plasma. The approach is to apply a Method-of-Characteristics (MoC) – based solution to the Boltzmann equation for each species with the Bhatnagar-Gross-Krook (BGK) collision operator modeling the species self-collisions. In the Boltzmann-BGK (B-BGK) equation the inter-species collisions are modeled as a resistive force on each species. The derived approximate MoC solution renders the resulting particle characteristic trajectories linear in physical space. To model the non-equilibrium effects of collisions, a Chapman-Enskog (CE) type expansion for each species is performed, which captures Finite-Larmor-Radius (FLR) effects on the stress tensor and the heat flux. To consistently couple the ion and electron fluids to the electromagnetic fields, the Perfectly Hyperbolic Maxwell's (PHM) equations are used, which incorporate the constraints of Gauss' Law for the Electric and Magnetic Fields into their temporal evolution. The Two-Fluid Plasma GKS (TFPGKS) scheme is implemented by using Weighted Essentially-Non-Oscillatory

(WENO) interpolation for cell interface reconstruction of the flow variables, while a Lax-Friedrichs – type approach is used for the PHM equations. A semi-analytic analysis of the derived fluxes compared to existing models demonstrates the magnetized asymptotic behavior which produces the expected anisotropy in the transport properties. The scheme is benchmarked against analytic solutions for the linearized governing equations. It is further validated against published results for several canonical problems, including the Electromagnetic Shock and Ion Acoustic Solitons. Finally, a parametric study of collisional electromagnetic shocks demonstrates the capabilities of the new TFPGKS scheme over more naive previous implementations. Overall, the work demonstrates the promise of the GKS approach to simulating plasma flows over a wide parameter range.

DEDICATION

To my wife Katie.

ACKNOWLEDGMENTS

CONTRIBUTORS AND FUNDING SOURCES

Contributors

This work was supported by a dissertation committee consisting of Professors Sharath Girimaji, Adonios Karpetis, and Kentaro Hara of the Department of Aerospace Engineering, Professor David Staack of the Department of Mechanical Engineering, and Professor Christopher Pope of the Department of Physics & Astronomy.

All work conducted for this dissertation was completed by the student independently. Portions of Chapter 3 were developed during collaboration with Eduardo de Carli da Silva, Diogo Nardelli Siebert, and Juan Pablo Salazar at the Universidade Federal de Santa Catarina – Campus Joinville, in Joinville, SC, Brazil.

Funding Sources

TABLE OF CONTENTS

LIST OF FIGURES

LIST OF TABLES

1. INTRODUCTION

1.1 Motivation

The study of plasma physics and plasma dynamics is motivated largely by its abundance, making up the vast majority of visible matter in the universe. An increased understanding of plasma behavior leads to improved comprehension of many natural phenomena, from the behavior of stellar atmospheres and interstellar matter to the interactions between our own Sun and geomagnetic fields. Investigating plasma phenomena lends us greater understanding of a wide variety of plasma applications in engineering and physics, from the development of fusion power generation via magnetic or inertial confinement to the application of plasmas to medical settings.

In particular, there has been extensive investigation into the use of plasma as propellant for electric spacecraft propulsion systems, ranging from ion and Hall thrusters to magnetoplasmadynamic thrusters to more compliciated plasma thruster systems. Specifically, we will look at the Variable Specific Impulse Magnetoplasma Rocket (VASIMR$^{\circledR}$ [7]) as an example system of interest. In the VASIMR$^{\circledR}$ system, thrust is produced by a plume of heated plasma which expands through a rocket nozzle formed from a diverging magnetic field [8]. An example of the VASIMR$^{\circledR}$ rocket plume under testing is shown in Figure 1.1, reprinted from [1]. A schematic depiction of the magnetic field lines (not to scale) is shown in red over the plasma plume. Of particular interest is the effect of the magnetic field on the transport of momentum and energy within the plasma plume. To determine the degree of these effects, we may investigate the parametric regimes within the VASIMR$^{\circledR}$ plume at the locations marked "1" and "2" in Figure 1.1, which is discussed in the next section.

1.2 Plasma Regimes

The dynamics of plasma flows is highly complex, involving transport of mass, momentum, and energy of many different particle species coupled with magnetic and electric fields.
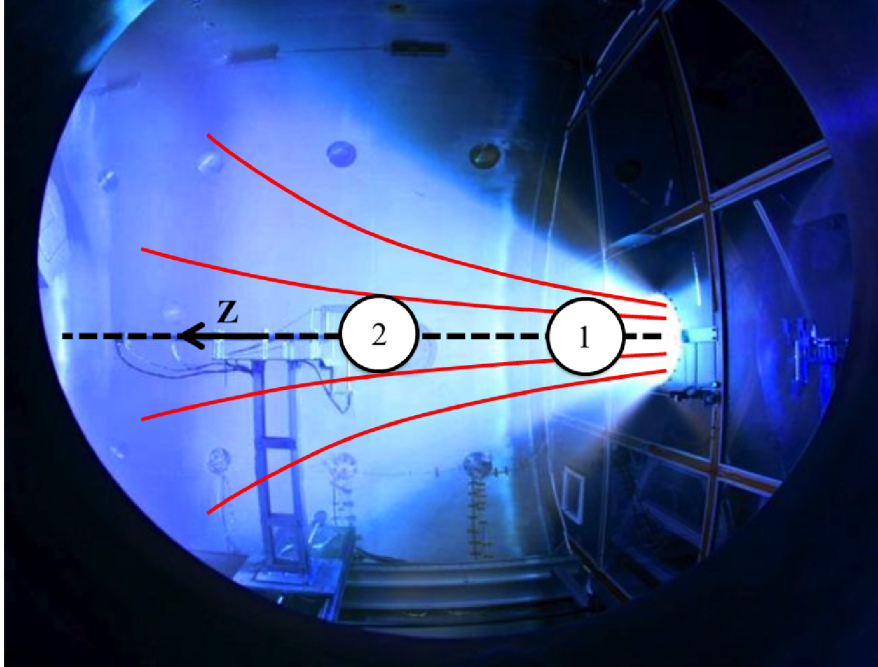
Figure 1.1: VASIMR® rocket engine plume. Reprinted and modified from Araya [1]

There are many factors which effect the behavior of space plasma flows. These range from the number of individual species present – and their particle charge and mass – to the degree of rarefaction and heating they experience. The parametric range wherein plasmas are defined may span many orders of magnitude – as many as 10^{25} cm^{-3} in particle number density and 10^7 eV in temperature [9]. To characterize plasma flow regimes we first introduce the Knudsen number Kn which characterizes the degree of rarefaction for the gas, or the degree to which collisional transport affects the flow. The Knudsen number is defined $Kn \equiv \frac{\lambda}{L}$. L is the characterized size or length of the system being considered, and $\lambda \equiv v_{th}\tau$ is the mean free path which characterizes the distance particles travel before being perturbed by collisions. Thus, the Knudsen number is equivalent to the normalized mean free path $\hat{\lambda}$. In defining the mean free path, we introduce the thermal velocity v_{th} and the collision time τ. The thermal velocity v_{th} is the characteristic speed of particles in the plasma and is related to the plasma temperature T and particle mass m by $v_{th} \equiv \sqrt{\frac{kT}{m}} - k$ being the Boltzmann constant. The collision time τ is the characteristic time between particle collisions.

The Larmor radius r_L and cyclotron frequency ω_c are parameters which characterize the length- and time-scales of the effect of electromagnetic (EM) fields on the plasma. The cyclotron frequency characterizes the frequency at which particles orbit around magnetic field lines and is defined as $\omega_c \equiv \frac{qB}{m}$. In defining ω_c, B is the magnetic field strength, while q and m are the particle charge and mass, respectively. The Larmor radius is defined $r_L \equiv v_{th}\omega_c^{-1}$, and represents the characteristic radius of gyration for particles around magnetic field lines.
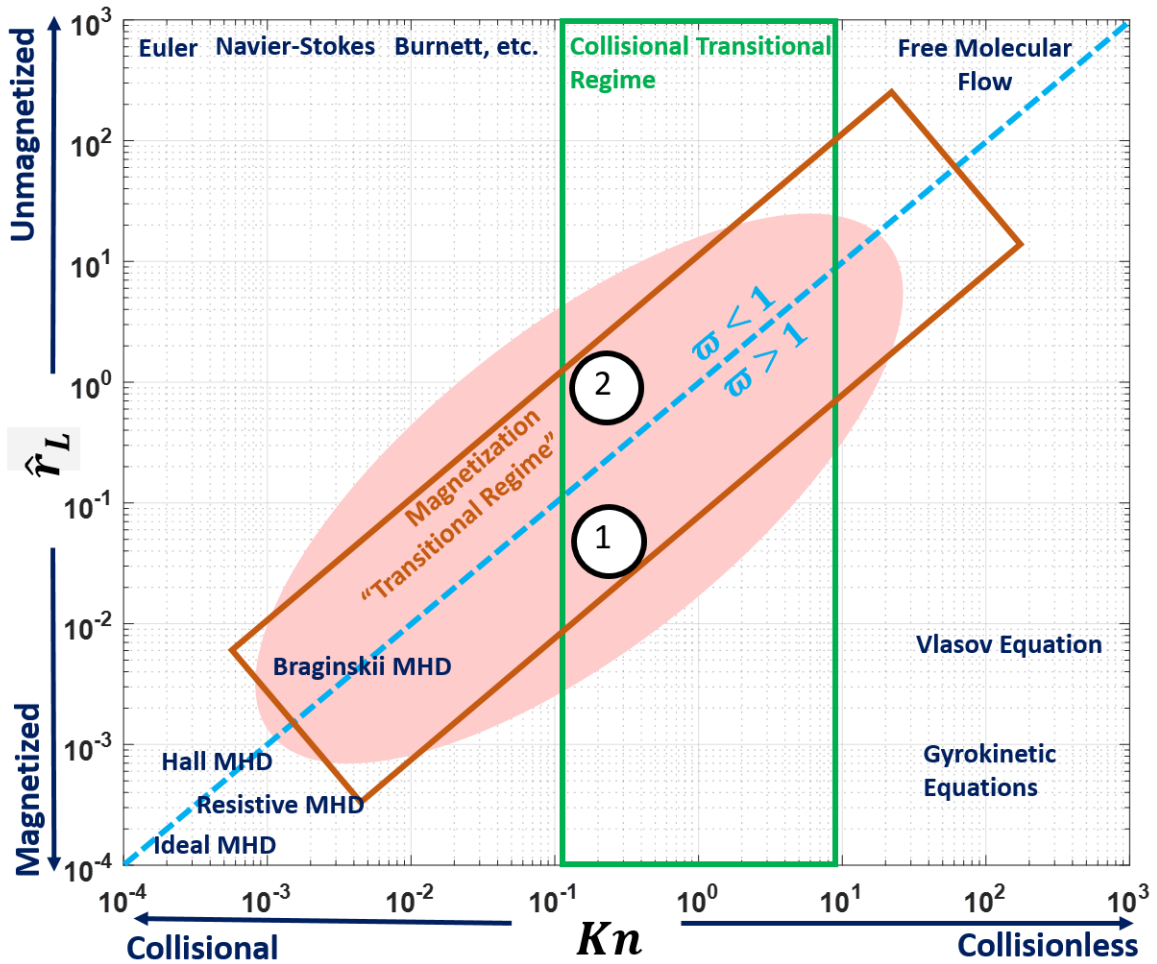
Figure 1.2: Plasma flows parametrized by normalized Larmor radius, Knudsen number, and Hall parameter

Figure 1.2 depicts a breakdown of some plasma flow regimes by Kn on the x-axis and normalized Larmor radius $\hat{r}_L \equiv \frac{r_L}{L}$ on the y-axis. However, while the Knudsen number is useful in determining the degree of collisional transport in a gas or plasma, the normalized Larmor radius alone is not enough to usefully determine the effects of the electromagnetic field on plasma transport. Thus, we will introduce the Hall parameter ϖ which characterizes the "competition" between the magnetic field and collisions in determining transport behavior for a gas. The Hall parameter may be defined as the ratio between the Knudsen number and normalized Larmor radius: $\varpi \equiv \frac{\hat{\lambda}}{\hat{r}_L}$. This is equivalent to the product of cyclotron frequency ω_c and collision time τ – i.e. $\varpi = \tau\omega_c$. In the limit $\varpi \ll 1$, the transport is unaffected entirely by the magnetic field, while in the limit $\varpi \gg 1$ the transport is magnetic field dominated in the directions perpendicular to the field, but not along it. This leads essentially to *anisotropy* of properties which would normally by isotropic. In Figure 1.2, the dashed blue line indicates the line of $\varpi = 1$, with $\varpi > 1$ below and $\varpi < 1$ above.

The most accurate representation of plasma flows involves solving for the position and velocity of each particle (or "super-particle") as it is affected by any applied electromagnetic fields as well as the induced fields resulting from all other particles (which are in turn evolved via Maxwell's equations). This is a daunting task, and essentially impossible except in the region to the far upper right of Figure 1.2, where we have essentially free molecular flow. For highly magnetized but collisionless flow near the lower right of Figure 1.2, the collisionless Vlasov or gyrokinetic equations may be used. For the regimes to the right on this figure, we may also consider the collective behavior of the particles of each species, from which a particle distribution function may be obtained which describes the probability density of particles in phase space. The spatio-temporal evolution of the distribution function is governed by first-principles gas-kinetic equations, such as the Boltzmann, Vlasov, or Fokker-Planck equations.

We can see that in the unmagnetized and highly collisional regime to the upper left we have the hydrodynamic fluid equations, from the Euler equations in the limit of $Kn \to 0$,

to the Burnett equations as we increase the collision time. In the limit of $Kn \to \infty$ and $\hat{r}_L \to \infty$, we have essentially free molecular flow, where the motion of individual molecules or atoms is of interest. In the highly collisional and highly magnetized regime, we have the various MHD fluid equations. These equations may be obtained from the kinetic – e.g., Boltzmann – equations through moments in velocity space to obtain single- or multi-fluid models, which produce a set of fluid equations for conserving mass, momentum, and energy.

The green and orange boxed regions which intersect the center of the chart are the "transitional" regimes of collisional and magnetized plasma flow and mark where the transport properties are significantly modified from the asymptotic limits at either end of the x- and y-axes. If we map the points "1" and "2" from the VASIMR® plume in Figure 1.1 on our chart in Figure 1.2, we see they reside in this area. Thus, we will broadly denote the ellipsoidal area highlighted in the center of Figure 1.2 as our "focus area" for this work.

Due to the complexity of the governing equations, purely analytical solutions of mathematical models governing plasma behavior are only possible for the simplest systems. While these fill a very important place in providing a starting point or order-of-magnitude estimate for many analyses, full understanding of system behavior requires a more in-depth exploration. However, due to their extreme nature, many space plasma systems are extremely difficult and expensive to study experimentally. As a result, developing numerical schemes for computing plasma flow behavior is an important engineering challenge. Due to the extremely wide range of plasma parameters and regimes of interest, there is a correspondingly wide range of governing models and schemes to solve them. Each approach involves a compromise among accuracy, speed/efficiency, fidelity, and complexity.

1.2.1 Advantages of GKS and Rationale for Further Development

In recent years, the gas-kinetic scheme (GKS) or gas-kinetic method (GKM) has shown promise as a compressible flow solver for fluid equations such as Euler, Navier-Stokes, Burnett, and Super-Burnett. The primary motivation for seeking to apply GKS to the Two-Fluid Plasma system is that it provides several advantages over other flow solvers. This is partic-

ularly true for high-Mach-number compressible and shocked flows when compared to traditional Riemann solvers, upwinding techniques, Godunov schemes, or Flux-Vector Splitting approaches. Kumar [10] provides a fairly comprehensive overview of the advantages of GKS. For a given species, all of the flow variables pertaining to that species are derived from a single distribution function, and are not directly based on the Navier-Stokes (NS) or Euler equations [10, 11, 12]. The Boltzmann equation has a much wider range of validity than the NS-type fluid equations. As a consequence GKS, which is based on the Boltzmann equation, has the potential to be valid for a much wider range of flows than strictly continuum-based fluid solvers. To date, GKS has demonstrated capability for both highly compressible flows [13] as well as incompressible flows [14]. Further, it has been extended to multi-fluid applications [15, 16] including reacting flows [17].

GKM has been used in the past for ideal magnetohydrodynamics (MHD) schemes [18, 19, 20], as well as a non-ideal/Hall MHD scheme [21]. However, these implementations have been performed either as direct flux-splitting schemes based on the explicit ideal MHD fluxes – such as in the case of Xu [18] and Tang and Xu [19, 20] – or have omitted the effect of the electromagnetic acceleration in the solution of the characteristic solution for calculating the numerical flux – such as in the case of Araya et al. [21]. Further, these schemes are incapable of recovering any finite-Larmor-radius (FLR) effects on heat flux and stress due to magnetization of the plasma. If the plasma is considered to be an ionized gas, our perspective is something like that depicted in Figure 1.3, where the effects of finite collisionality on the continuum may be significantly affected by the presence and influence of the electromagnetic fields. In Figure 1.3, the collisional effects are once again represented by the Knudsen number Kn. At the limit $Kn \rightarrow 0$ the problem is purely continuum, while at the limit $Kn \rightarrow \infty$ the problem is collisionless and purely kinetic. For the upper line in Figure 1.3 significant progress has already been made for both the near-continuum region (GKS) as well as the near-collisionless/transitional regime (UGKS) [22, 23, 24]. However, for the lower line where the effects of the electromagnetic fields – particularly the effects

6
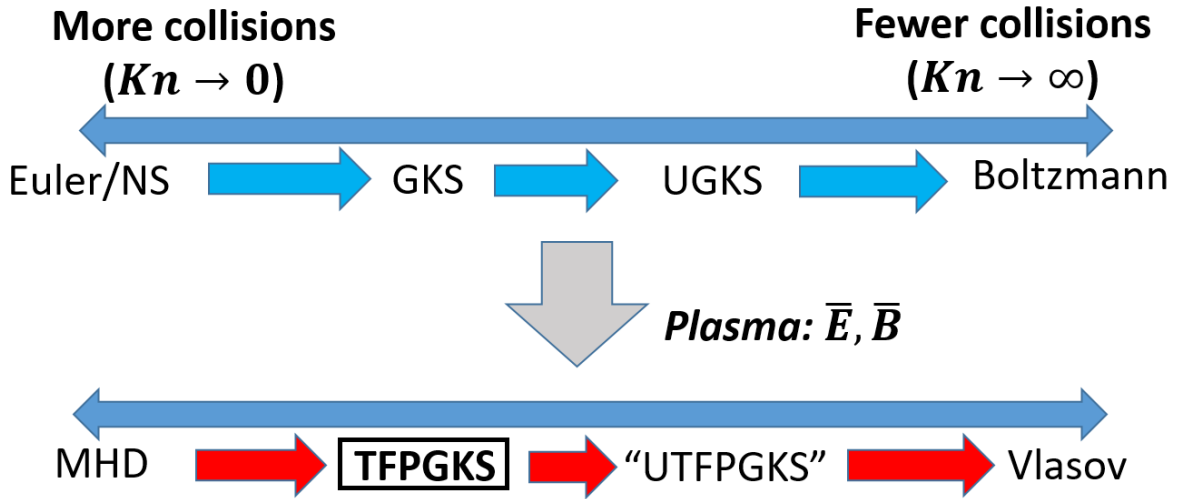
Figure 1.3: Conceptualization of a plasma flow regimes from an ionized gas perspective

of magnetization on transport – much work remains. For this dissertation, our objective is to enhance the GKS formulation to incorporate the effects of the electromagnetic fields (on charged species) and inter-species collisions, forming the Two-Fluid Plasma Gas-Kinetic Scheme (TFPGKS). In doing this, our aim is to develop a consistent and rigorous framework for extension of the UGKS platform to obtain a scheme which is fully applicable to the intersection of the transition regimes of Figure 1.2, which may be termed the "Unified Two-Fluid Plasma Gas-Kinetic Scheme" ("UTFPGKS").

1.3 Dissertation Scope

The primary objective of this dissertation is to develop the theoretical framework for applying the gas-kinetic scheme to a two-fluid plasma of singly-charged positive ions and electrons. A basic implementation is performed in one spatial dimension and the underlying theory and basic numerical soundness of the scheme are validated. Broadly, this work is broken into three primary foci.

In the first part, the theoretical framework of the enhanced gas-kinetic scheme is given in detail. The approach starts from a Method-of-Characteristics (MoC) based representation for the solution of the gas distribution from the Boltzmann equation with the Bhatnagar-Gross-

Krook (BKG) collision operator and incorporates a Chapman-Enskog type expansion for the non-equilibrium component of the gas distribution in a magnetized plasma. In particular, this differs from previous GKS developments for MHD in the way in which the external forces are incorporated within the MoC solution. An analysis of the resulting GKS solution for the time-dependent gas distribution is performed, and the resulting analytic expressions for the macroscopic fluxes are given in detail.

In the second part we describe the considerations necessary to implement the GKS flux calculation framework developed in Part 1 into an efficient numerical scheme. This includes addressing the reconstruction of the discretized fluid variables for use in the discrete GKS flux calculation, as well as considerations for the consistent co-evolution of the electromagnetic fields via a perfectly hyperbolic expression of the Maxwell's equations. Discretization of Maxwell's equations and treatment of the source terms for both the electromagnetic fields and fluid variables are discussed.

The third and final part encompasses the application of the numerical scheme. We present numerical studies to verify the proof-of-concept for the two-fluid plasma gas-kinetic scheme (TFPGKS). These include zero-dimensional analysis of the effective constitutive relationship compared to models from the literature, as well as comparison to analytic solutions of the linearized system of equations. In addition, we compare to published computational results in the literature. A basic parametric study of viscous and resistive electromagnetic shocks is performed to demonstrate some of the physics-capturing capabilities of the scheme.

1.4 Dissertation Organization

The rest of this dissertation is organized as follows: Chapter 2 presents a discussion of the governing equations for plasma flow. In Chapter 3, the theory behind the gas-kinetic scheme is discussed, and the development of the theory behind the enhanced gas-kinetic scheme is presented. Details of the numerical implementation of the TFPGKS scheme and the Maxwell's equations are given in Chapter 4. Chapter 5 presents a benchmark comparison of the TFPGKS scheme to analytic solutions of the linearized governing equations. Chapter

6 presents numerical tests to validate the enhanced two-fluid plasma gas-kinetic scheme, as well as a parametric study for application of the new scheme to collisional electromagnetic shocks. Finally, a summary of the work, conclusions, and recommendations for future work are given in Chapter 7.

2. GOVERNING EQUATIONS

2.1 The Boltzmann Equation

The kinetic Boltzmann equation represents the evolution of a single particle distribution function for a single gaseous species. It may be taken to be the fundamental governing equation for the plasma system. The distribution f evolves in phase space and time as

$$\frac{\partial f}{\partial t} + \boldsymbol{\xi} \cdot \frac{\partial f}{\partial \boldsymbol{x}} + \boldsymbol{a} \cdot \frac{\partial f}{\partial \boldsymbol{\xi}} = \left(\frac{\partial f}{\partial t}\right)_{collsions}. \tag{2.1}$$

In equation (2.1), t is time, $\boldsymbol{x}$ is the spatial coordinate, and $\boldsymbol{\xi}$ is the microscopic particle velocity. The quantity $\boldsymbol{a}$ is the particle acceleration due to external forces. Equation (2.1) is the most generic form for the single-species Boltzmann equation. The left-hand side (LHS) represents the total derivative of the distribution f in time $- \frac{df}{dt}$. This is represented by the partial gradient of f with respect to time summed with the advection of f in physical space (due to particle motion) and in velocity space (due to external forces). The term on the right-hand side (RHS) represents the action of collisions between particles effecting changes in f (which includes both collisions between like particles, and any other species). For a plasma, with charged particles in external electric ($\boldsymbol{E}$) and magnetic ($\boldsymbol{B}$) fields, with negligible gravitational effects, the third term on the LHS becomes

$$\boldsymbol{a} = \frac{q}{m}\left(\boldsymbol{E} + \boldsymbol{\xi} \times \boldsymbol{B}\right), \tag{2.2}$$

where q is the signed particle charge and m is the particle mass. Note that here $\boldsymbol{E}$ and $\boldsymbol{B}$ represent the mean electric and magnetic fields. The explicit electric fields between individual particles and magnetic fields generated by movement of individual particles are assumed

to be averaged into $\boldsymbol{E}$ and $\boldsymbol{B}$, which are calculated from e.g., Maxwell's equations.

$$\frac{\partial f}{\partial t} + \boldsymbol{\xi} \cdot \frac{\partial f}{\partial \boldsymbol{x}} + \frac{q}{m}\left(\boldsymbol{E} + \boldsymbol{\xi} \times \boldsymbol{B}\right) \cdot \frac{\partial f}{\partial \boldsymbol{\xi}} = \left(\frac{\partial f}{\partial t}\right)_{collisions} \tag{2.3}$$

A separate version of equation (2.3) must be considered for each species in the plasma. However, a simplified model which is applicable to a wide variety of problems is to reduce our system to that of a two-fluid plasma, wherein we only have electrons and a single ion species (for simplicity the ions considered herein are singly charged).

Equation (2.3) represents a 6-dimensional system for each species (three in physical space and three in velocity space). To reduce the dimensional complexity, the system may be simplified by reducing to a set of fluid equations for each species, via appropriate moments in velocity space (e.g., $\int \theta f d\boldsymbol{\xi}$) of each species' governing Boltzmann equation.

$$\int_{-\infty}^{\infty} (m)\, f d\boldsymbol{\xi} = \rho \tag{2.4}$$

$$\int_{-\infty}^{\infty} (m\boldsymbol{\xi})\, f d\boldsymbol{\xi} = \rho\boldsymbol{u} \tag{2.5}$$

$$\int_{-\infty}^{\infty} \left(m\frac{1}{2}\boldsymbol{\xi}^2\right) f d\boldsymbol{\xi} = \varepsilon = \frac{1}{2}\rho\boldsymbol{u}^2 + \frac{p}{\gamma - 1} \tag{2.6}$$

Equations (2.4)-(2.6) represent moments of $\theta = m[1, \boldsymbol{\xi}, \frac{1}{2}\boldsymbol{\xi}^2]$, which produce the fluid quantities of mass density (ρ), momentum ($\rho\boldsymbol{u}$), and energy (ε, kinetic + internal). The internal energy is determined by the pressure p and the ratio of specific heat γ.

For the current work, the Boltzmann equation will be used with the Bhatnagar-Gross-Krook (BGK) collision operator, which was first proposed in 1954 [25].

$$\left(\frac{\partial f_\alpha}{\partial t}\right)_{C,\alpha\alpha} \equiv \frac{g_\alpha - f_\alpha}{\tau_{\alpha\alpha}} \tag{2.7}$$

Equation (2.7) depicts the BGK collision operator model for self-collisions within a species α. The BGK collision operator is not derived from the Boltzmann collision operator – see

equation (2.3) – and is instead essentially an "first-order" phenomenological model for the collisional relaxation process.

$$\left(\frac{\partial f}{\partial t}\right)_{C,\alpha\alpha} = \int \int [f_\alpha(\boldsymbol{\xi}')f_\alpha(\boldsymbol{\xi}_1') - f_\alpha(\boldsymbol{\xi})f_\alpha(\boldsymbol{\xi}_1)] \, \sigma(|\boldsymbol{\xi} - \boldsymbol{\xi}_1|, \Omega)d\Omega d\boldsymbol{\xi}_1 \qquad (2.8)$$

Equation (2.8) describes collisions between particles of velocities $\boldsymbol{\xi}$ and $\boldsymbol{\xi}_1$ which have velocities $\boldsymbol{\xi}'$ and $\boldsymbol{\xi}_1'$ after the collision process, which is described by the cross-section σ. The general Boltzmann collision operator and other general collision operators derived from it – e.g., Fokker Planck or Coulomb collision operators – are highly complex and for many applications are not tractable.

Thus, we turn to the much simpler BGK collision operator – equation (2.7) – which essentially describes the relaxation of f_α towards the equilibrium distribution g_α over some characteristic "collision time" $\tau_{\alpha\alpha}$. Despite its ad-hoc nature, the BGK operator is known to approach g_α at equilibrium, produce the correct moments of equation (2.1), and satisfy the H-theorem [26]. However, it does have some shortcomings, notably that it assumes a Prandtl number $Pr = 1$ – i.e. that the characteristic time for diffusion of momentum and thermal energy are the same. The Prandtl number is defined $Pr \equiv \frac{\mu c_p}{\kappa}$, where μ is the viscosity, c_p is the specific heat, and κ is the thermal conductivity. Further, it does a poor job of describing the collisional relaxation of higher moments [27]. However, it should prove adequate for a flows where the distribution is not too far from a Maxwellian, such as flows in the near-continuum regime and some low-speed rarefied flows [28, 29, 30].

To model the inter-species collisions, a simple "Stokes'-Drag" type model, wherein the interspecies collision operator is modeled as a drag force proportional to the bulk velocity differential between species:

$$\left(\frac{\partial f}{\partial t}\right)_{C,\alpha\beta} \equiv \frac{\boldsymbol{u}_\beta - \boldsymbol{u}_\alpha}{\tau_{\alpha\beta}} \cdot \frac{\partial f_\alpha}{\partial \boldsymbol{\xi}} \qquad (2.9)$$

This model for the drag will produce a drag term in the momentum equation,

$$\boldsymbol{R}_{\alpha\beta} \equiv \int \boldsymbol{\xi} \left[\frac{\boldsymbol{u}_\beta - \boldsymbol{u}_\alpha}{\tau_{\alpha\beta}} \cdot \frac{\partial f_\alpha}{\partial \boldsymbol{\xi}} \right] d\boldsymbol{\xi} = \frac{\rho_\alpha}{\tau_{\alpha\beta}} \left(\boldsymbol{u}_\beta - \boldsymbol{u}_\alpha \right), \quad (2.10)$$

and a corresponding term in the energy equation,

$$\boldsymbol{u}_\alpha \cdot \boldsymbol{R}_{\alpha\beta} \equiv \int \frac{1}{2} \boldsymbol{\xi}^2 \left[\frac{\boldsymbol{u}_\beta - \boldsymbol{u}_\alpha}{\tau_{\alpha\beta}} \cdot \frac{\partial f_\alpha}{\partial \boldsymbol{\xi}} \right] d\boldsymbol{\xi} = \frac{\rho_\alpha}{\tau_{\alpha\beta}} \left(\boldsymbol{u}_\alpha \cdot \boldsymbol{u}_\beta - \boldsymbol{u}_\alpha^2 \right). \quad (2.11)$$

Note that this model does not account for purely thermal energy transfer or heating from inter-species collisions – i.e. due to $T_\alpha \neq T_\beta$. This can be a reasonable approximation given that the typical time for thermal relaxation between species is slower than each species' thermal self-equilibration time [31].

2.2 Two-Fluid Plasma Model

By taking the moments in equations (2.4)-(2.6) of equation (2.3), the governing fluid equations for each species are obtained,

$$\frac{\partial \rho_\alpha}{\partial t} + \nabla \cdot (\rho_\alpha \boldsymbol{u}_\alpha) = 0 \quad (2.12)$$

$$\frac{\partial (\rho_\alpha \boldsymbol{u}_\alpha)}{\partial t} + \nabla \cdot [\rho_\alpha \boldsymbol{u}_\alpha \boldsymbol{u}_\alpha + \underline{\boldsymbol{P}}_\alpha] = \frac{q_\alpha}{m_\alpha} \left(\rho_\alpha \boldsymbol{u}_\alpha \times \boldsymbol{B} + \rho_\alpha \boldsymbol{E} \right) + \boldsymbol{R}_{\alpha\beta} \quad (2.13)$$

$$\frac{\partial \varepsilon_\alpha}{\partial t} + \nabla \cdot [\boldsymbol{u}\varepsilon_\alpha + \boldsymbol{q}_\alpha + \boldsymbol{u}_\alpha \cdot \underline{\boldsymbol{P}}_\alpha] = \frac{q_\alpha}{m_\alpha} \rho_\alpha \boldsymbol{u}_\alpha \cdot \boldsymbol{E} + \boldsymbol{u}_\alpha \cdot \boldsymbol{R}_{\alpha\beta}. \quad (2.14)$$

In equations (2.12)-(2.14) the subscript $\alpha \in [i, e]$ stands for each species (ions or electrons). The quantity $\underline{\boldsymbol{P}}_\alpha = \underline{1} p_\alpha + \underline{\boldsymbol{\Phi}}$ represents the internal stress tensor of each species, where p is pressure and $\underline{\boldsymbol{\Phi}}$ is viscous (collisional) stress. The term $\boldsymbol{q}_\alpha$ is the species heat flux vector. The quantities $\boldsymbol{R}_{\alpha\beta}$ and $Q_{\alpha\beta}$ represent the momentum transfer (drag) and heat transfer between species α and β due to interspecies collisions.

2.2.1 Maxwell's Equations

For a completely internally self-consistent set of equations, Maxwell's equations for the electromagnetic fields must also be considered.

$$\frac{\partial \boldsymbol{E}}{\partial t} = c^2 \boldsymbol{\nabla} \times \boldsymbol{B} - \frac{\boldsymbol{J}}{\epsilon_0} \tag{2.15}$$

$$\frac{\partial \boldsymbol{B}}{\partial t} = -\boldsymbol{\nabla} \times \boldsymbol{E} \tag{2.16}$$

$$\boldsymbol{\nabla} \cdot \boldsymbol{B} = 0 \tag{2.17}$$

$$\boldsymbol{\nabla} \cdot \boldsymbol{E} = \frac{\rho_Q}{\epsilon_0} \tag{2.18}$$

Equations (2.15) and (2.16) describe the temporal evolution of $\boldsymbol{E}$ and $\boldsymbol{B}$, with $\boldsymbol{J} = \Sigma_\alpha \frac{q_\alpha \rho_\alpha \boldsymbol{u}_\alpha}{m_\alpha}$ denoting the electric current density. Equations (2.17) and (2.18) are constraints which they must obey everywhere in space and time, where $\rho_Q = \Sigma_\alpha \frac{q_\alpha \rho_\alpha}{m_\alpha}$ is the electrical space charge density. These constraints will always be satisfied analytically if they are satisfied on the system boundaries and initially everywhere.

2.3 The Gas-Kinetic Scheme

The focus of this work is on developing an enhanced representation of the Gas-Kinetic Scheme (GKS) or Gas-Kinetic Method (GKM) to form an algorithm for solving the fluid conservation equations for mass, momentum, and energy for the two-fluid plasma equations. Initially developed by Xu and Prendergast [32, 33] in the early 1990s, GKS has been shown to be a highly capable algorithm for solving a wide range of computational fluid dynamics problems.

2.3.1 General GKS Formulation

The foundation of GKS is based on obtaining the time-dependent gas distribution function f from which the fluid fluxes of mass, momentum, and energy may be calculated. Recall equation (2.3), from which we may obtain the fluid conservation equations for the mass, mo-

mentum, and energy of each species.

$$\frac{\partial \rho_\alpha}{\partial t} + \nabla \cdot [\boldsymbol{F}_\alpha^\rho] = 0 \tag{2.19}$$

$$\frac{\partial (\rho_\alpha \boldsymbol{u}_\alpha)}{\partial t} + \nabla \cdot [\underline{\boldsymbol{F}}_\alpha^{\rho \boldsymbol{u}}] = \frac{q_\alpha}{m_\alpha} \left(\rho_\alpha \boldsymbol{u}_\alpha \times \boldsymbol{B} + \rho_\alpha \boldsymbol{E} \right) + \boldsymbol{R}_{\alpha\beta} \tag{2.20}$$

$$\frac{\partial \varepsilon_\alpha}{\partial t} + \nabla \cdot [\boldsymbol{F}_\alpha^\varepsilon] = \frac{q_\alpha}{m_\alpha} \rho_\alpha \boldsymbol{u}_\alpha \cdot \boldsymbol{E} + \boldsymbol{u}_\alpha \cdot \boldsymbol{R}_{\alpha\beta} + Q_{\alpha\beta}. \tag{2.21}$$

However, unlike equations (2.12)-(2.14), the fluxes in equations (2.19)-(2.21) are defined

$$\boldsymbol{F}^\rho = \int_{-\infty}^\infty \boldsymbol{\xi} \left(m \right) f d\boldsymbol{\xi}, \tag{2.22}$$

$$\underline{\boldsymbol{F}}^{\rho \boldsymbol{u}} = \int_{-\infty}^\infty \boldsymbol{\xi} \left(m \boldsymbol{\xi} \right) f d\boldsymbol{\xi}, \tag{2.23}$$

$$\boldsymbol{F}^\varepsilon = \int_{-\infty}^\infty \boldsymbol{\xi} \left(m \frac{1}{2} \boldsymbol{\xi}^2 \right) f d\boldsymbol{\xi}. \tag{2.24}$$

The crux of the GKS algorithm is to solve equation (2.3) to obtain the time-dependent distribution f, in order to calculate fluxes (Equations (2.22)-(2.24)), from which equations (2.19)-(2.21) may be evolved, instead of computing from the purely continuum constitutive relationships of section 2.2. This provides a more consistent physical description of the temporal evolution of the flow. While the overall GKS algorithm is second-order accurate in time, it is different from a second order accurate solution of the equations in section 2.2 – using a two-step Runge-Kutta approach, for example. The difference is that the second-order temporal evolution of GKS is more *physically consistent*. This is due to the fact that GKS determines the mass, momentum, and energy fluxes from a single distribution. Thus it circumvents potential inconsistencies which could arise in other solvers using constitutive relationships [10].

3. MODEL FORMULATION AND DEVELOPMENT

The central theme of GKS is to calculate the various fluxes in the governing equations of the conserved quantities – ρ, $\rho\boldsymbol{u}$, and ε – using a kinetic distribution function rather than constitutive relations. In this Chapter our goal is to develop the theoretical framework for applying the gas-kinetic approach to a two-fluid plasma. Our approach in this section is as follows:

1. Discussion of the Boltzmann equation as the underlying fundamental governing equation for the fluid behavior.

2. Non-dimensionalization of the Boltzmann-BGK equation and subsequent order-of-magnitude analysis of individual terms.

3. Application of the Chapman-Enskog expansion to the non-dimensionalized B-BGK equation to determine non-equilibrium behavior of the distribution f.

4. Development of Method-of-Characteristics (MoC) solution to obtain time-dependent distribution $f(t)$.

5. Calculation of moments of $f(t)$ and derivation of closure equations to obtain final analytic flux expression.

3.1 The Boltzmann-BGK (B-BGK) Equation

In this study we restrict ourselves to the B-BGK equation – equation (2.7)– along with the Stokes'-Drag model – equation (2.9) – for interspecies collisions.

$$\frac{\partial f_\alpha}{\partial t} + \boldsymbol{\xi} \cdot \frac{\partial f_\alpha}{\partial \boldsymbol{x}} + \frac{q_\alpha}{m_\alpha}\left(\boldsymbol{E} + \boldsymbol{\xi} \times \boldsymbol{B}\right) \cdot \frac{\partial f_\alpha}{\partial \boldsymbol{\xi}} = \frac{g_\alpha - f_\alpha}{\tau_{\alpha\alpha}} - \frac{\boldsymbol{U}_{\alpha\beta}}{\tau_{\alpha\beta}} \cdot \frac{\partial f_\alpha}{\partial \boldsymbol{\xi}}. \tag{3.1}$$

In equation (3.1) f_α is the single particle distribution function for species α, while g_α is the equilibrium distribution towards which f_α relaxes due to collisions. $\boldsymbol{U}_{\alpha\beta} = \boldsymbol{u}_\beta - \boldsymbol{u}_\alpha$ is

the mean velocity differential between species α and β. The collision time $\tau_{\alpha\beta}$ is that for particles from species α with species β – note that this only applies for $\beta \neq \alpha$. The peculiar velocity $\boldsymbol{c}$ is defined as the difference between the particle velocity $\boldsymbol{\xi}$ and the mean species velocity $\boldsymbol{u}$: $\boldsymbol{c} \equiv \boldsymbol{\xi} - \boldsymbol{u}$. The definition of $\boldsymbol{c}$ we may split $\boldsymbol{\xi}$ into $\boldsymbol{\xi} = \boldsymbol{u} + \boldsymbol{c}$. In equation (3.1) we may split $\boldsymbol{\xi} \times \boldsymbol{B} = \boldsymbol{u} \times \boldsymbol{B} + \boldsymbol{c} \times \boldsymbol{B}$, and denote $\boldsymbol{E}' = \boldsymbol{E} + \boldsymbol{u} \times \boldsymbol{B}$ as the electric field in the frame moving with velocity $\boldsymbol{u}$. The effect of splitting the magnetic field acceleration term is essentially to divide it into "fluid" and "kinetic" portions [34]. From here on we will suppress the α subscript in equation (3.1) for clarity.

$$\frac{\partial f}{\partial t} + \boldsymbol{\xi} \cdot \frac{\partial f}{\partial \boldsymbol{x}} + \frac{q}{m}\left(\boldsymbol{E}' + \boldsymbol{c} \times \boldsymbol{B}\right) \cdot \frac{\partial f}{\partial \boldsymbol{\xi}} = \frac{g - f}{\tau} - \frac{\boldsymbol{U}_\beta}{\tau_\beta} \cdot \frac{\partial f}{\partial \boldsymbol{\xi}} \tag{3.2}$$

3.1.1 Non-dimensionalization of B-BGK Equation

To non-dimensionalize equation (3.2) we choose a scaling length l_0 and time t_0 and define the characteristic velocity to be the thermal velocity v_{th} where $v_{th} = \sqrt{\frac{kT}{m}}$, where k is the Boltzmann constant, and T is fluid temperature. In equation (3.2) we may then replace the temporal and spatial partial derivatives:

$$\frac{\partial}{\partial t} = \frac{1}{t_0}\frac{\partial}{\partial \hat{t}}, \tag{3.3}$$

$$\frac{\partial}{\partial \boldsymbol{x}} = \frac{1}{l_0}\frac{\partial}{\partial \hat{\boldsymbol{x}}}. \tag{3.4}$$

The particle velocity may be normalized such that $\boldsymbol{\xi} = v_{th}\hat{\boldsymbol{\xi}}$, which assumes that the mean fluid velocity is $O(v_{th})$. Thus we have

$$\frac{\partial}{\partial \boldsymbol{\xi}} = \frac{1}{v_{th}}\frac{\partial}{\partial \hat{\boldsymbol{\xi}}}. \tag{3.5}$$

The resulting normalization of equation (3.2) is

$$\frac{\partial f}{\partial \hat{t}} + \frac{t_0 v_{th}}{l_0}\hat{\boldsymbol{\xi}} \cdot \frac{\partial f}{\partial \hat{\boldsymbol{x}}} + \frac{t_0 q}{m v_{th}}E_0'\hat{\boldsymbol{E}}' \cdot \frac{\partial f}{\partial \hat{\boldsymbol{\xi}}} + \frac{t_0 q B_0}{m}\left(\hat{\boldsymbol{c}} \times \hat{\boldsymbol{B}}\right) \cdot \frac{\partial f}{\partial \hat{\boldsymbol{\xi}}} =$$
$$\frac{t_0}{\tau}(g - f) - \frac{t_0 U_\beta}{\tau_\beta v_{th}}\hat{\boldsymbol{U}}_\beta \cdot \frac{\partial f}{\partial \hat{\boldsymbol{\xi}}}. \quad (3.6)$$

Where $E_0 \equiv |\boldsymbol{E}'|$, $B_0 \equiv |\boldsymbol{B}|$, and $U_\beta \equiv |\boldsymbol{U}_\beta|$. In addition we have multiplied equation (3.6) by t_0 so that the entire equation is in units of f. We also will take $t_0 = l_0/(v_{th})$. Finally, we will choose scaling for the electric and magnetic fields and inter-species collisions. The quantity $\frac{q B_0}{m} = \omega_c$ is simply the cyclotron frequency. However, it is slightly less straightforward for the electric field and the inter-species collisions (drag). We take the scaling

$$U_\beta \approx \frac{v_{th}}{(1 + \omega_c t_0)}, \quad (3.7)$$

as we are only considering charged species. Physically, this means that U_β is of the order of the characteristic speed as $\omega_c t_0 \ll 1$, but decreases as $\omega_c t_0 \gg 1$ because of increased correlation between the ion and electron motion due to the action of the electromagnetic fields. We will also take the scaling $qE_0' \approx \frac{m v_{th}^2}{l_0}$, meaning the electric field force on a particle will typically change the kinetic energy of a particle by $m v_{th}^2$ over a distance l_0.

$$\frac{\partial f}{\partial \hat{t}} + \hat{\boldsymbol{\xi}} \cdot \frac{\partial f}{\partial \hat{\boldsymbol{x}}} + \hat{\boldsymbol{E}}' \cdot \frac{\partial f}{\partial \hat{\boldsymbol{\xi}}} + t_0 \omega_c\left(\hat{\boldsymbol{c}} \times \hat{\boldsymbol{B}}\right) \cdot \frac{\partial f}{\partial \hat{\boldsymbol{\xi}}} = \frac{t_0}{\tau}(g - f) - \frac{t_0}{\tau_\beta(1 + t_0\omega_c)}\hat{\boldsymbol{U}}_\beta \cdot \frac{\partial f}{\partial \hat{\boldsymbol{\xi}}} \quad (3.8)$$

Equation (3.8) follows a similar non-dimensionalization scheme to that of Araya et al. [1] and Section 4.11 of Fitzpatrick [36], where all hatted quantities ($\hat{\cdot}$) are $O(1)$.

$$\frac{\partial f}{\partial \hat{t}} + \hat{\boldsymbol{\xi}} \cdot \frac{\partial f}{\partial \hat{\boldsymbol{x}}} + \hat{\boldsymbol{E}}' \cdot \frac{\partial f}{\partial \hat{\boldsymbol{\xi}}} + t_0 \omega_c\left(\hat{\boldsymbol{c}} \times \hat{\boldsymbol{B}}\right) \cdot \frac{\partial f}{\partial \hat{\boldsymbol{\xi}}} = \frac{t_0}{\tau}(g - f) - \frac{t_0}{\tau_\beta(1 + t_0\omega_c)}\hat{\boldsymbol{U}}_\beta \cdot \frac{\partial f}{\partial \hat{\boldsymbol{\xi}}} \quad (3.9)$$

18

3.1.2 Chapman-Enskog Expansion

Starting with equation (3.9) we can start to determine which may be the important components. We can replace $t_0 \omega_c$ by defining the Larmor radius

$$r_L \equiv \frac{v_{th}}{\omega_c}, \tag{3.10}$$

so that

$$t_0 \omega_c = \frac{l_0}{r_L} = \hat{r}_L^{-1}. \tag{3.11}$$

Thus equation (3.8) may be re-written:

$$\frac{\partial f}{\partial \hat{t}} + \hat{\boldsymbol{\xi}} \cdot \frac{\partial f}{\partial \hat{\boldsymbol{x}}} + \hat{\boldsymbol{E}}' \cdot \frac{\partial f}{\partial \hat{\boldsymbol{\xi}}} + \frac{1}{\hat{r}_L} \left(\hat{\boldsymbol{c}} \times \hat{\boldsymbol{B}} \right) \cdot \frac{\partial f}{\partial \hat{\boldsymbol{\xi}}} = \frac{t_0}{\tau}(g - f) - \frac{t_0 \hat{r}_L}{\tau_\beta (1 + \hat{r}_L)} \hat{\boldsymbol{U}}_\beta \cdot \frac{\partial f}{\partial \hat{\boldsymbol{\xi}}} \tag{3.12}$$

Equation (3.12) is similar to the scaling presented by Araya et al., with the addition of the term for inter-species collisions [35]. However, we will take a slightly different perspective. We are interested in the two-fluid equations, which implicitly requires that $\frac{\tau}{t_0} = \epsilon \ll 1$ be true. The parameter ϵ is effectively the Knudsen number, which may also be defined $\epsilon = \frac{\lambda_{\text{mfp}}}{l_0}$ where λ_{mfp} is the mean free path for species α. Specifically, we will assume that a Chapman-Enskog type approach may be employed, wherein we will approximate f as being near thermal equilibrium, and expand it near a Maxwellian distribution, g.

$$f = g + f^{(1)} + f^{(2)} + \cdots \rightarrow \frac{f}{g} = \phi = 1 + \phi^{(1)} + \phi^{(2)} + \dots \tag{3.13}$$

Where $\phi^{(1)} = O(\epsilon)$, $\phi^{(2)} = O(\epsilon^2)$, etc., where $\epsilon \equiv |\tau \mathbb{D} \ln f| \approx \frac{\tau}{t_0} \ll 1$. The operator $\mathbb{D}$ indicates the sum of operators acting on f in equation (3.1). Clearly, $\mathbb{D} = O(t_0^{-1})$, where t_0 is some "large-scale" time for variation of the distribution. That is, it t_0 is essentially the "macroscopic time-scale" of temporal variations in the fluid, while l_0 is the "macroscopic length-scale" for spatial variations. If we truncate equation (3.13) to second order – only

19

retaining terms of $O(\epsilon)$ – we will capture the equations to Navier-Stokes order in terms of the Knudsen number.

Next we insert the expansion of equation (3.13) into equation (3.12)

$$
\frac{\partial(g + f^{(1)})}{\partial \hat{t}} + \hat{\boldsymbol{\xi}} \cdot \frac{\partial(g + f^{(1)})}{\partial \hat{\boldsymbol{x}}} + \hat{\boldsymbol{E}}' \cdot \frac{\partial(g + f^{(1)})}{\partial \hat{\boldsymbol{\xi}}}
$$
$$
+ \frac{1}{\hat{r}_L}\left(\hat{\boldsymbol{c}} \times \hat{\boldsymbol{B}}\right) \cdot \frac{\partial(g + f^{(1)})}{\partial \hat{\boldsymbol{\xi}}} = \frac{t_0}{\tau}(-f^{(1)}) - \frac{t_0 \hat{r}_L}{\tau_\beta(1 + \hat{r}_L)}\hat{\boldsymbol{U}}_\beta \cdot \frac{\partial(g + f^{(1)})}{\partial \hat{\boldsymbol{\xi}}}, \quad (3.14)
$$

and recall the form of the Maxwellian g, for the equilibrium solution of f:

$$
g = \rho \left(\frac{m}{2\pi kT}\right)^{\frac{3}{2}} \exp\left(-\frac{m}{2kT}(\boldsymbol{\xi} - \boldsymbol{u})^2\right) = \rho \left(\frac{m}{2\pi kT}\right)^{\frac{3}{2}} \exp\left(-\frac{m}{2kT}\boldsymbol{c}^2\right). \quad (3.15)
$$

Thus, $\frac{\partial g}{\partial \boldsymbol{\xi}} \propto \boldsymbol{c}$, and therefore $(\hat{\boldsymbol{c}} \times \hat{\boldsymbol{B}}) \cdot \frac{\partial g}{\partial \hat{\boldsymbol{\xi}}}$ is equivalently zero:

$$
\frac{\partial(g + f^{(1)})}{\partial \hat{t}} + \hat{\boldsymbol{\xi}} \cdot \frac{\partial(g + f^{(1)})}{\partial \hat{\boldsymbol{x}}} + \hat{\boldsymbol{E}}' \cdot \frac{\partial(g + f^{(1)})}{\partial \hat{\boldsymbol{\xi}}}
$$
$$
+ \frac{1}{\hat{r}_L}\left(\hat{\boldsymbol{c}} \times \hat{\boldsymbol{B}}\right) \cdot \frac{\partial(f^{(1)})}{\partial \hat{\boldsymbol{\xi}}} = \frac{t_0}{\tau}(-f^{(1)}) - \frac{t_0 \hat{r}_L}{\tau_\beta(1 + \hat{r}_L)}\hat{\boldsymbol{U}}_\beta \cdot \frac{\partial(g + f^{(1)})}{\partial \hat{\boldsymbol{\xi}}}. \quad (3.16)
$$

We can then normalize equation (3.16) by g and order the terms individually by order of magnitude, we will obtain equations (3.17) – (3.22).

$$
\frac{\partial(\ln g)}{\partial \hat{t}} \sim O(1) \tag{3.17}
$$

$$
\hat{\boldsymbol{\xi}} \cdot \frac{\partial(\ln g)}{\partial \hat{\boldsymbol{x}}} \sim O(1) \tag{3.18}
$$

$$
\hat{\boldsymbol{E}}' \cdot \frac{\partial(\ln g)}{\partial \hat{\boldsymbol{\xi}}} \sim O(1) \tag{3.19}
$$

$$
\frac{\left(\hat{\boldsymbol{c}} \times \hat{\boldsymbol{B}}\right)}{\hat{r}_L} \cdot \frac{\partial(\phi^{(1)})}{\partial \hat{\boldsymbol{\xi}}} \sim O\left(\frac{\epsilon}{\hat{r}_L}\right) \tag{3.20}
$$

$$
\frac{t_0}{\tau}(-\phi^{(1)}) \sim O(1) \tag{3.21}
$$

$$
\frac{t_0 \hat{r}_L \hat{\boldsymbol{U}}_\beta}{\tau_\beta(1 + \hat{r}_L)} \cdot \frac{\partial(\ln g)}{\partial \hat{\boldsymbol{\xi}}} \sim O\left(\frac{t_0 \hat{r}_L}{\tau_\beta(1 + \hat{r}_L)}\right) \tag{3.22}
$$

20

Terms (3.17) – (3.19) and (3.21) are all clearly $O(1)$ and will most likely be retained. For term (3.20), we see that this may be rearranged by realizing that $\hat{r}_L^{-1} = t_0\omega_c$ and $\frac{\tau}{t_0} = \epsilon$. Defining the Hall parameter $\varpi \equiv \tau\omega_c$, we observe that $\hat{r}_L^{-1} = \frac{\tau\omega_c}{\tau/t_0} = \frac{\varpi}{\epsilon}$. Thus, this term is $O(\varpi)$ overall. This is smaller for the ions than the electrons, but for most problems we are interested in we expect $O(\varpi) > O(\epsilon)$, so it will be retained.

For term (3.22) we first look at the portion $O(\frac{t_0}{\tau_\beta})$. For the ions, we may typically assume that this may be $\sim O(1)$, but for the electrons it will typically be $\sim O(\epsilon^{-1})$ (due to the disparate mass ratio between species). For $\frac{\hat{r}_L}{(1+\hat{r}_L)}$, we see that for $\hat{r}_L \gtrsim 1$ this scales as $\sim O(1)$, but for $\hat{r}_L \ll 1$ it scales as $\sim O(\hat{r}_L)$. For the electrons, we may typically expect $\hat{r}_L \ll 1$ for the flows we are interested in. Thus, we expect this term to scale as $O(\frac{\hat{r}_L}{\epsilon})$ for the electrons, which is likely $\sim O(1)$ if $\hat{r}_L \sim O(\epsilon)$. For the ions, we typically expect that $\hat{r}_L \lesssim O(1)$, thus this term may scale as $\sim O(\hat{r}_L) \lesssim O(1)$ which is not necessarily negligible. Thus, we conclude that while some terms may be slightly larger or smaller than $O(1)$, for the cases we are interested in they may all be considered to be of approximately the same order. As a consequence we must include all of the terms (3.17) – (3.22) for our analysis to be complete. The additional terms in equation (3.16) – e.g., $\frac{\partial f^{(1)}}{\partial t}$ – contain an additional factor of ϵ and may all therefore be neglected.

3.1.3 Solving for the Non-equilibrium Distribution

To obtain a closed expression for $f^{(1)}$, we retain the leading order terms of the previous analysis.

$$\frac{\partial g}{\partial t} + \boldsymbol{\xi} \cdot \frac{\partial g}{\partial \boldsymbol{x}} + \frac{q}{m}\boldsymbol{E}' \cdot \frac{\partial g}{\partial \boldsymbol{\xi}} + \frac{q}{m}\boldsymbol{c} \times \boldsymbol{B} \cdot \frac{\partial f^{(1)}}{\partial \boldsymbol{\xi}} = -\frac{f^{(1)}}{\tau} - \frac{\boldsymbol{U}_\beta}{\tau_\beta} \cdot \frac{\partial g}{\partial \boldsymbol{\xi}}, \qquad (3.23)$$

Combing the leading order terms, we obtain equation (3.23) which must be solved to obtain $f^{(1)}$. If we denote $\phi^{(1)} \equiv f^{(1)}/g$, and rearrange equation (3.23), we will get:

$$\phi^{(1)} + \tau\frac{q}{m}\boldsymbol{c} \times \boldsymbol{B} \cdot \frac{\partial \phi^{(1)}}{\partial \boldsymbol{\xi}} = -\tau\left[\frac{\partial \ln g}{\partial t} + \boldsymbol{\xi} \cdot \frac{\partial \ln g}{\partial \boldsymbol{x}} + \frac{q}{m}\boldsymbol{E}' \cdot \frac{\partial \ln g}{\partial \boldsymbol{\xi}} + \frac{\boldsymbol{U}_\beta}{\tau_\beta} \cdot \frac{\partial \ln g}{\partial \boldsymbol{\xi}}\right] \quad (3.24)$$

If we replace $\boldsymbol{B} = |\boldsymbol{B}|\hat{\boldsymbol{b}}$, and re-introducing the Hall parameter as $\varpi = \tau\omega_c$, equation (3.24) becomes

$$\phi^{(1)} + \varpi\boldsymbol{c} \times \hat{\boldsymbol{b}} \cdot \frac{\partial\phi^{(1)}}{\partial\boldsymbol{\xi}} = -\tau\left[\frac{\partial\ln g}{\partial t} + \boldsymbol{\xi} \cdot \frac{\partial\ln g}{\partial\boldsymbol{x}} + \frac{q}{m}\boldsymbol{E}' \cdot \frac{\partial\ln g}{\partial\boldsymbol{\xi}} + \frac{\boldsymbol{U}_\beta}{\tau_\beta} \cdot \frac{\partial\ln g}{\partial\boldsymbol{\xi}}\right] \quad (3.25)$$

Thus, equation (3.25) will asymptotically reduce to the usual expression for $f^{(1)}$ in a Navier-Stokes fluid in the limit of $\varpi \to 0$,

$$\phi^{(1)} = -\tau\left[\frac{\partial\ln g}{\partial t} + \boldsymbol{\xi} \cdot \frac{\partial\ln g}{\partial\boldsymbol{x}} + \frac{q}{m}\boldsymbol{E}' \cdot \frac{\partial\ln g}{\partial\boldsymbol{\xi}} + \frac{\boldsymbol{U}_\beta}{\tau_\beta} \cdot \frac{\partial\ln g}{\partial\boldsymbol{\xi}}\right]. \quad (3.26)$$

The chain rule may be directly applied to g to obtain the derivatives of g with respect to t, $\boldsymbol{x}$, and $\boldsymbol{\xi}$ in terms of the primitive variables,

$$\frac{\partial g}{\partial t} = \frac{\partial g}{\partial\rho}\frac{\partial\rho}{\partial t} + \frac{\partial g}{\partial\boldsymbol{u}} \cdot \frac{\partial\boldsymbol{u}}{\partial t} + \frac{\partial g}{\partial T}\frac{\partial T}{\partial t}, \quad (3.27)$$

$$\frac{\partial g}{\partial\boldsymbol{x}} = \frac{\partial g}{\partial\rho}\frac{\partial\rho}{\partial\boldsymbol{x}} + \frac{\partial g}{\partial\boldsymbol{u}} \cdot \frac{\partial\boldsymbol{u}}{\partial\boldsymbol{x}} + \frac{\partial g}{\partial T}\frac{\partial T}{\partial\boldsymbol{x}}, \quad (3.28)$$

$$\frac{\partial g}{\partial\boldsymbol{\xi}} = -\frac{m}{kT}(\boldsymbol{\xi} - \boldsymbol{u})\,g. \quad (3.29)$$

If we introduce the ideal (i.e. Euler) equations for the primitive variables ρ, $\boldsymbol{u}$, and T,

$$\frac{\partial\rho}{\partial t} = -\rho\nabla \cdot \boldsymbol{u} - \boldsymbol{u} \cdot \nabla\rho, \quad (3.30)$$

$$\frac{\partial\boldsymbol{u}}{\partial t} = -\boldsymbol{u} \cdot \nabla\left[\boldsymbol{u}\right] - \frac{k}{m}\nabla T - \frac{kT}{\rho m}\nabla\rho + \frac{q}{m}\left(\boldsymbol{u} \times \boldsymbol{B} + \boldsymbol{E}\right) + \frac{1}{\rho}\boldsymbol{R}_\beta, \quad (3.31)$$

$$\frac{\partial T}{\partial t} = -\boldsymbol{u} \cdot \nabla\left[T\right] - \frac{2}{3}T\nabla \cdot \left[\boldsymbol{u}\right], \quad (3.32)$$

equation (3.26) becomes

$$\phi^{(1)} = -\tau\left[\left(\frac{m}{2kT}c^2 - \frac{5}{2}\right)\frac{\boldsymbol{c}}{T} \cdot \frac{\partial T}{\partial\boldsymbol{x}} + \frac{m}{kT}\left(\boldsymbol{cc} - \frac{c^2}{3}\boldsymbol{1}\right) : \frac{\partial\boldsymbol{u}}{\partial\boldsymbol{x}}\right]. \quad (3.33)$$

22

The notation : is a "double dot product" to indicate for example $\boldsymbol{a} \cdot \underline{\boldsymbol{A}} \cdot b = \boldsymbol{ab} : \underline{bmA}$, where $\boldsymbol{a}$ and $\boldsymbol{b}$ are arbitrary vectors and $\underline{bmA}$ is an arbitrary second-order tensor. Equivalently, we could write $a_i A_{ij} b_j$ in index notation. Note that the drag term $\boldsymbol{R}_\beta$ in equation (3.31) is defined $\boldsymbol{R}_\beta \equiv \rho \frac{\boldsymbol{U}_\beta}{\tau_\beta}$. Equation (3.33) will produce the familiar Fourier's Law for heat conduction (i.e. $\boldsymbol{q} = -\kappa \boldsymbol{\nabla} T$, where $\kappa \equiv \frac{5}{2} \frac{k}{m} \tau p$) and Navier-Stokes stress tensor (see e.g., appendix A of [13]). The right-hand side of equations (3.25) and (3.26) are equivalent to the right-hand side of equation (3.33), thus from equation (3.25) we obtain the equation which gives the first order correction $f^{(1)}$ for the magnetized case,

$$\phi^{(1)} + \varpi \boldsymbol{c} \times \hat{\boldsymbol{b}} \cdot \frac{\partial \phi^{(1)}}{\partial \boldsymbol{\xi}} = -\tau \left[\left(\frac{m}{2kT} \boldsymbol{c}^2 - \frac{5}{2} \right) \frac{\boldsymbol{c}}{T} \cdot \frac{\partial T}{\partial \boldsymbol{x}} + \frac{m}{kT} \left(\boldsymbol{cc} - \frac{\boldsymbol{c}^2}{3} \underline{1} \right) : \frac{\partial \boldsymbol{u}}{\partial \boldsymbol{x}} \right]. \quad (3.34)$$

Equation (3.34) was solved by Woods [34] for $f^{(1)}$ by observing that since $\boldsymbol{\nabla} T$ and $\boldsymbol{\nabla} \boldsymbol{u}$ are independent, the terms pertaining to each of them may be obtained separately and afterwards be joined.

$$\phi^{(1)}_{\boldsymbol{\nabla} T} + \varpi \boldsymbol{c} \times \hat{\boldsymbol{b}} \cdot \frac{\partial \phi^{(1)}_{\boldsymbol{\nabla} T}}{\partial \boldsymbol{\xi}} = -\tau \left[\left(\frac{m}{2kT} \boldsymbol{c}^2 - \frac{5}{2} \right) \frac{\boldsymbol{c}}{T} \cdot \frac{\partial T}{\partial \boldsymbol{x}} \right] \quad (3.35)$$

$$\phi^{(1)}_{\boldsymbol{\nabla} \boldsymbol{u}} + \varpi \boldsymbol{c} \times \hat{\boldsymbol{b}} \cdot \frac{\partial \phi^{(1)}_{\boldsymbol{\nabla} \boldsymbol{u}}}{\partial \boldsymbol{\xi}} = -\tau \left[\frac{m}{kT} \left(\boldsymbol{cc} - \frac{\boldsymbol{c}^2}{3} \underline{1} \right) : \frac{\partial \boldsymbol{u}}{\partial \boldsymbol{x}} \right] \quad (3.36)$$

To solve equations (3.35) – (3.36), we can will assume a solution and demonstrate that it satisfies the governing equation. First we make two important observations:

1. In the limit of $\varpi \to 0$, the second term on the LHS of equations (3.35) and (3.36) disappears, i.e. $\phi^{(1)}$ asymptotically approaches the expression on the RHS.

2. In the limit of $\varpi \to \infty$, the first order correction $\phi^{(1)}$ should be bounded. This may be understood physically from the kinetic perspective. The magnetic field will not affect motion parallel to itself and will not directly do work on the charged species to increase or decrease their energy. Its action will be to redirect existing transport and impeded motion which is perpendicular to itself. Thus at large values of ϖ, we expect

23

to see "anisotropization" of the transport.

Thus, we propose a solution for equation (3.35) of the form

$$\phi_{\boldsymbol{\nabla} T}^{(1)} = \left(\frac{m}{2kT} \boldsymbol{c}^2 - \frac{5}{2} \right) \boldsymbol{c} \cdot \boldsymbol{A}_T, \tag{3.37}$$

where $\boldsymbol{A}_T \equiv \boldsymbol{A}_T(|\boldsymbol{c}|^2, \boldsymbol{c} \cdot \hat{\boldsymbol{b}}, \boldsymbol{x}, t)$, but is not a function of $\boldsymbol{c}$ itself. Substituting equation (3.37) into equation (3.35), we find that $\boldsymbol{A}_T$ must satisfy the following:

$$\left(\frac{m}{2kT} \boldsymbol{c}^2 - \frac{5}{2} \right) \left[\boldsymbol{c} \cdot \boldsymbol{A}_T + \varpi (\boldsymbol{c} \times \hat{\boldsymbol{b}}) \cdot \boldsymbol{A}_T + \frac{\tau}{T} \boldsymbol{c} \cdot \frac{\partial T}{\partial \boldsymbol{x}} \right] = 0, \tag{3.38}$$

from which it is straightforward to determine that $\boldsymbol{A}_T$ must be given by $\boldsymbol{A}_T = -\frac{\tau}{T} \underline{\hat{\boldsymbol{\kappa}}} \cdot \frac{\partial T}{\partial \boldsymbol{x}}$. If we turn to index notation for perspicuity, the tensor $\hat{\kappa}_{ij}$ is defined by the normalized magnetic field vector $\hat{\boldsymbol{b}}$, denoted b_i in index notation,

$$\hat{\kappa}_{ij} = b_i b_j + \frac{1}{1 + \varpi^2} \left(\delta_{ij} - b_i b_j \right) - \frac{\varpi}{1 + \varpi^2} \epsilon_{ikj} b_k. \tag{3.39}$$

For $\phi_{\boldsymbol{\nabla} \boldsymbol{u}}^{(1)}$, similar to equation (3.37) we will use the last term on the right-hand side of equation (4.12) or (4.13) as a starting point and assume a solution of the same form for equation (3.36):

$$\phi_{\boldsymbol{\nabla} \boldsymbol{u}}^{(1)} = \left(\boldsymbol{cc} - \frac{\boldsymbol{c}^2}{3} \underline{1} \right) : \underline{\boldsymbol{A}}_{\boldsymbol{u}}, \tag{3.40}$$

where once again $\boldsymbol{A}_{\boldsymbol{u}} \equiv \boldsymbol{A}_{\boldsymbol{u}}(|\boldsymbol{c}|^2, \boldsymbol{c} \cdot \hat{\boldsymbol{b}}, \boldsymbol{x}, t)$, but is not a function of $\boldsymbol{c}$ itself. Substituting equation (3.40) into equation (3.36), we find that $\boldsymbol{A}_{\boldsymbol{u}}$ must satisfy the following:

$$\left[\left(\boldsymbol{cc} - \frac{\boldsymbol{c}^2}{3} \underline{1} \right) : \left(\underline{\boldsymbol{A}}_{\boldsymbol{u}} + \frac{\tau m}{kT} \frac{\partial \boldsymbol{u}}{\partial \boldsymbol{x}} \right) + \left(\varpi (\boldsymbol{c} \times \hat{\boldsymbol{b}}) \boldsymbol{c} + \boldsymbol{c} \varpi (\boldsymbol{c} \times \hat{\boldsymbol{b}}) \right) : \underline{\boldsymbol{A}}_{\boldsymbol{u}} \right] = 0, \tag{3.41}$$

from which, $\underline{\boldsymbol{A}}_{\boldsymbol{u}}$ may be determined to be $\underline{\boldsymbol{A}}_{\boldsymbol{u}} = -\tau \frac{m}{kT} \left(\boldsymbol{cc} - \frac{\boldsymbol{c}^2}{3} \underline{1} \right) : \underline{\hat{\underline{M}}} : \frac{\partial \boldsymbol{u}}{\partial \boldsymbol{x}}$. To define

$\underline{\hat{M}}$, again turning to index notation, we find:

$$\hat{M}_{ijkl} = \mathbb{N}^{(1)}_{ijkl} + \frac{1}{1+4\varpi^2}\mathbb{N}^{(2)}_{ijkl} + \frac{1}{1+\varpi^2}\mathbb{N}^{(3)}_{ijkl} + \frac{2\varpi}{1+4\varpi^2}\mathbb{N}^{(4)}_{ijkl} + \frac{\varpi}{1+\varpi^2}\mathbb{N}^{(5)}_{ijkl}. \quad (3.42)$$

where the tensors $\mathbb{N}^{(j)}_{ijkl}$ are defined by equations (3.43) – (3.47).

$$\mathbb{N}^{(1)}_{ijkl} \equiv \frac{1}{2}\Big[\delta_{ik}\delta jl + 3b_ib_jb_kb_l - (b_ib_k\delta_{jl} + b_jb_k\delta_{il}) + \epsilon_{imk}b_m\epsilon_{jnl}b_n\Big] \quad (3.43)$$

$$\mathbb{N}^{(2)}_{ijkl} \equiv \frac{1}{2}\Big[\delta_{ik}\delta jl + b_ib_jb_kb_l - (b_ib_k\delta_{jl} + b_jb_k\delta_{il}) - \epsilon_{imk}b_m\epsilon_{jnl}b_n\Big] \quad (3.44)$$

$$\mathbb{N}^{(3)}_{ijkl} \equiv -2b_ib_jb_kb_l + (b_ib_k\delta_{jl} + b_jb_k\delta_{il}) \quad (3.45)$$

$$\mathbb{N}^{(4)}_{ijkl} \equiv \frac{1}{2}\Big[\epsilon_{iml}b_mb_kb_j + \epsilon_{jml}b_mb_kb_i - \epsilon_{imk}b_m\delta_{jl} - \epsilon_{jmk}b_m\delta_{il}\Big] \quad (3.46)$$

$$\mathbb{N}^{(5)}_{ijkl} \equiv -\epsilon_{iml}b_mb_kb_j - \epsilon_{jml}b_mb_kb_i \quad (3.47)$$

$$\phi^{(1)} = -\tau\left[\left(\frac{m}{2kT}c^2 - \frac{5}{2}\right)\frac{c}{T}\cdot\hat{\underline{\kappa}}\cdot\frac{\partial T}{\partial x} + \frac{m}{kT}\left(cc - \frac{c^2}{3}\mathbf{1}\right):\underline{\hat{M}}:\frac{\partial u}{\partial x}\right] \quad (3.48)$$

By combining the previous results, we can conclude that the solution of equation (3.25) is given by equation (3.48). A more in-depth presentation of the derivation of the particular terms in $\underline{A}_u$ may be found in Chapter 12 of [34].

3.1.4 Example: Magnetized Heat Flux

From the constitutive model of equation (3.48), the modified Fourier's Law of heat conduction becomes $q = -\underline{\kappa}\cdot\boldsymbol{\nabla}T$, where $\underline{\kappa} \equiv \frac{5}{2}\frac{k}{m}\tau p\hat{\underline{\kappa}}$. Figure 3.1 depicts a schematic example of the magnetized Fourier's Law. In this figure we have chosen a frame where the anti-gradient of the temperature lies in the X-Y plane, and the magnetic field vector lies along the Z-axis. We can see that as the Hall parameter is increased, the component of the Fourier heat flux perpendicular to B is reduced, and a transverse component is introduced. As the Hall parameter increases to very large values, the heat flux becomes nearly parallel to the magnetic field vector. A more detailed analysis of the behavior of the TFPGKS fluxes is done in Section 6.1.

$\overline{q}(\varpi)$ vs. $-\overline{\nabla}T$ and $\overline{b}$
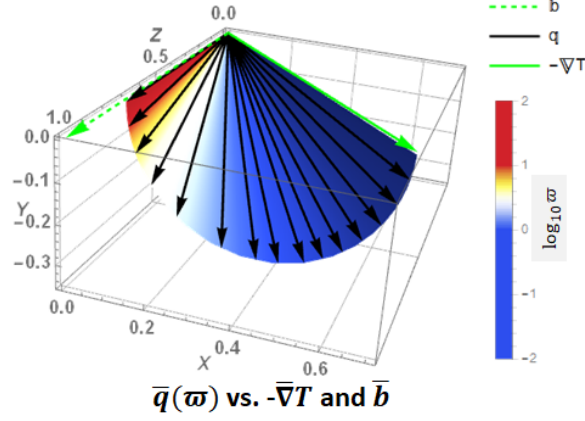
Figure 3.1: Schematic depiction of the magnetized heat flux versus the regular Fourier heat flux as the magnetization (characterized by the Hall parameter $\varpi \equiv \tau\omega_c$) becomes increasingly pronounced

3.2 B-BGK Method of Characteristics (MoC) Solution

To obtain the Method of Characteristics solution for the BGK flux, we return again to the B-BGK equation:

$$\frac{\partial f}{\partial t} + \boldsymbol{\xi} \cdot \frac{\partial f}{\partial \boldsymbol{x}} + \frac{q}{m}\left(\boldsymbol{E} + \boldsymbol{\xi} \times \boldsymbol{B}\right) \cdot \frac{\partial f}{\partial \boldsymbol{\xi}} = \frac{g - f}{\tau} - \frac{\boldsymbol{U}_\beta}{\tau_\beta} \cdot \frac{\partial f}{\partial \boldsymbol{\xi}}.$$

The terms on the LHS may be regarded collectively as $\frac{df}{dt}$,

$$\frac{df}{dt} = \frac{g - f}{\tau} - \frac{\boldsymbol{U}_\beta}{\tau_\beta} \cdot \frac{\partial f}{\partial \boldsymbol{\xi}}, \tag{3.49}$$

where the characteristics are given by the solution:

$$\frac{d\boldsymbol{x}}{dt} = \boldsymbol{\xi}(t), \tag{3.50}$$

$$\frac{d\boldsymbol{\xi}}{dt} = \frac{q}{m}\left(\boldsymbol{E}(\boldsymbol{x}, t) + \boldsymbol{\xi}(t) \times \boldsymbol{B}(\boldsymbol{x}, t)\right). \tag{3.51}$$

However, this will give us complicated particle trajectories in phase space, as shown in Figure 3.2.

26
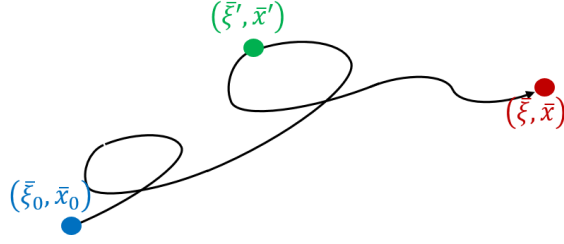
Figure 3.2: Schematic of a hypothetical particle trajectory in phase space based on equation (3.49)

However, this can be circumvented by the following approach, wherein $\frac{df}{dt}$ is considered to be defined in a different way:

$$\frac{df}{dt} = \frac{g - f}{\tau} - \frac{\boldsymbol{U}_\beta}{\tau_\beta} \cdot \frac{\partial f}{\partial \boldsymbol{\xi}} - \frac{q}{m}\left(\boldsymbol{E} + \boldsymbol{\xi} \times \boldsymbol{B}\right) \cdot \frac{\partial f}{\partial \boldsymbol{\xi}}. \qquad (3.52)$$

This is conceptually similar to the "BFF" approach described in Section C.2 of Chapter V of [37] and proposed by [38] for Lattice-Boltzmann simulations. From equation (3.52) the characteristics are given by the solution:

$$\frac{d\boldsymbol{x}}{dt} = \boldsymbol{\xi}_0, \qquad (3.53)$$

$$\frac{d\boldsymbol{\xi}}{dt} = 0, \qquad (3.54)$$

which produces linear trajectories as shown by the diagram in Figure 3.3.

Figure 3.3: Schematic of a hypothetical particle trajectory in phase space based on equation (3.52)

To obtain integral solution along characteristics for $f(t)$, we can employ a similar pro-

cedure to that found in Kogan [39], pages 73–83. From equation (3.52), we multiply both sides by $e^{t/\tau}$:

$$e^{t/\tau}\frac{df}{dt} = e^{t/\tau}\left[\left(\frac{g-f}{\tau} - \frac{\boldsymbol{U}_\beta}{\tau_\beta}\cdot\frac{\partial f}{\partial\boldsymbol{\xi}} - \frac{q}{m}\left(\boldsymbol{E}+\boldsymbol{\xi}\times\boldsymbol{B}\right)\cdot\frac{\partial f}{\partial\boldsymbol{\xi}}\right)\right]. \qquad (3.55)$$

From equation (3.52) we obtain the following,

$$\frac{d}{dt}\left(e^{t/\tau}f\right) = e^{t/\tau}\frac{e^{t/\tau}}{\tau}g - \tau\frac{e^{t/\tau}}{\tau}\left[\frac{\boldsymbol{U}_\beta}{\tau_\beta}\cdot\frac{\partial f}{\partial\boldsymbol{\xi}} + \frac{q}{m}\left(\boldsymbol{E}+\boldsymbol{\xi}\times\boldsymbol{B}\right)\cdot\frac{\partial f}{\partial\boldsymbol{\xi}}\right], \qquad (3.56)$$

from which we can obtain equation (3.57) in a straightforward manner, assuming that the trajectory is linear.

$$f(\boldsymbol{x},\boldsymbol{\xi},t) = \frac{1}{\tau}\int_0^t g(\boldsymbol{x}',\boldsymbol{\xi}',t')e^{-(t-t')/\tau}dt' - \frac{1}{\tau}\int_0^t \frac{\tau}{\tau_\beta}\boldsymbol{U}_\beta\cdot\boldsymbol{\nabla}_{\boldsymbol{\xi}'}f(\boldsymbol{x}',\boldsymbol{\xi}',t')e^{-(t-t')/\tau}dt'$$
$$- \frac{1}{\tau}\int_0^t \tau\frac{q}{m}\left(\boldsymbol{E}+\boldsymbol{\xi}'\times\boldsymbol{B}\right)\cdot\boldsymbol{\nabla}_{\boldsymbol{\xi}'}f(\boldsymbol{x}',\boldsymbol{\xi}',t')e^{-(t-t')/\tau}dt' + e^{-t/\tau}f(\boldsymbol{x}_0,\boldsymbol{\xi}_0,0), \quad (3.57)$$

Here we note that $\boldsymbol{x}_0$ and $\boldsymbol{\xi}_0$ are the particle position and velocity at time $t = 0$. Further, we adopt the convention that $\boldsymbol{x} = 0$ at time t, while at time $0 < t' < t$ the particle position and velocity are $\boldsymbol{x}'$ and $\boldsymbol{\xi}'$. Here we recall that the phase space trajectories of $\boldsymbol{x}$ and $\boldsymbol{\xi}$ are determined by equations (3.53) and (3.54), which yield $\boldsymbol{\xi}' = \boldsymbol{\xi}_0 = \boldsymbol{\xi}$, and $\boldsymbol{x}' = 0 - \boldsymbol{\xi}(t-t')$, $\boldsymbol{x}_0 = 0 - \boldsymbol{\xi}t$. For the current development, it is assumed that $\boldsymbol{U}_\beta$, $\boldsymbol{E}$, and $\boldsymbol{B}$ are constant during the TFPGKS flux evolution. This is likely not an appropriate assumption for all flows, but has been utilized here as it greatly simplifies the overall development.

To obtain $g(\boldsymbol{x}',\boldsymbol{\xi},t')$, $f(\boldsymbol{x}',\boldsymbol{\xi},t')$, we utilize the Chapman Enskog expansion and a Taylor expansion in space and time near $t = 0$ and $\boldsymbol{x} = 0$. This assumes that $\boldsymbol{x}'$ and t' are much smaller than the macroscopic timescales of interest. Note that the timescale t' should be shorter than the inverse gyration frequency. However, it is not necessary that $t' < \tau$ because the dissipation in the TFPGKS scheme is determined by collisions (τ), and the effect of the

28

evolutionary time t on the viscous solution is minimal [12, 13, 32].

$$g(\boldsymbol{x}', \boldsymbol{\xi}, t') \approx g(0, \boldsymbol{\xi}, 0) - (t - t')\boldsymbol{\xi} \cdot \frac{\partial g}{\partial \boldsymbol{x}} + t'\frac{\partial g}{\partial t} \tag{3.58}$$

$$f(\boldsymbol{x}', \boldsymbol{\xi}, t') \approx g(\boldsymbol{x}', \boldsymbol{\xi}, t') + e^{-t'/\tau} f^{(1)} \tag{3.59}$$

In equations (3.58) and (3.59) g and $f^{(1)}$ are taken at $\boldsymbol{x} = 0$ and $t = 0$. The first order correction $f^{(1)}$ – which is obtained from the Chapman Enskog expansion – has a pre-factor $e^{-t'/\tau}$ to account for exponential decay of the non-equilibrium portion of the initial condition. That is, $f(0, \boldsymbol{\xi}, 0) = g(0, \boldsymbol{\xi}, 0) + f^{(1)}$, but for large t' relative to τ we have $\lim_{t' \gg \tau} f(\boldsymbol{x}', \boldsymbol{\xi}, t') \to g(\boldsymbol{x}', \boldsymbol{\xi}, t')$.

$$
\begin{aligned}
f(\boldsymbol{x}, \boldsymbol{\xi}, t) = & \frac{1}{\tau} \int_0^t \left(g - (t - t')\boldsymbol{\xi} \cdot \frac{\partial g}{\partial \boldsymbol{x}} + t'\frac{\partial g}{\partial t} \right) e^{-(t-t')/\tau} dt' \\
& - \frac{1}{\tau} \int_0^t \frac{\tau}{\tau_\beta} \boldsymbol{U}_\beta \cdot \boldsymbol{\nabla}_{\boldsymbol{\xi}'} \left(g - (t - t')\boldsymbol{\xi} \cdot \frac{\partial g}{\partial \boldsymbol{x}} + t'\frac{\partial g}{\partial t} + e^{-t'/\tau} f^{(1)} \right) e^{-(t-t')/\tau} dt' \\
& - \frac{1}{\tau} \int_0^t \tau \frac{q}{m} \left(\boldsymbol{E} + \boldsymbol{\xi} \times \boldsymbol{B} \right) \cdot \boldsymbol{\nabla}_{\boldsymbol{\xi}'} \left(g - (t - t')\boldsymbol{\xi} \cdot \frac{\partial g}{\partial \boldsymbol{x}} + t'\frac{\partial g}{\partial t} + e^{-t'/\tau} f^{(1)} \right) e^{-(t-t')/\tau} dt' \\
& + e^{-t/\tau} \left(g - t\boldsymbol{\xi} \cdot \frac{\partial g}{\partial \boldsymbol{x}} + f^{(1)} \right), \quad (3.60)
\end{aligned}
$$

Inserting the expansions of equations (3.58) and (3.59) into equation (3.57) we obtain equation (3.60). Integrating equation (3.60) over t', this produces for $f(\boldsymbol{\xi}, t)$:

$$
\begin{aligned}
f(\boldsymbol{\xi}, t) = & \left(g \left[1 - e^{-t/\tau} \right] - \left[\tau - e^{-t/\tau}(t + \tau) \right] \boldsymbol{\xi} \cdot \frac{\partial g}{\partial \boldsymbol{x}} + \left[t + \tau(e^{-t/\tau} - 1) \right] \frac{\partial g}{\partial t} \right) \\
& - \tau \left[\frac{q}{m} \left(\boldsymbol{E}' + \boldsymbol{c} \times \boldsymbol{B} \right) + \frac{\boldsymbol{U}_\beta}{\tau_\beta} \right] \cdot \frac{\partial}{\partial \boldsymbol{\xi}} \left(g \left[1 - e^{-t/\tau} \right] - \left[\tau - e^{-t/\tau}(t + \tau) \right] \boldsymbol{\xi} \cdot \frac{\partial g}{\partial \boldsymbol{x}} \right. \\
& \left. + \left[t + \tau(e^{-t/\tau} - 1) \right] \frac{\partial g}{\partial t} + \frac{t}{\tau} e^{-t/\tau} f^{(1)} \right) + e^{-t/\tau} \left(g - t\boldsymbol{\xi} \cdot \frac{\partial g}{\partial \boldsymbol{x}} + f^{(1)} \right). \quad (3.61)
\end{aligned}
$$

Recall we have taken our coordinate system to be such that $\boldsymbol{x} = 0$ is the origin. Equation

29

(3.61) can be easily be rearranged:

$$f(\boldsymbol{\xi}, t) = \left(g + t\frac{\partial g}{\partial t} - \tau \left[1 - e^{-t/\tau} \right] \left(\frac{\partial g}{\partial t} + \boldsymbol{\xi} \cdot \frac{\partial g}{\partial \boldsymbol{x}} \right) + e^{-t/\tau} f^{(1)} \right)$$
$$- \tau \left[\frac{q}{m} \left(\boldsymbol{E'} + \boldsymbol{c} \times \boldsymbol{B} \right) + \frac{\boldsymbol{U}_\beta}{\tau_\beta} \right] \cdot \frac{\partial}{\partial \boldsymbol{\xi}} \left(g \left[1 - e^{-t/\tau} \right] - \left[\tau - e^{-t/\tau}(t + \tau) \right] \boldsymbol{\xi} \cdot \frac{\partial g}{\partial \boldsymbol{x}} \right.$$
$$\left. + \left[t + \tau(e^{-t/\tau} - 1) \right] \frac{\partial g}{\partial t} + \frac{t}{\tau} e^{-t/\tau} f^{(1)} \right). \quad (3.62)$$

In practice our interest will be in the accumulated (or integrated) effects of f changing over time. Thus, we will integrate $f(t)$ over time from $t = 0$ to $t = \Delta t$,

$$\int_0^{\Delta t} f(\boldsymbol{\xi}, t)dt = \int_0^{\Delta t} \left\{ \left(g + t\frac{\partial g}{\partial t} - \tau \left[1 - e^{-t/\tau} \right] \left(\frac{\partial g}{\partial t} + \boldsymbol{\xi} \cdot \frac{\partial g}{\partial \boldsymbol{x}} \right) + e^{-t/\tau} f^{(1)} \right) \right.$$
$$- \tau \left[\frac{q}{m} \left(\boldsymbol{E'} + \boldsymbol{c} \times \boldsymbol{B} \right) + \frac{\boldsymbol{U}_\beta}{\tau_\beta} \right] \cdot \frac{\partial}{\partial \boldsymbol{\xi}} \left(g \left[1 - e^{-t/\tau} \right] - \left[\tau - e^{-t/\tau}(t + \tau) \right] \boldsymbol{\xi} \cdot \frac{\partial g}{\partial \boldsymbol{x}} \right.$$
$$\left. \left. + \left[t + \tau(e^{-t/\tau} - 1) \right] \frac{\partial g}{\partial t} + \frac{t}{\tau} e^{-t/\tau} f^{(1)} \right) \right\} dt, \quad (3.63)$$

which gives us

$$\overline{f}(\boldsymbol{\xi}) \equiv \int_0^{\Delta t} f(\boldsymbol{\xi}, t)dt = \Delta t \left\{ \left(g + \frac{\Delta t}{2}\frac{\partial g}{\partial t} - \tau \left[1 - \frac{\tau}{\Delta t} \left(1 - e^{-\Delta t/\tau} \right) \right] \left(\frac{\partial g}{\partial t} + \boldsymbol{\xi} \cdot \frac{\partial g}{\partial \boldsymbol{x}} \right) \right. \right.$$
$$+ \frac{\tau}{\Delta t} \left(1 - e^{-\Delta t/\tau} \right) f^{(1)} \right) - \tau \left[\frac{q}{m} \left(\boldsymbol{E'} + \boldsymbol{c} \times \boldsymbol{B} \right) + \frac{\boldsymbol{U}_\beta}{\tau_\beta} \right] \cdot \frac{\partial}{\partial \boldsymbol{\xi}} \left(g \left[1 - \frac{\tau}{\Delta t} \left(1 - e^{-\Delta t/\tau} \right) \right] \right.$$
$$- \left[\tau - \frac{2\tau^2}{\Delta t} + \left(\tau + \frac{2\tau^2}{\Delta t} \right) e^{-\Delta t/\tau} \right] \boldsymbol{\xi} \cdot \frac{\partial g}{\partial \boldsymbol{x}} + \left[\frac{\Delta t}{2} - \tau + \frac{\tau^2}{\Delta t} \left(1 - e^{-\Delta t/\tau} \right) \right] \frac{\partial g}{\partial t}$$
$$\left. \left. + \left[\frac{\tau}{\Delta t} \left(1 - e^{-\Delta t/\tau} \right) - e^{-\Delta t/\tau} \right] f^{(1)} \right) \right\}. \quad (3.64)$$

Equation (3.64) is the final expression for the "time-evolved" distribution $f(t)$ from which the TFPGKS fluxes are calculated.

30

3.3 Moments Closure and Formation of Macroscopic Fluxes

Recall the equation for $f(t)$ – Eq. (3.62) – and its temporally integrated form – Eq. (3.64). If we represent the moment for flux of a quantity, we take $\int \psi \boldsymbol{\xi} f d\boldsymbol{\xi}$. That is, for the flux of mass, we take the first moment of f (and so on for higher moments),

$$\int_0^{\Delta t} F_1^\rho(t)dt \equiv \bar{F}_1^\rho = \int_0^{\Delta t} \left(\int \xi_1 f(\boldsymbol{\xi}, t)d\boldsymbol{\xi} \right) dt = \int \xi_1 \bar{f}(\boldsymbol{\xi})d\boldsymbol{\xi}. \qquad (3.65)$$

If for the fluxes of mass, momentum, and energy we define ψ where $\psi \in [1, \xi_k, \xi^2/2]$ then the integrated moment $\frac{1}{\tau_0} \int_0^{\tau_0} F_k^\psi(t)dt \equiv \bar{F}_k^\psi$ becomes

$$\bar{F}_k^\psi \equiv \int \psi \xi_k \bar{f}(\boldsymbol{\xi})d\boldsymbol{\xi} =$$

$$\Delta t \int \psi \xi_k \left\{ \left(g + \frac{\Delta t}{2} \frac{\partial g}{\partial t} - \tau \left[1 - \frac{\tau}{\Delta t} \left(1 - e^{-\Delta t/\tau} \right) \right] \left(\frac{\partial g}{\partial t} + \boldsymbol{\xi} \cdot \frac{\partial g}{\partial \boldsymbol{x}} \right) \right. \right.$$

$$+ \frac{\tau}{\Delta t} \left(1 - e^{-\Delta t/\tau} \right) f^{(1)} \right) - \tau \left[\frac{q}{m} \left(\boldsymbol{E}' + \boldsymbol{c} \times \boldsymbol{B} \right) + \frac{\boldsymbol{U}_\beta}{\tau_\beta} \right] \cdot \frac{\partial}{\partial \boldsymbol{\xi}} \left(g \left[1 - \frac{\tau}{\Delta t} \left(1 - e^{-\Delta t/\tau} \right) \right] \right)$$

$$- \left[\tau - \frac{2\tau^2}{\Delta t} + \left(\tau + \frac{2\tau^2}{\Delta t} \right) e^{-\Delta t/\tau} \right] \boldsymbol{\xi} \cdot \frac{\partial g}{\partial \boldsymbol{x}} + \left[\frac{\Delta t}{2} - \tau + \frac{\tau^2}{\Delta t} \left(1 - e^{-\Delta t/\tau} \right) \right] \frac{\partial g}{\partial t}$$

$$\left. + \left[\frac{\tau}{\Delta t} \left(1 - e^{-\Delta t/\tau} \right) - e^{-\Delta t/\tau} \right] f^{(1)} \right) \right\} d\boldsymbol{\xi}. \qquad (3.66)$$

For convenience we define $\theta \equiv \psi \xi_k$, and define γ_k using equations (3.67) – (3.71) to replace terms involving τ and Δt in equation (3.66):

$$\gamma_1 \equiv \int_0^{\Delta t} (e^{-t/\tau})dt = \tau \left(1 - e^{-\Delta t/\tau} \right), \qquad (3.67)$$

$$\gamma_2 \equiv \int_0^{\Delta t} (1 - e^{-t/\tau})dt = \Delta t - \tau \left(1 - e^{-\Delta t/\tau} \right), \qquad (3.68)$$

$$\gamma_3 \equiv \int_0^{\Delta t} (\tau - e^{-t/\tau}(t + \tau))dt = \left[\tau \Delta t \left(1 + e^{-\Delta t/\tau} \right) - 2\tau^2 \left(1 - e^{-\Delta t/\tau} \right) \right], \qquad (3.69)$$

$$\gamma_4 \equiv \int_0^{\Delta t} (t + \tau(e^{-t/\tau} - 1))dt = \left[\frac{\Delta t^2}{2} - \tau \Delta t + \tau^2 \left(1 - e^{-\Delta t/\tau} \right) \right], \qquad (3.70)$$

$$\gamma_5 \equiv = \int_0^{\Delta t} (te^{-t/\tau})dt = \tau \left(1 - e^{-\Delta t/\tau} \right) - \Delta t e^{-\Delta t/\tau}. \qquad (3.71)$$

31

Substituting the γ_k into equation (3.66) gives us

$$\bar{F}_k^\psi = \int \theta \left\{ \left(g\Delta t + \frac{\Delta t^2}{2}\frac{\partial g}{\partial t} - \tau\gamma_2 \left(\frac{\partial g}{\partial t} + \boldsymbol{\xi}\cdot\frac{\partial g}{\partial \boldsymbol{x}}\right) \right.\right.$$
$$+ \gamma_1 f^{(1)}\right) - \tau\left[\frac{q}{m}\left(\boldsymbol{E'} + \boldsymbol{c}\times\boldsymbol{B}\right) + \frac{\boldsymbol{U}_\beta}{\tau_\beta}\right]\cdot\frac{\partial}{\partial\boldsymbol{\xi}}\left(g\gamma_2\right.$$
$$\left.\left. - \gamma_3\boldsymbol{\xi}\cdot\frac{\partial g}{\partial\boldsymbol{x}} + \gamma_4\frac{\partial g}{\partial t} + \gamma_5 f^{(1)}\right)\right\}d\boldsymbol{\xi}. \quad (3.72)$$

If we define $\langle\theta\rangle \equiv \int \theta g(\boldsymbol{\xi})d\boldsymbol{\xi}$, and recall that $\phi^{(1)} \equiv \frac{f^{(1)}}{g}$, then equation (3.72) may be written as the following:

$$\bar{F}_k^\psi = \left(\langle\theta\rangle\Delta t + \frac{\Delta t^2}{2}\langle\theta\frac{\partial\ln g}{\partial t}\rangle - \tau\gamma_2\left(\langle\theta\frac{\partial\ln g}{\partial t}\rangle + \langle\theta\boldsymbol{\xi}\cdot\frac{\partial\ln g}{\partial\boldsymbol{x}}\rangle\right) + \gamma_1\langle\theta\phi^{(1)}\rangle\right)$$
$$+ \int \tau\left[\left[\frac{q}{m}\left(\boldsymbol{E'}+\boldsymbol{c}\times\boldsymbol{B}\right) + \frac{\boldsymbol{U}_\beta}{\tau_\beta}\right]\cdot\frac{\partial\theta}{\partial\boldsymbol{\xi}}\right]\left(g\gamma_2 - \gamma_3 g\boldsymbol{\xi}\cdot\frac{\partial\ln g}{\partial\boldsymbol{x}} + \gamma_4 g\frac{\partial\ln g}{\partial t} + \gamma_5 g\phi^{(1)}\right)d\boldsymbol{\xi}.$$
$$(3.73)$$

From equation (3.73), if we define the total acceleration $\boldsymbol{F}$ as $\boldsymbol{F} \equiv \frac{q}{m}\boldsymbol{E'} + \frac{\boldsymbol{U}_\beta}{\tau_\beta} + \frac{q}{m}\boldsymbol{c}\times\boldsymbol{B}$, then we may further simplify the notation:

$$\bar{F}_k^\psi = \left(\langle\theta\rangle\Delta t + \frac{\Delta t^2}{2}\langle\theta\frac{\partial\ln g}{\partial t}\rangle - \tau\gamma_2\left(\langle\theta\frac{\partial\ln g}{\partial t}\rangle + \langle\theta\boldsymbol{\xi}\cdot\frac{\partial\ln g}{\partial\boldsymbol{x}}\rangle\right) + \gamma_1\langle\theta\phi^{(1)}\rangle\right)$$
$$+ \tau\left(\langle\boldsymbol{F}\cdot\frac{\partial\theta}{\partial\boldsymbol{\xi}}\rangle\gamma_2 - \gamma_3\langle\boldsymbol{F}\cdot\frac{\partial\theta}{\partial\boldsymbol{\xi}}\boldsymbol{\xi}\cdot\frac{\partial\ln g}{\partial\boldsymbol{x}}\rangle + \gamma_4\langle\boldsymbol{F}\cdot\frac{\partial\theta}{\partial\boldsymbol{\xi}}\frac{\partial\ln g}{\partial t}\rangle + \gamma_5\langle\boldsymbol{F}\cdot\frac{\partial\theta}{\partial\boldsymbol{\xi}}\phi^{(1)}\rangle\right). \quad (3.74)$$

Equation (3.74) is the final general expression of the TFPGKS flux which must be calculated (2.19) – (2.24).

In sections 6.1 and 6.5, the TFPGKS flux in equation (3.74) is compared to a version which neglects to account both for the acceleration in the MoC solution and for the additional effects of magnetization in the solution for $f^{(1)}$. The latter is similar to previously implemented approaches of GKS for MHD and plasmas [18, 21]. To simplify the nomencla-

ture, the TFPGKS scheme will be termed the "Coupled" scheme to refer to the coupling of the electromagnetic acceleration to the GKS flux calculation, while the latter approach will be referred to as the "Uncoupled" scheme.

While equation (3.74) is accurate given the assumptions we have made so far, it is not necessarily amenable to direct use in a numerical scheme. This is because care must be taken in how the moments of the TFPGKS flux are calculated when considered for a discretized set of fluid variables on a numerical grid. The process of extending the theoretical framework discussed in this chapter to numerical implementation is discussed in detail in Chapter 4.

4. NUMERICAL IMPLEMENTATION

In previous Chapters we developed the fundamental formulation for calculating the GKS fluxes and discussed the complete set of equations that must be self-consistently solved to evolve the two-fluid plasma system. In this Chapter we discuss the various considerations and strategies for numerical implementation. This includes:

1. Representing the various gradients of the Maxwellian g that appear in the TFPGKS flux – $\frac{\partial g}{\partial t}$, $\frac{\partial g}{\partial \boldsymbol{x}}$ – so as to be more amenable to discretization.

2. Selecting a method of reconstructing the discrete flow field – which resides at cell centers e.g., i, $i + 1$ – to calculate the TFPGKS fluxes at cell interfaces, e.g., $i + \frac{1}{2}$.

3. Evolving Maxwell's equations – Eq. (2.15) and (2.16) – in such a way as to self-consistently adhere to Gauss's laws for the electric and magnetic fields – Eq. (2.17) and (2.18).

4. Non-dimensionalization of the governing equations to improve numerical tractability.

4.1 Discrete Formulation of TFPGKS Flux

In this section, we discuss the approach for applying the analytic TFPGKS flux from Chapter 3 to a discrete system where the continuum flow variables must be reconstructed to calculate the flux between cells. Recall that in the TFPGKS scheme while we are evolving the governing equations for continuum variables – ρ, $\rho\boldsymbol{u}$, and ε – of each species, our aim is to use the gas-kinetic scheme to calculate the fluxes from a kinetic perspective. While in principle it may be possible to apply a similar strategy to calculate the source terms of the governing equations, for the current work we will calculate the source terms using their continuum expressions.

4.1.1 Temporal Integration of TFPGKS Flux

First, we recall equation (3.61) for the time-dependent distribution $f(\boldsymbol{\xi}, t)$. For the TF-PGKS flux, we take the moment of $f(\boldsymbol{\xi}, t)$ on $\boldsymbol{\xi}$.

$$
\begin{aligned}
F_k^{\psi_\sigma}(t) = \Bigg\langle g\bigg(&\left[1 - e^{-t/\tau}\right] - \left[\tau - e^{-t/\tau}(t + \tau)\right]\boldsymbol{\xi} \cdot \frac{\partial \ln g}{\partial \boldsymbol{x}} \\
&+ \left[t + \tau(e^{-t/\tau} - 1)\right]\frac{\partial \ln g}{\partial t}\bigg)(\xi_k\psi_\sigma) + g\bigg(\left[1 - e^{-t/\tau}\right] - \left[\tau - e^{-t/\tau}(t + \tau)\right]\boldsymbol{\xi} \cdot \frac{\partial \ln g}{\partial \boldsymbol{x}} \\
&+ \left[t + \tau(e^{-t/\tau} - 1)\right]\frac{\partial \ln g}{\partial t} + \frac{t}{\tau}e^{-t/\tau}\phi^{(1)}\bigg)\left(\frac{\tau q}{m}(\boldsymbol{E} + \boldsymbol{\xi} \times \boldsymbol{B}) + \frac{\tau \boldsymbol{U}}{\tau_\beta}\right) \cdot \boldsymbol{\nabla}_{\boldsymbol{\xi}}\Big((\xi_k\psi_\sigma)\Big) \\
&+ e^{-t/\tau}g\left(1 - t\boldsymbol{\xi} \cdot \frac{\partial \ln g}{\partial \boldsymbol{x}} + \phi^{(1)}\right)(\xi_k\psi_\sigma) \Bigg\rangle \quad (4.1)
\end{aligned}
$$

Equation (4.1) represents the k-th component of flux of the conserved quantities, where the brackets are defined $\langle \cdot \rangle \equiv \int (\cdot)\, d\boldsymbol{\xi}$ to indicate the moment over $\boldsymbol{\xi}$. To obtain the total flux over a timestep Δt, equation (4.1) must be integrated over t, from which we define $\bar{F}_k^{\psi_\sigma} \equiv \int_0^{\Delta t} F_k^{\psi_\sigma}(t)dt$.

$$
\begin{aligned}
\bar{F}_k^{\psi_\sigma} = \Bigg\langle &g\left(\gamma_2 - \gamma_3\boldsymbol{\xi} \cdot \frac{\partial \ln g}{\partial \boldsymbol{x}} + \gamma_4\frac{\partial \ln g}{\partial t}\right)(\xi_k\psi_\sigma) \\
&+ g\left(\gamma_2 - \gamma_3\boldsymbol{\xi} \cdot \frac{\partial \ln g}{\partial \boldsymbol{x}} + \gamma_4\frac{\partial \ln g}{\partial t} + \gamma_5\phi^{(1)}\right)\left(\frac{\tau q}{m}(\boldsymbol{E} + \boldsymbol{\xi} \times \boldsymbol{B}) + \frac{\tau \boldsymbol{U}}{\tau_\beta}\right) \cdot \boldsymbol{\nabla}_{\boldsymbol{\xi}}\Big((\xi_k\psi_\sigma)\Big) \\
&+ g\left(\gamma_1 - \tau\gamma_5\boldsymbol{\xi} \cdot \frac{\partial \ln g}{\partial \boldsymbol{x}} + \gamma_1\phi^{(1)}\right)(\xi_k\psi_\sigma) \Bigg\rangle \quad (4.2)
\end{aligned}
$$

The temporally integrated flux $\bar{F}_k^{\psi_\sigma}$ is shown in equation (4.2), where we have reintroduced the γ_k defined in equations (3.67) – (3.71).

$$
\bar{F}_k^{\psi} = \left(\langle \theta \rangle + \frac{\tau_0}{2} \langle \theta \frac{\partial \ln g}{\partial t} \rangle - \tau \gamma_2 \left(\langle \theta \frac{\partial \ln g}{\partial t} \rangle + \langle \theta \boldsymbol{\xi} \cdot \frac{\partial \ln g}{\partial \boldsymbol{x}} \rangle \right) \right.
$$
$$
\left. + \gamma_1 \langle \theta \phi^{(1)} \rangle \right) + \tau \left(\langle \boldsymbol{F} \cdot \frac{\partial \theta}{\partial \boldsymbol{\xi}} \rangle \gamma_2 - \gamma_3 \langle \boldsymbol{F} \cdot \frac{\partial \theta}{\partial \boldsymbol{\xi}} \boldsymbol{\xi} \cdot \frac{\partial \ln g}{\partial \boldsymbol{x}} \rangle + \gamma_4 \langle \boldsymbol{F} \cdot \frac{\partial \theta}{\partial \boldsymbol{\xi}} \frac{\partial \ln g}{\partial t} \rangle + \gamma_5 \langle \boldsymbol{F} \cdot \frac{\partial \theta}{\partial \boldsymbol{\xi}} \phi^{(1)} \rangle \right)
$$

$$(4.3)$$

4.1.2   Construction of TFPGKS Gradient Coefficients

Note that in equation (4.2) we must determine quantities such as $\frac{\partial \ln g}{\partial \boldsymbol{x}}$. However, in the numerical solution of the flow dynamics, we only know about the fluid variables – $[\rho, \rho \boldsymbol{u}, \varepsilon]$ – and their gradients in space. Thus, in the TFPGKS procedure we define so-called "gradient coefficients" $\boldsymbol{a} \equiv \frac{\partial \ln g}{\partial \boldsymbol{x}}$ and $A \equiv \frac{\partial \ln g}{\partial t}$, which can be uniquely determined from the gradients of the fluid variables [12], where the coefficients $\boldsymbol{a}$ and A are in fact polynomials in $\boldsymbol{\xi}$. Recall the the vector $\psi = [1, \boldsymbol{\xi}, \frac{1}{2} \boldsymbol{\xi}^2]$ which produces the macroscopic conserved variables via moments on g: $\Psi \equiv \int \psi g d\boldsymbol{\xi} = [\rho, \rho \boldsymbol{u}, \varepsilon]$. Designating the components of ψ as ψ_β, the gradient coefficients can be expressed as $\boldsymbol{a} = \boldsymbol{a}_\beta \psi_\beta$ and $A = A_\beta \psi_\beta$, such that $\frac{\partial g}{\partial \boldsymbol{x}} \equiv g \boldsymbol{a}_\beta \psi_\beta$ and $\frac{\partial g}{\partial t} \equiv g A_\beta \psi_\beta$.

$$
\bar{F}_k^{\psi_\sigma} = \left\langle g \left(\gamma_2 - \gamma_3 \boldsymbol{\xi} \cdot \boldsymbol{a}_\beta \psi_\beta + \gamma_4 A_\beta \psi_\beta \right) \psi_\sigma \right.
$$
$$
+ g \left(\gamma_2 - \gamma_3 \boldsymbol{\xi} \cdot \boldsymbol{a}_\beta \psi_\beta + \gamma_4 A_\beta \psi_\beta + \gamma_5 \phi^{(1)} \right) \left(\frac{\tau q}{m} \left(\boldsymbol{E} + \boldsymbol{\xi} \times \boldsymbol{B} \right) + \frac{\tau \boldsymbol{U}}{\tau_\beta} \right) \cdot \boldsymbol{\nabla}_{\boldsymbol{\xi}} \left(\psi_\sigma \right)
$$
$$
\left. + g \left(\gamma_1 - \tau \gamma_5 \boldsymbol{\xi} \cdot \boldsymbol{a}_\beta \psi_\beta + \gamma_1 \phi^{(1)} \right) \psi_\sigma \right\rangle \quad (4.4)
$$

The $\boldsymbol{a}_\beta$ and A_β are constants with respect to $\boldsymbol{\xi}$. The $\boldsymbol{a}_\beta$ can be obtained directly and

uniquely from the gradients of the conserved variables:

$$\frac{\partial \Psi_\alpha}{\partial \boldsymbol{x}} = \frac{\partial}{\partial \boldsymbol{x}} \int \psi_\alpha g d\boldsymbol{\xi} = \int \psi_\alpha \frac{\partial g}{\partial \boldsymbol{x}} d\boldsymbol{\xi} = \int \psi_\alpha g \boldsymbol{a}_\beta \psi_\beta d\boldsymbol{\xi} \tag{4.5}$$

In equation (4.5), we observe that the gradients $\frac{\partial \Psi_\alpha}{\partial \boldsymbol{x}}$ may be obtained from the spatial distri-
bution of the flow variables. Further, the $\boldsymbol{a}_\beta$ are constants with respect to the moments on $\boldsymbol{\xi}$.
If we define $M_{\alpha\beta} \equiv \int g \psi_\alpha \psi_\beta d\boldsymbol{\xi}$, then the coefficients $\boldsymbol{a}_\beta$ are determined by its inverse.

$$\boldsymbol{a}_\beta = M_{\alpha\beta}^{-1} \frac{\partial \Psi_\alpha}{\partial \boldsymbol{x}} \tag{4.6}$$

In practice the quantity $M_{\alpha\beta}^{-1}$ in equation (4.6) may be determined analytically so that no
numerical matrix inversion needs to be done (see Appendix A).

To compute the coefficients A_β, we recall the first-order non-equilibrium correction to
the distribution $f^{(1)}$, equation (4.7).

$$f^{(1)} + \varpi \boldsymbol{c} \times \hat{\boldsymbol{b}} \cdot \frac{\partial f^{(1)}}{\partial \boldsymbol{\xi}} = -\tau g \left[\frac{\partial \ln g}{\partial t} + \boldsymbol{\xi} \cdot \frac{\partial \ln g}{\partial \boldsymbol{x}} + \frac{q}{m} \boldsymbol{E}' \cdot \frac{\partial \ln g}{\partial \boldsymbol{\xi}} + \frac{\boldsymbol{U}_\beta}{\tau_\beta} \cdot \frac{\partial \ln g}{\partial \boldsymbol{\xi}} \right] \tag{4.7}$$

Replacing the gradients of g with their corresponding gradient coefficients, and recalling for
the Maxllian g we have $\frac{\partial g}{\partial \boldsymbol{\xi}} = -\frac{m}{kT} (\boldsymbol{\xi} - \boldsymbol{u}) g$, we get:

$$f^{(1)} + \varpi \boldsymbol{c} \times \hat{\boldsymbol{b}} \cdot \frac{\partial f^{(1)}}{\partial \boldsymbol{\xi}} = -\tau g \left[A_\beta \psi_\beta + \boldsymbol{\xi} \cdot \boldsymbol{a}_\beta \psi_\beta - \left(\frac{q}{m} \boldsymbol{E}' + \frac{\boldsymbol{U}_\beta}{\tau_\beta} \right) \cdot \frac{m}{kT} (\boldsymbol{\xi} - \boldsymbol{u}) \right]. \tag{4.8}$$

Note that $f^{(1)}$ does not make a contribution to the conserved variables Ψ_α. That is, $\Psi_\alpha \equiv$
$\int \psi_\alpha f d\boldsymbol{\xi} \approx \int \psi_\alpha g d\boldsymbol{\xi} + \int \psi_\alpha f^{(1)} d\boldsymbol{\xi} = \int \psi_\alpha g d\boldsymbol{\xi} - \int \psi_\alpha f^{(1)} d\boldsymbol{\xi} = 0.$

$$\int \psi_\alpha f^{(1)} d\boldsymbol{\xi} + \int \psi_\alpha \left(\varpi \boldsymbol{c} \times \hat{\boldsymbol{b}} \cdot \frac{\partial f^{(1)}}{\partial \boldsymbol{\xi}} \right) d\boldsymbol{\xi} =$$
$$-\tau \int \psi_\alpha \left[g A_\beta \psi_\beta + g \boldsymbol{\xi} \cdot \boldsymbol{a}_\beta \psi_\beta - g \left(\frac{q}{m} \boldsymbol{E}' + \frac{\boldsymbol{U}_\beta}{\tau_\beta} \right) \cdot \frac{m}{kT} (\boldsymbol{\xi} - \boldsymbol{u}) \right] d\boldsymbol{\xi} \tag{4.9}$$

From equation (4.9) we can obtain an equation which may be solved for A_β in terms of known quantities by observing that $\frac{\partial}{\partial \boldsymbol{\xi}}(\boldsymbol{c} \times \hat{\boldsymbol{b}}) = 0$ and recalling that $f \to 0$ as $\boldsymbol{\xi} \to \pm\infty$:

$$\int \psi_\alpha \left[g A_\beta \psi_\beta + g \boldsymbol{\xi} \cdot \boldsymbol{a}_\beta \psi_\beta - g \psi_\alpha \left(\frac{q}{m} \boldsymbol{E}' + \frac{\boldsymbol{U}_\beta}{\tau_\beta} \right) \cdot \frac{m}{kT} (\boldsymbol{\xi} - \boldsymbol{u}) \right] d\boldsymbol{\xi} = 0. \qquad (4.10)$$

From equation (4.10), we find:

$$A_\beta = -M_{\alpha\beta}^{-1} \left[\boldsymbol{a}_\beta \cdot \int g \boldsymbol{\xi} \psi_\alpha \psi_\beta d\boldsymbol{\xi} - \frac{m}{kT} \left(\frac{q}{m} \boldsymbol{E}' + \frac{\boldsymbol{U}_\beta}{\tau_\beta} \right) \cdot \int g \psi_\alpha (\boldsymbol{\xi} - \boldsymbol{u}) \, d\boldsymbol{\xi} \right]. \qquad (4.11)$$

This will give us the coefficients $\boldsymbol{a}_\beta$ and A_β in equation (4.4). However, note that we must still supply $\phi^{(1)}$, which to be useful for our TFPGKS flux construction must be given using the same gradient coefficients.

$$\phi^{(1)} = -\tau \left[A_\beta \psi_\beta + \xi_i a_\beta^i \psi_\beta - 2 \left(\frac{m}{2kT} \right) F_i (\xi_i - u_i) \right] \qquad (4.12)$$

Expressing Equation (3.26) – for the *unmagnetized* $\phi^{(1)}$ – in terms of the same gradient coefficients will produce equation (4.12). Note that we have returned to index notation for clarity, and defined $F_i \equiv \frac{q}{m} E_i' + \frac{U_{\beta,i}}{\tau_\beta}$. For the magnetized $\phi^{(1)}$, we seek to define $\phi^{(1)}$ so that it has a similar form to equation (4.12), like the parallelism between equations (3.33) and (3.48). Thus, we will define:

$$\phi^{(1)} = -\tau \left[B_\beta \psi_\beta + \xi_i b_\beta^i \psi_\beta - 2 \left(\frac{m}{2kT} \right) F_i^B (\xi_i - u_i) \right]. \qquad (4.13)$$

The quantities B_β, b_β^i, and F_i^B are "magnetized" versions of the quantities appearing in equation (4.12).

If we define $\beta \in [0, 4]$ and $i, j \in [1, 3]$, then it can be shown that the quantities b_β^i, B_β,

and F_i^B can be defined to be the following.

$$F_i^B \equiv \hat{\kappa}_{ij} F_j, \tag{4.14}$$

$$b_0^i \equiv \hat{\kappa}_{ij} a_0^j, \tag{4.15}$$

$$b_j^i \equiv \hat{M}_{ijkl} \left(a_l^k + 2a_4^k u_l \right) - 2b_4^i u_j, \tag{4.16}$$

$$b_4^i \equiv \hat{\kappa}_{ij} a_4^j. \tag{4.17}$$

Note that if we construct b_0^i, b_j^i, b_4^i, $F_{B,i}$ we may form B_0, B_i, B_4 via $\int \psi_\alpha f^{(1)} d\boldsymbol{\xi} = 0$. That is, we can obtain B_β in the same fashion as A_β, via equation (4.11):

$$B_\beta = -M_{\alpha\beta}^{-1} \left[\int \xi_i b_\beta^i \psi_\beta \psi_\sigma - \int 2(\frac{m}{2kT}) F_i^B (\xi_i - u_i) \psi_\sigma \right] \tag{4.18}$$

Here we will add that in the continuous limit, it can be shown that the expression in equation (4.13) will reduce to that of equation (3.48). However, for use in TFPGKS it is necessary to use equation (4.13) due to the use of reconstructed variables in the non-continuous case. Thus, for the TFPGKS flux with gradient coefficients we have in place of equation (4.2):

$$
\begin{aligned}
\bar{F}_k^{\psi_\sigma} = &\left\langle g \left(\gamma_2 - \gamma_3 \boldsymbol{\xi} \cdot \boldsymbol{a}_\beta \psi_\beta + \gamma_4 A_\beta \psi_\beta \right) \psi_\sigma + g \left(\gamma_2 - \gamma_3 \boldsymbol{\xi} \cdot \boldsymbol{a}_\beta \psi_\beta + \gamma_4 A_\beta \psi_\beta \right. \right. \\
&+ \gamma_5 \left\{ -\tau \left[B_\beta \psi_\beta + \xi_i b_\beta^i \psi_\beta - 2(\frac{m}{2kT}) F_i^B (\xi_i - u_i) \right] \right\} \left) \left(\frac{\tau q}{m} \left(\boldsymbol{E} + \boldsymbol{\xi} \times \boldsymbol{B} \right) + \frac{\tau \boldsymbol{U}}{\tau_\beta} \right) \cdot \boldsymbol{\nabla}_{\boldsymbol{\xi}} \left(\psi_\sigma \right) \right. \\
&+ g \left(\gamma_1 - \tau \gamma_5 \boldsymbol{\xi} \cdot \boldsymbol{a}_\beta \psi_\beta + \gamma_1 \left\{ -\tau \left[B_\beta \psi_\beta + \xi_i b_\beta^i \psi_\beta - 2(\frac{m}{2kT}) F_i^B (\xi_i - u_i) \right] \right\} \right) \psi_\sigma \right\rangle.
\end{aligned}
\tag{4.19}
$$

4.1.3 WENO Reconstruction and Left- and Right-Moment Calculation

On a discretized grid of cells, the fluid and electromagnetic variables are also discretized such that the value of e.g., ρ in a cell i is taken to be the "average" value of ρ within the cell which exists at the cell center. However, to calculate numerical flux between cells, the

value of the variables at the cell interfaces must be estimated. In the current work, this is done via a 5th order Weighted Essentially Non-Oscillatory (WENO) reconstruction scheme [40, 41], which has been implemented with GKS previously [10, 11, 22]. Kumar et al. [11] in particular deliver an excellent discussion of the WENO implementation used here. Figure
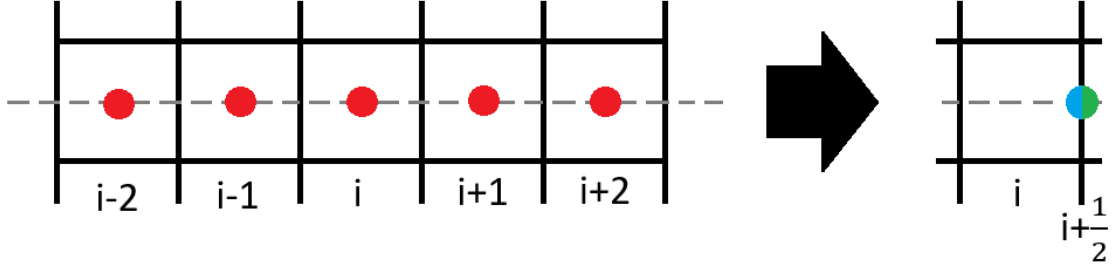
Figure 4.1: Qualitative schematic of WENO reconstruction

4.1 gives a schematic interpretation of how the WENO scheme takes a 5-cell stencil of cell-centered values and obtains left- and right- interpolated values to be used in constructing the TFPGKS flux.

The result of the reconstruction process takes Ψ at the locations $i - 2$ through $i + 2$ and gives us interpolated left- and right-values Ψ^l and Ψ^r at the cell interface $i + \frac{1}{2}$. From the reconstructed values of $\Psi^{l,r}$, e.g., $\rho^{l,r}, (\rho\boldsymbol{u})^{l,r}, \varepsilon^{l,r}$, we may obtain left- and right- values of the primitive variables $\rho^{l,r}, \boldsymbol{u}^{l,r}, T^{l,r}$. If we once again recall the definition of the Maxwellian g,

$$g = \rho \left(\frac{m}{2\pi kT} \right)^{3/2} e^{-\frac{m}{2kT}(\boldsymbol{\xi}-\boldsymbol{u})^2},$$

we see g is uniquely defined by ρ, $\boldsymbol{u}$, and T. Thus, $\rho^{l,r}, \boldsymbol{u}^{l,r}, T^{l,r}$ define local Maxwellians $g_{L,R}$ on either side of the interface. From this we define the non-equilibrium gas distribution

function f – which includes the contributions from $\phi^{(1)}$ – in equation (4.20).

$$f(t) = g^l \left[1 + a^{i,l}_\beta \psi_\beta x_i + A^l \psi_\beta t + e^{-t'/\tau} \phi^{(1),l} \right] H(\xi_1) +$$
$$g^r \left[1 + a^{i,r}_\beta \psi_\beta x_i + A^r_\beta \psi_\beta t + e^{-t'/\tau} \phi^{(1),r} \right] (1 - H(\xi_1)) \quad (4.20)$$

Note that equation (4.20) is defined for reconstruction along the x-direction, with the Heaviside function $H(x)$ applied to the particle velocity along x. The quantities $\phi^{(1),l}$ and $\phi^{(1),r}$ are defined as

$$\phi^{(1),r} = -\tau \left[B^r_\beta \psi_\beta + \xi_i b^{i,r}_\beta \psi_\beta - 2(\frac{m}{2kT^r}) F^{B,r}_i (\xi_i - u^r_i) \right]. \quad (4.21)$$

The construction of f_0 applies for most of the terms in equation (4.19) – the last three terms in equation (3.57).

The quantities $a^{l,r}_\beta$ and $A^{l,r}_\beta$ are defined as in equation (4.6) and (4.11). However, we define the left- and right- slopes for the variables in the x-direction in a slightly different manner. These slopes are defined in equations (4.22) and (4.23).

$$\frac{\partial \Psi^L}{\partial x} \approx \frac{\Psi^l_{i+\frac{1}{2}} - \Psi_i}{\Delta x/2} \quad (4.22)$$

$$\frac{\partial \Psi^R}{\partial x} \approx \frac{\Psi_{i+1} - \Psi^r_{i+\frac{1}{2}}}{\Delta x/2} \quad (4.23)$$

For the slopes perpendicular to the interface, a straightforward central finite difference approach can be used with the left- and right- reconstructed values. This approach is similar to that taken in [12]. The meaning of this approach with regards to the Maxwellian is that we assume the initial distribution and its slope perpendicular to the interface are discontinuous.

In addition to the non-equilibrium distribution f, the equilibrium distribution g is also defined. The distribution g is continuous at the cell interface and pertains to the terms resulting

from the first term in equation (3.57):

$$\Psi^0 \equiv \int \psi_\alpha g_0 d\boldsymbol{\xi} = \int_{\xi_1>0} \psi_\alpha g^l d\boldsymbol{\xi} + \int_{\xi_1<0} \psi_\alpha g^r d\boldsymbol{\xi}. \qquad (4.24)$$

The Maxwellian g_0 is defined by equation 4.24, where the half moments of g^l and g^r in velocity space perpendicular to the interface are combined. For the left-reconstructed distribution g^l, the particles with $\xi_1 > 0$ are taken because they are moving towards the interface, likewise for the right-constructed distribution g^r and the left-moving particles $\xi_1 < 0$. The underlying physical assumption is that these left- and right-moving particles combine in such a way as to "collapse" into the interface equilibrium state g_0 [13]. From this the equilibrium state g is defined as

$$g = g_0 \left[1 + \bar{a}_\beta^{1,l} \psi_\beta \xi_1 H(\xi_1) + \bar{a}_\beta^{1,r} \psi_\beta \xi_1 \left(1 - H(\xi_1) \right) + \bar{a}_\beta^2 \psi_\beta \xi_2 + \bar{a}_\beta^3 \psi_\beta \xi_3 + \bar{A} t \right]. \qquad (4.25)$$

The $\bar{a}_\beta$ and $\bar{A}_\beta$ quantities in equation (4.25) are defined similarly to $a_\beta^{l,r}$ and $A_\beta^{l,r}$. However, here only the slopes perpendicular to the interface are discontinuous. The left- and right- slopes are defined in equations (4.26) and (4.27).

$$\frac{\partial \Psi^{0,L}}{\partial x} \approx \frac{\Psi^0_{i+\frac{1}{2}} - \Psi_i}{\Delta x/2} \qquad (4.26)$$

$$\frac{\partial \Psi^{0,R}}{\partial x} \approx \frac{\Psi_{i+1} - \Psi^0_{i+\frac{1}{2}}}{\Delta x/2} \qquad (4.27)$$

Thus, the equilibrium distribution is continuous, but its slope perpendicular to the cell interface is discontinuous. The rationale behind this approach is the following:

1. The non-equilibrium distribution is discontinuous because it is based on the initial discontinuous state at the beginning of the time step.

2. The equilibrium distribution is continuous because it is assumed to have collapsed to a single state at the interface due to collisions.
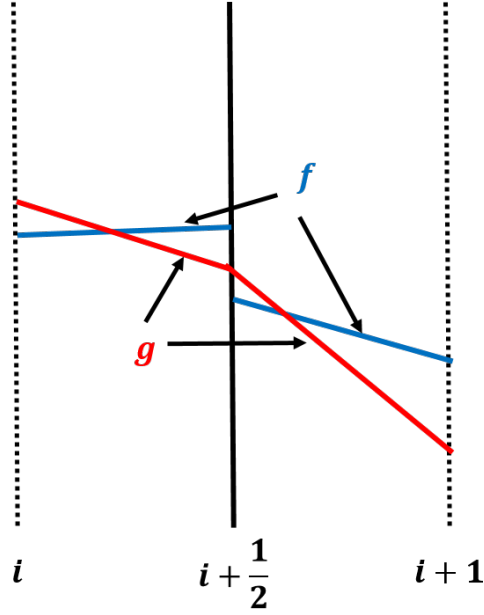
Figure 4.2: Schematic representation of the non-equilibrium distribution f and the equilibrium distribution g and their slopes at the interface $i + \frac{1}{2}$

The relationship between f and g in equations (4.20) and (4.25) is shown schematically in figure 4.2. From the discontinuous interface reconstruction, the final form of the flux from equation 4.19 may be determined. More detailed expressions of the flux terms to be implemented are given in Appendix B.

4.2 Prandtl Number Correction

As discussed in Chapter 2, one of the chief shortcomings of the BGK collision operator is that it assumes a Prandtl number of $Pr = 1$, which is not correct. To correct for this a Prandtl number "fix" may be applied [12]. To do this, the portion of the energy flux which corresponds to the heat flux is scaled by the appropriate Prandtl number which may be specified as a parameter. Recall that the Prandtl number is proportional to the ratio of viscosity and thermal conductivity, $Pr \propto \frac{\mu}{\kappa}$.

$$\boldsymbol{F}^{\varepsilon}_{fix} = \boldsymbol{F}^{\varepsilon} + \left(\frac{1}{Pr} - 1 \right) \boldsymbol{q} \tag{4.28}$$

43

The procedure to fix the energy flux for the correct Prandtl number is outlined in equation (4.28), wherein the energy flux is augmented by adding the "missing" portion of heat flux – for $Pr < 1$ – or by subtracting the "extra" heat flux – for $Pr > 1$.

4.3 Perfectly Hyperbolic Maxwell's (PHM) Equations

For a completely internally self-consistent system, Maxwell's equations for the electromagnetic fields must also be considered.

$$
\frac{\partial \boldsymbol{E}}{\partial t} = c^2 \boldsymbol{\nabla} \times \boldsymbol{B} - \frac{\boldsymbol{J}}{\epsilon_0}
$$
$$
\frac{\partial \boldsymbol{B}}{\partial t} = -\boldsymbol{\nabla} \times \boldsymbol{E}
$$
$$
\boldsymbol{\nabla} \cdot \boldsymbol{B} = 0
$$
$$
\boldsymbol{\nabla} \cdot \boldsymbol{E} = \frac{\rho_Q}{\epsilon_0}
$$

Equations (2.15) and (2.16) provide a means of temporally advancing the electromagnetic fields, given appropriate initial and boundary conditions. However, equations (2.18) and (2.17) place constraints on the electric and magnetic fields that must be obeyed. While it is true that these constraints will analytically be conserved by equations (2.15) and (2.16) if they are satisfied by the initial and boundary conditions. It is not guaranteed that they will be preserved in a discretized system. Failure to do so can lead to charge conservation violation and potentially the generation of spurious forces parallel to the magnetic field [42].

Enforcing the divergence constraints of equations (2.17) and (2.18) can be done by a variety of strategies. Toth provides a comprehensive overview of strategies for enforcing zero divergence in the magnetic field for MHD solutions [43]. Dedner et al. provide a scheme for "divergence cleaning" of the MHD system. It is also possible to design schemes which enforce zero divergence for the magnetic field at the level of the discretization [45].

The approach we have taken is that of Munz et al. in employing the so-called "Perfectly Hyperbolic" Maxwell's (PHM) equations [46, 47, 48]. The PHM equations directly incor-

porate the divergence constraints of equations (2.17) and (2.18) into the temporal evolution of the two-fluid system by introducing two additional variables ϕ and ψ which act as proxies for the divergence constraints – or "correction potentials" [4] – while being consistent with the overall hyperbolic structure of the two-fluid – Maxwell system.

$$\frac{\partial \boldsymbol{E}}{\partial t} = c^2 \boldsymbol{\nabla} \times \boldsymbol{B} - \frac{\boldsymbol{J}}{\epsilon_0} - c^2 \zeta_\phi \boldsymbol{\nabla} \phi \tag{4.29}$$

$$\frac{\partial \boldsymbol{B}}{\partial t} = -\boldsymbol{\nabla} \times \boldsymbol{E} - \zeta_\psi \boldsymbol{\nabla} \psi \tag{4.30}$$

$$\frac{\partial \psi}{\partial t} = -c^2 \zeta_\psi \boldsymbol{\nabla} \cdot \boldsymbol{B} \tag{4.31}$$

$$\frac{\partial \phi}{\partial t} = -\zeta_\phi \left(\boldsymbol{\nabla} \cdot \boldsymbol{E} - \frac{\rho_Q}{\epsilon_0} \right) \tag{4.32}$$

Equations (4.29) and (4.30) describe the temporal evolution of $\boldsymbol{E}$ and $\boldsymbol{B}$. Equations (4.31) and (4.32) are the evolution equations for the divergence proxies ψ and ϕ.

The parameters ζ_ϕ and ζ_ψ are the propagation speeds at which the divergence proxies remove errors in the divergence of the electric and magnetic field. In the limit as ζ_ϕ and ζ_ψ become infinitely large, the divergence constraints will be satisfied exactly, though this is not computationally feasible. For finite ζ_ϕ and ζ_ψ, the divergence constraints will be satisfied approximately. In Section 6.3, some tests of the PHM equations' divergence preserving capability are presented.

4.4   Non-dimensionalization of Governing Equations

For numerical convenience equations (2.19) – (2.21) and (4.29) – (4.31) are implemented in a non-dimensional form, similar to the approach of Abgrall and Kumar and Kumar and Mishra [3, 6].

$$\hat{\rho}_{i,e} \equiv \frac{\rho_{i,e}}{m_i n_0} \qquad (4.33)$$

$$\hat{E} \equiv \frac{E}{V_0 B_0} \qquad (4.37)$$

$$\hat{u}_{i,e} \equiv \frac{u_{i,e}}{V_0} \qquad (4.34)$$

$$\hat{B} \equiv \frac{B}{B_0} \qquad (4.38)$$

$$\hat{T}_{i,e} \equiv \frac{T_{i,e}}{T_0} \qquad (4.35)$$

$$\hat{\phi} \equiv \frac{\phi}{B_0} \qquad (4.39)$$

$$\hat{\varepsilon}_{i,e} \equiv \frac{\varepsilon_{i,e}}{m_i n_0 V_0^2} \qquad (4.36)$$

$$\hat{\psi} \equiv \frac{\psi}{V_0 B_0} \qquad (4.40)$$

This normalization strategy uses the ion reference thermal velocity as the reference velocity, $V_0 \equiv \sqrt{\frac{kT_0}{m_i}}$. The spatial scale is defined by $\hat{x} \equiv \frac{x}{x_0}$ and the temporal scale by $\hat{t} \equiv \frac{t}{t_0}$ where $t_0 \equiv \frac{x_0}{V_0}$. The mass ratio is defined as $M \equiv \frac{m_i}{m_e}$. Further, the normalized reference Larmor radius $\hat{r}_L$ and Debye length $\hat{\lambda}_D$ are defined as $\hat{r}_L \equiv \frac{V_0 m_i}{qB_0 X_0}$ and $\hat{\lambda}_D = \sqrt{\frac{\epsilon_0 kT_0}{n_0 q^2} \frac{1}{x_0}}$.

$$\frac{\partial \hat{\rho}_\alpha}{\partial \hat{t}} + \hat{\boldsymbol{\nabla}} \cdot \left[\hat{\boldsymbol{F}}_\alpha^{\hat{\rho}_\alpha} \right] = 0 \qquad (4.41)$$

$$\frac{\partial (\hat{\rho}_\alpha \hat{\boldsymbol{u}}_\alpha)}{\partial \hat{t}} + \hat{\boldsymbol{\nabla}} \cdot \left[\underline{\hat{\boldsymbol{F}}}_\alpha^{\hat{\rho}\hat{u}} \right] = \frac{M_\alpha}{\hat{r}_L} \left(\hat{\rho}_\alpha \hat{\boldsymbol{u}}_\alpha \times \hat{\boldsymbol{B}} + \hat{\rho}_\alpha \hat{\boldsymbol{E}} \right) + \hat{\boldsymbol{R}}_{\alpha\beta} \qquad (4.42)$$

$$\frac{\partial \hat{\varepsilon}_\alpha}{\partial \hat{t}} + \hat{\nabla} \cdot \left[\hat{\boldsymbol{F}}_\alpha^{\hat{\varepsilon}} \right] = \frac{M_\alpha}{\hat{r}_L} \hat{\rho}_\alpha \hat{\boldsymbol{u}}_\alpha \cdot \hat{\boldsymbol{E}} + \hat{\boldsymbol{u}}_\alpha \cdot \hat{\boldsymbol{R}}_{\alpha\beta} + \hat{Q}_{\alpha\beta}. \qquad (4.43)$$

$$\frac{\partial \hat{\boldsymbol{E}}}{\partial \hat{t}} = \hat{c}^2 \hat{\boldsymbol{\nabla}} \times \hat{\boldsymbol{B}} - \frac{\hat{r}_L}{\hat{\lambda}_D^2} \left(\hat{\boldsymbol{u}}_i - \hat{\boldsymbol{u}}_e \right) - \hat{c}^2 \zeta_\phi \hat{\boldsymbol{\nabla}} \hat{\phi} \qquad (4.44)$$

$$\frac{\partial \hat{\boldsymbol{B}}}{\partial \hat{t}} = -\hat{\boldsymbol{\nabla}} \times \boldsymbol{E} - \zeta_\psi \boldsymbol{\nabla} \psi \qquad (4.45)$$

$$\frac{\partial \hat{\psi}}{\partial \hat{t}} = -\hat{c}^2 \zeta_\psi \hat{\boldsymbol{\nabla}} \cdot \hat{\boldsymbol{B}} \qquad (4.46)$$

$$\frac{\partial \hat{\phi}}{\partial \hat{t}} = \zeta_\phi \left(\hat{\boldsymbol{\nabla}} \cdot \hat{\boldsymbol{E}} - \frac{\hat{r}_L}{\hat{\lambda}_D^2} \left(\hat{\rho}_i - M \hat{\rho}_e \right) \right) \qquad (4.47)$$

Applying these definitions to the governing equations, equations (2.19) – (2.21) and (4.29) – (4.31) become equations (4.41) – (4.46). The fluxes in equations (4.41) – (4.43) are given in normalized form in equations (4.48) – (4.50).

$$\hat{\boldsymbol{F}}_\alpha^{\hat{\rho}} \equiv \frac{\boldsymbol{F}_\alpha^{\rho_\alpha}}{m_i n_0 V_0}, \quad (4.48) \quad \underline{\hat{\boldsymbol{F}}}_\alpha^{\hat{\rho}\hat{\boldsymbol{u}}} \equiv \frac{\boldsymbol{F}_\alpha^{\rho\boldsymbol{u}}}{m_i n_0 V_0^2}, \quad (4.49) \quad \hat{\boldsymbol{F}}_\alpha^{\hat{\varepsilon}} \equiv \frac{\boldsymbol{F}_\alpha^\varepsilon}{m_i n_0 V_0^3}. \quad (4.50)$$

For simplicity of notation in the remainder of this dissertation, the "$\hat{\ }$" designation will be dropped for the variables in equations (4.41) – (4.47), and non-dimensionalized variables will be assumed unless stated otherwise.

4.5 PHM Flux Discretization and Source Terms

For the flux calculation in the PHM equations (4.44) – (4.47), a straightforward Lax-Friedrichs (LF) type flux calculation is used [49].

$$\tilde{F}_{i+\frac{1}{2}}^Q = \frac{1}{2} \left[F_{i+\frac{1}{2}}^{Q,L} + F_{i+\frac{1}{2}}^{Q,R} - \alpha \left(Q_{i+\frac{1}{2}}^r - Q_{i+\frac{1}{2}}^l \right) \right] \tag{4.51}$$

Equation (4.51) gives a basic overview of the LF flux calculation. In Equation (4.51), $F_{i+\frac{1}{2}}^{Q,L}$ and $F_{i+\frac{1}{2}}^{Q,R}$ are the left- and right- fluxes of the variable Q at the cell interface $i + \frac{1}{2}$ calculated from the left- and right-side reconstructed flow variables at that interface. The quantities $Q_{i+\frac{1}{2}}^{l,r}$ are the left- and right- values of the variable Q at the interface $i + \frac{1}{2}$.

The quantity α in equation (4.51) is generally taken to be the solution of the characteristic speed for the variable Q, but may alternatively be approximated as $\frac{\Delta x}{\Delta t}$. In applying this to the PHM equations, we have generally elected to simply set $\alpha = \hat{c}$. The LF flux is known to be only first-order [50], so to achieve second-order integration in time for the fluxes of equations (4.44) – (4.46), the LF flux is implemented within a two-stage Runge-Kutta scheme.

To calculate the source terms of equations (4.41) – (4.47), the code uses Strang Splitting. This is a form of operator splitting wherein first the source terms are advanced by $\frac{\Delta t}{2}$, then the fluxes are advanced by Δt followed by a second source term advancement of $\frac{\Delta t}{2}$.

$$\mathbb{L}^{\Delta t} \approx \mathbb{L}_1^{\Delta t/2} \mathbb{L}_2^{\Delta t} \mathbb{L}_1^{\Delta t/2} \tag{4.52}$$

If the total operator to solve equations (4.41) – (4.46) is represented by, e.g., $\mathbb{L}$, and the individual operators for the source term update and flux update are $\mathbb{L}_1$ and $\mathbb{L}_2$, respectively, then equation (4.52) represents the approximate total update over a time-step Δt, which is accurate to second order [51]. Thus, the integration scheme of equations (4.44) – (4.46) should be second-order overall.

5. PRELIMINARY LINEAR ANALYSIS

To benchmark the performance of the implemented two-fluid plasma gas-kinetic scheme the numerical solution will be compared to an analytical solution of the linearized governing equations. Seeking solutions in the linear regime allows us to obtain exact analytic solutions against which to compare. A similar procedure was followed by Loverich et al. to benchmark their Discontinuous Galerkin method for solving the ideal two-fluid equations [5].

5.1 Linearization of Governing Equations

To obtain an analytic solution to equations 4.41-4.47, a small perturbation to the electron velocity is assumed, with spatial and temporal dependence $e^{i(kx+\omega t)}$. The ions are assumed to be stationary in this derivation. Further, $\hat{\boldsymbol{F}}_\alpha^{\hat{\rho}}$, $\hat{\underline{\boldsymbol{F}}}_\alpha^{\hat{\rho}\hat{\boldsymbol{u}}}$, $\hat{\boldsymbol{F}}_\alpha^{\hat{\epsilon}}$ are assumed to take their ideal (i.e. Euler) form.

$$\frac{\partial \hat{\rho}_e}{\partial \hat{t}} + \hat{\boldsymbol{\nabla}} \cdot [\hat{\rho}_e \hat{\boldsymbol{u}}_e] = 0 \tag{5.1}$$

$$\frac{\partial (\hat{\rho}_e \hat{\boldsymbol{u}}_e)}{\partial \hat{t}} + \hat{\boldsymbol{\nabla}} \cdot [\hat{\rho}_e \hat{\boldsymbol{u}}_e \hat{\boldsymbol{u}}_e + \underline{\boldsymbol{1}} \hat{p}_e] = \frac{M}{\hat{r}_L} \left(\hat{\rho}_e \hat{\boldsymbol{u}}_e \times \hat{\boldsymbol{B}} + \hat{\rho}_e \hat{\boldsymbol{E}} \right) + \hat{\boldsymbol{R}}_{e\beta} \tag{5.2}$$

$$\frac{\partial \hat{\epsilon}_e}{\partial \hat{t}} + \hat{\nabla} \cdot [\hat{\boldsymbol{u}}_e \hat{\varepsilon}_e + \hat{\boldsymbol{u}}_e \hat{p}_e] = \frac{M}{\hat{r}_L} \hat{\rho}_e \hat{\boldsymbol{u}}_e \cdot \hat{\boldsymbol{E}} + \hat{\boldsymbol{u}}_e \cdot \hat{\boldsymbol{R}}_{e\beta} + \hat{Q}_{e\beta}. \tag{5.3}$$

$$\frac{\partial \hat{\boldsymbol{E}}}{\partial \hat{t}} = \hat{c}^2 \hat{\boldsymbol{\nabla}} \times \hat{\boldsymbol{B}} - \frac{\hat{r}_L}{\hat{\lambda}_D^2} (\hat{\boldsymbol{u}}_i - \hat{\boldsymbol{u}}_e) \tag{5.4}$$

$$\frac{\partial \hat{\boldsymbol{B}}}{\partial \hat{t}} = -\hat{\boldsymbol{\nabla}} \times \boldsymbol{E} \tag{5.5}$$

$$\tag{5.6}$$

Here we have returned to the regular (non-PHM) form of Maxwell's equations for equations (5.4) – (5.5). Assuming variation only along x (i.e. $\frac{\partial}{\partial y} = \frac{\partial}{\partial z} = 0$), we can reduce equations

(5.1) – (5.5) to the following:

$$\frac{\partial \rho_e}{\partial t} + \frac{\partial}{\partial x}\left(\rho_e u_e\right) = 0 \tag{5.7}$$

$$\rho_e \frac{\partial u_e}{\partial t} + \rho_e u_e \frac{\partial u_e}{\partial x} + \frac{\partial p_e}{\partial x} = -\frac{M}{r_L}\left(\rho_e v_e B_z + \rho_e E_x\right) - \frac{\rho_e^2 M^2 u_e}{\sigma \lambda_D^2 c^2} \tag{5.8}$$

$$\rho_e \frac{\partial v_e}{\partial t} + \rho_e u_e \frac{\partial v_e}{\partial x} = -\frac{M}{r_L}\left(-\rho_e u_e B_z + \rho_e E_y\right) - \frac{\rho_e^2 M^2 v_e}{\sigma \lambda_D^2 c^2} \tag{5.9}$$

$$\frac{\partial T_e}{\partial t} + u_e \frac{\partial T_e}{\partial x} + \frac{2}{3}T_e \frac{\partial u_e}{\partial x} = 0 \tag{5.10}$$

$$\frac{\partial E_x}{\partial t} = -\frac{r_L}{\lambda_D^2}\left(-M\rho_e u_e\right) \tag{5.11}$$

$$\frac{\partial E_y}{\partial t} = -c^2 \frac{\partial B_z}{\partial x} - \frac{r_L}{\lambda_D^2}\left(-M\rho_e v_e\right) \tag{5.12}$$

$$\frac{\partial B_z}{\partial t} = -\frac{\partial E_y}{\partial x} \tag{5.13}$$

In equations (5.7)–(5.13) and the following analysis we have removed the hat notation ($\hat{\cdot}$) denoting normalized variables for simplicity. First we will assume a perturbed solution for the electron x-velocity $u_e = -iU_0 \exp[i(kx + \omega t)]$, where $U_0 \ll 1$. The ions are assumed to be infinitely massive and stationary ($\rho_i = const = \rho_0$, $\boldsymbol{u}_i = 0 = const$, $T_i = T_{e,0} = const$). Additionally, we assume that $w_e = 0$, $E_z = 0$, and $B_y = B_x = 0$. Further we assume that $\frac{\omega}{k} \ll c$, i.e. that the plasma is non-relativistic.

$$\rho_e = \rho_{e,0}\left[1 + \frac{ikU_0}{\omega}\exp(i(kx + \omega t))\right] \tag{5.14}$$

$$T_e = T_{e,0}\left[1 + \frac{2}{3}i\frac{ku_0}{\omega}\exp(i(kx + \omega t))\right] \tag{5.15}$$

From the electron mass conservation (5.7) and energy conservation (5.10), and the assumed solution for u_e it is straightforward to obtain an expression for the perturbed density ρ_e – equation (5.14) – and perturbed temperature T_e – equation (5.15). In equation (5.15) the $\frac{2}{3} = (\gamma_e - 1)$ is for $\gamma_e = \frac{5}{3}$.

From equation (5.11) and using the perturbed solutions for ρ_e and u_e we can obtain the

solution for the x-component of the electric field E_x.

$$E_x = -\frac{U_0 M \rho_{e,0} r_L}{\omega \lambda_D^2} \exp[i(kx + \omega t)] \qquad (5.16)$$

If we further assume that $B_z = E_y = v_e = 0$, then from equation (5.8) we can obtain the dispersion relation for ω, equation (5.17).

$$\omega \approx \pm \left[\frac{5}{3} M T_{e,0} k^2 + \frac{M^2 \rho_{e,0}}{\lambda_D^2} \right]^{\frac{1}{2}} + i \frac{M^2 \rho_{e,0}}{2\sigma \lambda_D^2 c^2} \qquad (5.17)$$

This assumes $\frac{5}{3} M T_{e,0} k^2, \frac{M^2 \rho_{e,0}}{\lambda_D^2} \gg \left(\frac{M^2 \rho_{e,0}}{2\sigma \lambda_D^2 c^2} \right)^2$, i.e. that $v_{th}^2 k^2, \omega_p^2 \gg \frac{1}{4\tau_{ei}^2}$. Essentially that the characteristic damping time is appreciably longer than a period of the oscillations. The imaginary portion of ω being positive – $\Im(\omega) > 0$ – indicates an exponential decay of the oscillations, with characteristic time of $\frac{2\sigma \lambda_D^2 c^2}{M^2 \rho_{e,0}} = 2\tau_{ei}$.

If we assume $\sigma \to \infty$ (i.e. $\tau_{ei} \to \infty$), there will be no damping in the solution. If we further assume that $B_z \neq 0$ we must also allow $E_y \neq= 0$ and $v_e \neq 0$. From this we will obtain solutions for v_e, E_y, and B_z, and a modified dispersion relation for ω:

$$v_e = -\frac{B_{z,0} M U_0}{\omega r_L} \exp[i(kx + \omega t)], \qquad (5.18)$$

$$E_y = -i\frac{B_{z,0} M^2 \rho_{e,0} U_0}{c^2 k^2 \lambda_D^2} \exp[i(kx + \omega t)], \qquad (5.19)$$

$$B_z = B_{z,0} \left(1 + i\frac{M^2 \rho_{e,0} U_0}{\omega k c^2 \lambda_D^2} \exp[i(kx + \omega t)] \right). \qquad (5.20)$$

From equation (5.9), (5.12), and (5.13) we can obtain equations (5.18) – (5.20) for v_e, E_y, and B_z. Once again from equation (5.8) we obtain the dispersion relation for ω:

$$\omega \approx \pm \left[\frac{5}{3} M T_{e,0} k^2 + \frac{M^2 \rho_{e,0}}{\lambda_D^2} + \frac{B_{z,0}^2 M^2}{r_L^2} \right]^{\frac{1}{2}}. \qquad (5.21)$$

These assume $\omega^2 \ll c^2 k^2$, $\omega_p^2 \ll c^2 k^2$.

51

5.2 Results of Linear Analysis

In the following, two cases will be examine. The first is initialized with a single wave mode – $u_e = -iU_0 \exp[i(kx + \omega t)]$ – in order to verify that the solver captures the simplest version of the solution. In the second, an approximate square wave for the electron velocity u_e is used by initializing a linear combination of wave modes.
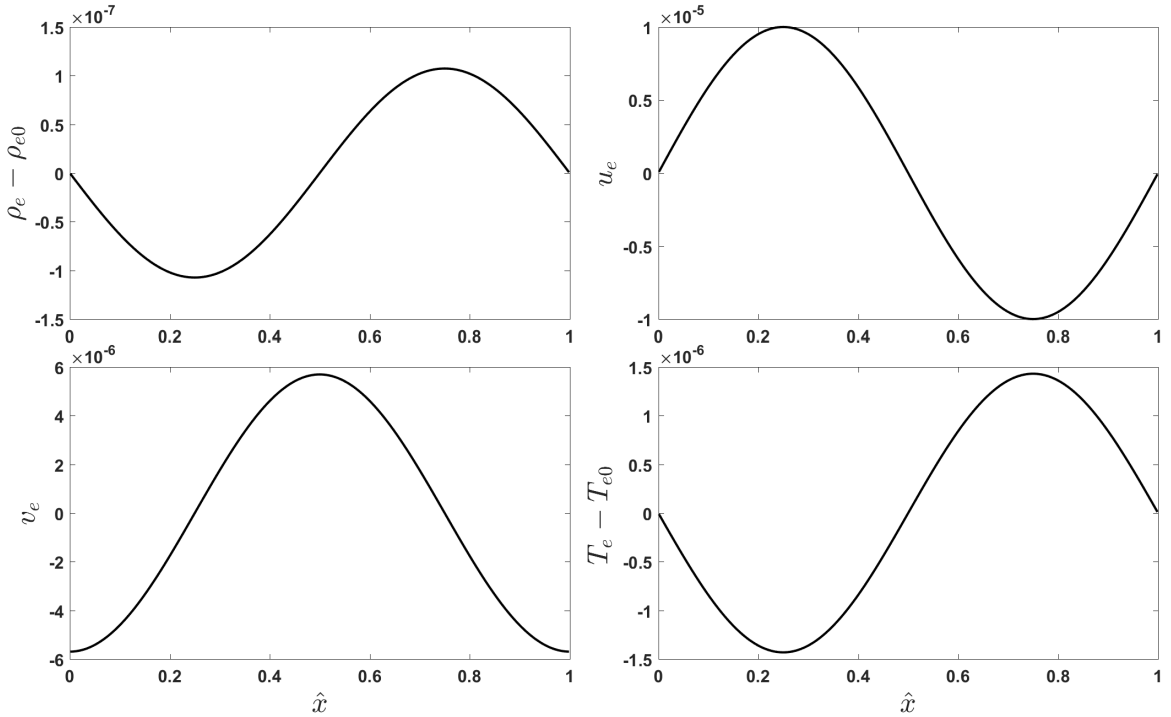

Figure 5.1: Initial condition of electron x- and y-velocity, temperature, and density for linearized solution using a single mode. T and ρ are plotted as $T_e - T_{e,0}$ and $\rho_e - \rho_{e,0}$

For the single wave mode the initialization of the electron fluid variables ρ_e, T_e, u_e, and v_e are depicted in Figure 5.1 while the electromagnetic fields E_x, E_y and B_z are shown in Figure 5.2. A second set of initial conditions uses an approximate square wave – Eq. (5.22) – which initializes several modes at once to further test the scheme's performance.

$$u_e = \sum_{n=0}^{9} -i\frac{U_0}{2n+1} \exp[i(k_n x + \omega_n t)] \tag{5.22}$$

52

Figure 5.2: Initial condition of x- and y-components of the electric field and z-component of the magnetic field for linearized solution using a single mode. B_z is plotted as $B_z - B_{z,0}$

This approach is similar to that of Loverich et al. [5]. The approximate wave pulse with 10 modes seen in equation (5.22) is used because it would be impossible to resolve all of the modes of the square pulse on a finite grid.
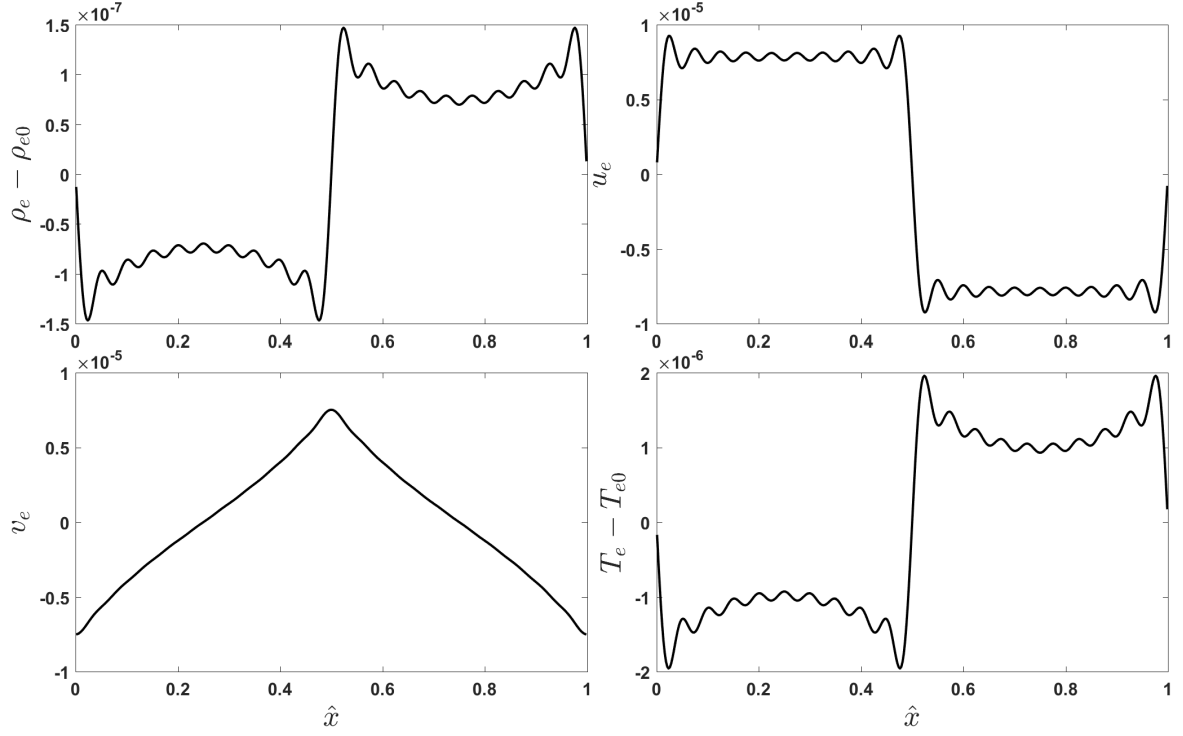
Figure 5.3: Initial condition of electron x- and y-velocity, temperature, and density for linearized solution using an approximate square wave for the electron x-velocity. T, and ρ are plotted as $T_e - T_{e,0}$ and $\rho_e - \rho_{e,0}$

Figures 5.3 and 5.4 show the initialization of the approximate square mode in the electron x-velocity. Note that the wave is not square for the temperature, density, y-velocity, and the electromagnetic fields. In the following results, unless otherwise specified a grid of $Nx = 400$ cells – i.e. $\Delta x = 0.0025$ with $\Delta t = 5 \times 10^{-7}$ is used.
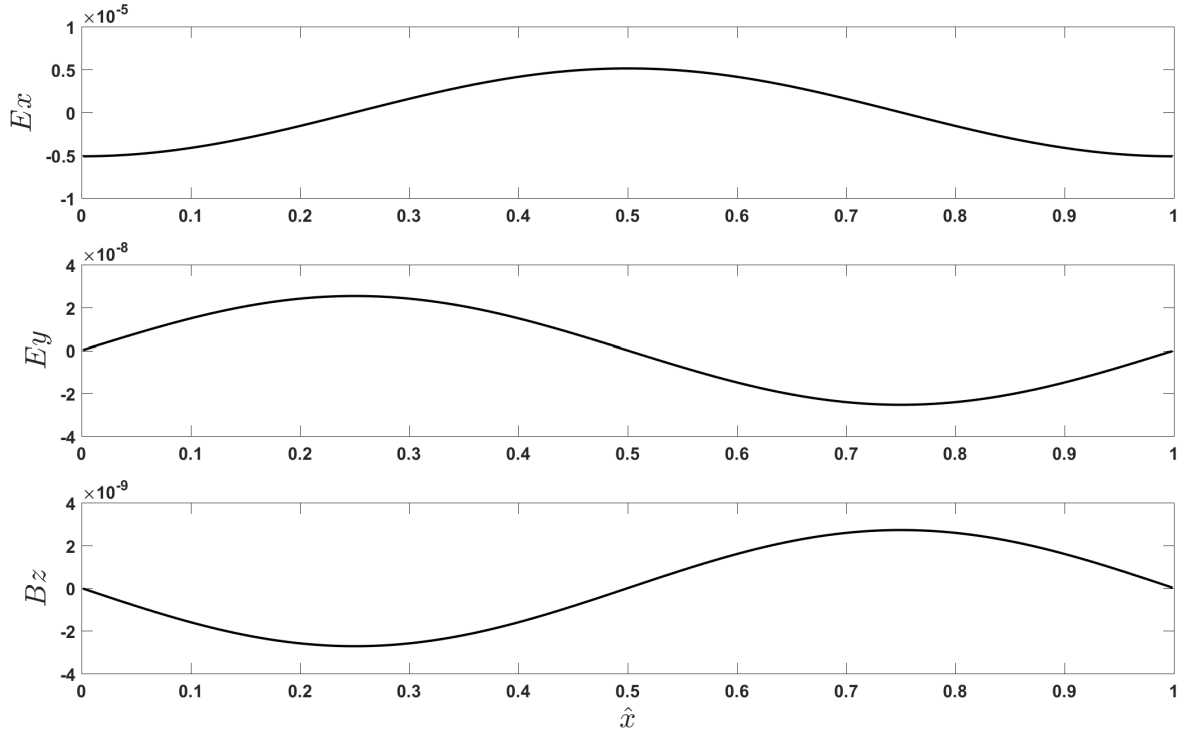
Figure 5.4: Initial condition of x- and y-component of the electric field and z-component of the magnetic field for linearized solution using an approximate square wave for the electron x-velocity. B_z is plotted as $B_z - B_{z,0}$
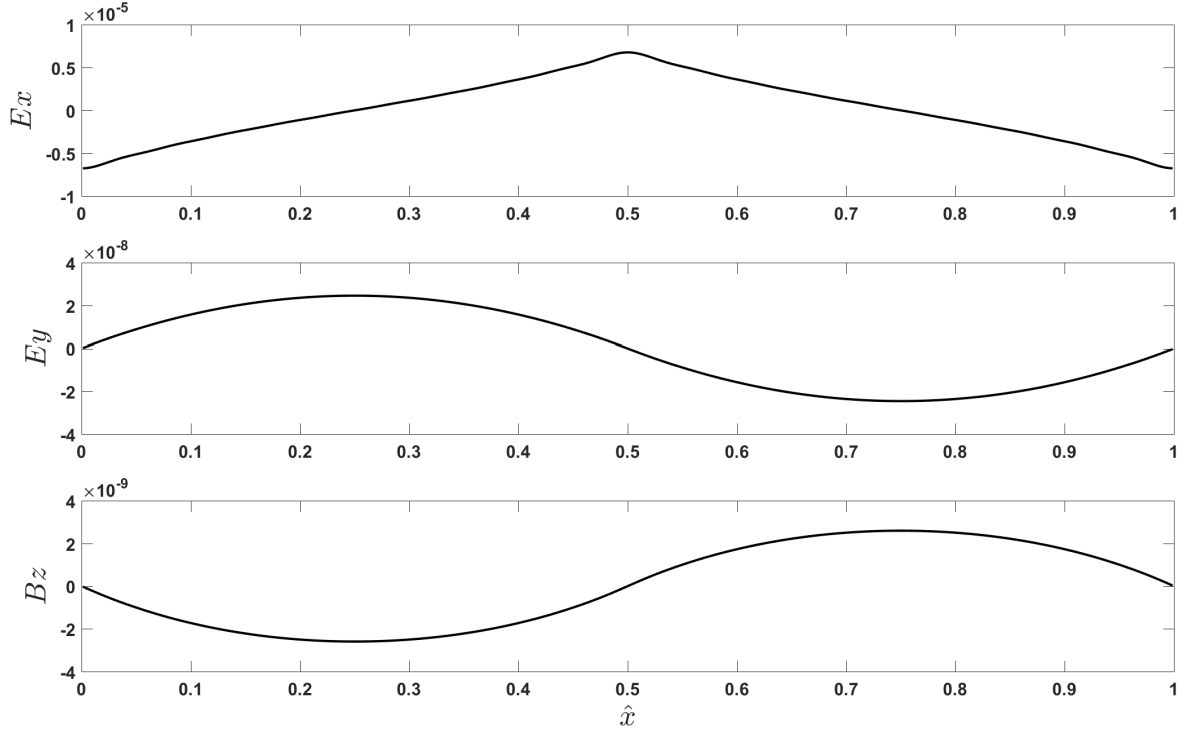
5.2.1 PHM Solver Benchmark: Constrained Electron Fluid

The Perfectly Hyperbolic Maxwell's equations are used to evolve the electromagnetic fields in such a way that the divergence constraints of Gauss' law for the electric and magnetic fields are enforced. As the current implementation is only one-dimensional, this is strictly speaking not necessary for the magnetic field as it is trivially enforced – if $\nabla \cdot \boldsymbol{B} = 0$ is true in the initial conditions it cannot evolve to be otherwise. In addition, while it is possible that charge conservation violations may occur in a one-dimensional simulation we expect that it is likely not critical. Here we test the PHM solver in isolation by driving or constraining the electron fluid properties to follow the analytic linearized solutions exactly.

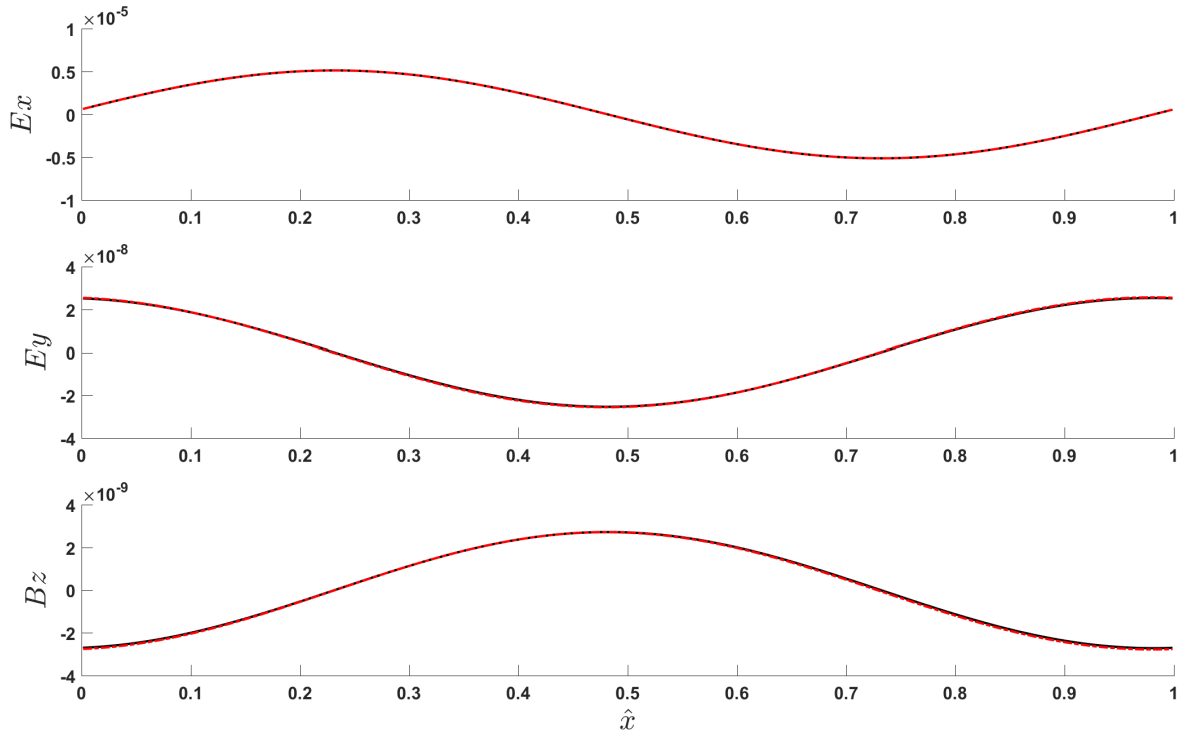Figure 5.5: Electromagnetic fields at $\hat{t} = 4$. Analytic solution (solid black) vs. the computed solution (dashed red) for the driven electron fluid case for a single mode

Figure 5.5 compares the computed solution of the electromagnetic fields to the analytic solution from equations (5.16), (5.19), and (5.20) in the spatial domain at a non-dimensional time $\hat{t} = 4$ for a single wave.

Figure 5.6: Electromagnetic fields at $\hat{x} = 0.25$ for $\hat{t} = 0 - 4$. Analytic solution (solid black) vs. the computed solution (dashed red) for the driven electron fluid case for a single mode

Figure 5.6 compares the analytic and numerical solutions at a single point ($\hat{x} = 0.25$) over the entire simulation time. In both cases it can be seen that the agreement is very good. This is further demonstrated by Figure 5.7 which depicts the normalized L_1 error of each of the electric and magnetic field components. The L_1 norm of a quantity y is defined as $L_1 \equiv \sum_{i=1}^{N} |y_i|$, where the summation over $i \in [1, N]$ is done for all cells in the domain. The L_1 error here has y equal to the difference between the computed and analytical solutions at each point. In all three the error is constant and does not appear to grow significantly in time. Later in Section 6.3 we perform further verification of the PHM solver against published data for the electromagnetic shock problem [52].

Figure 5.7: Base-10 logarithm of the normalized L_1 error for electromagnetic fields for $\hat{t} = 0 - 4$ for the driven electron fluid case for a single mode

In addition to the single wave mode, multi-mode simulations were run for the approximate u_e square pulse initialization with the electron fluid variables prescribed to follow their exact analytic solutions.

Figure 5.8: Electromagnetic fields at $\hat{t} = 4$. Analytic solution (solid black) vs. the computed solution (dashed red) for the driven electron fluid case – approximate square wave

Figure 5.8 compares the computed solution of the electromagnetic fields to the analytic solution from equations (5.16), (5.19), and (5.20) in the spatial domain at a non-dimensional time $\hat{t} = 4$.
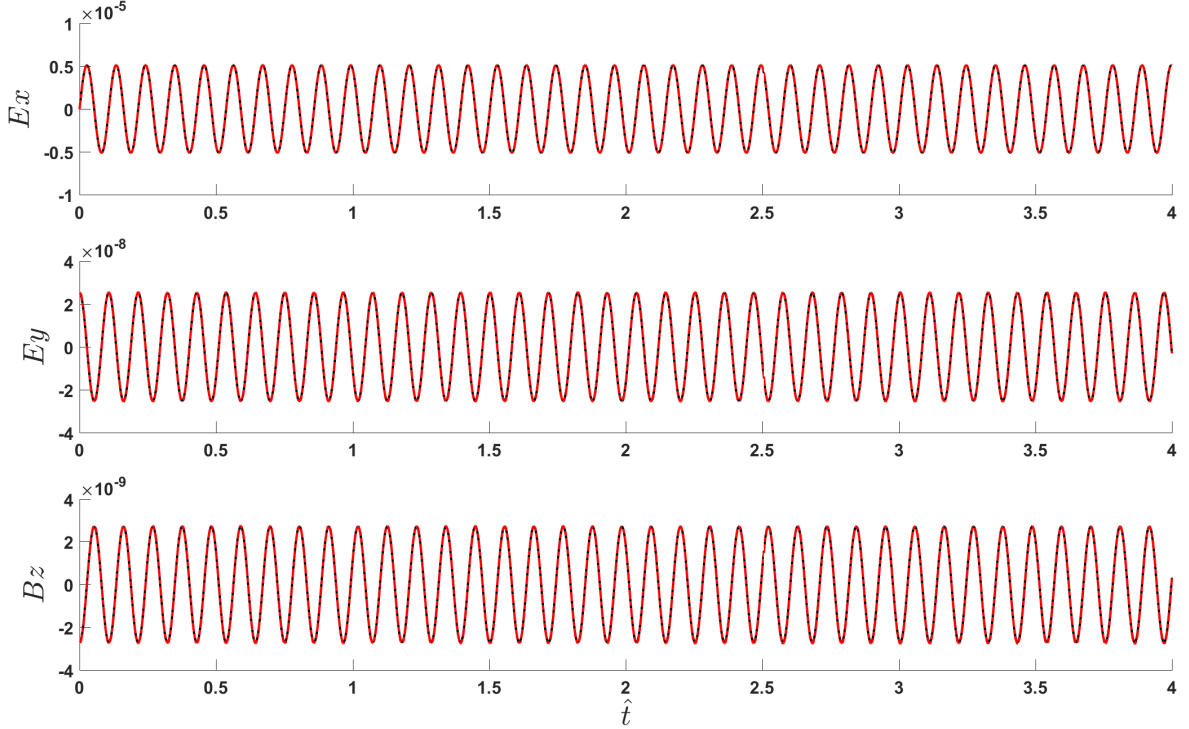
Figure 5.9: Electromagnetic fields at $\hat{x} = 0.25$ for $\hat{t} = 0 - 4$. Analytic solution (solid black) vs. the computed solution (dashed red) for the driven electron fluid case – approximate square wave

Figure 5.9 compares the analytic and numerical solutions at a single point ($\hat{x} = 0.25$) over the entire simulation time. In both cases it can be seen that the agreement is very good. This is further demonstrated by Figure 5.10 which depicts the normalized L_1 error of each of the electric and magnetic field components. In all three the error is constant and does not appear to grow significantly in time.
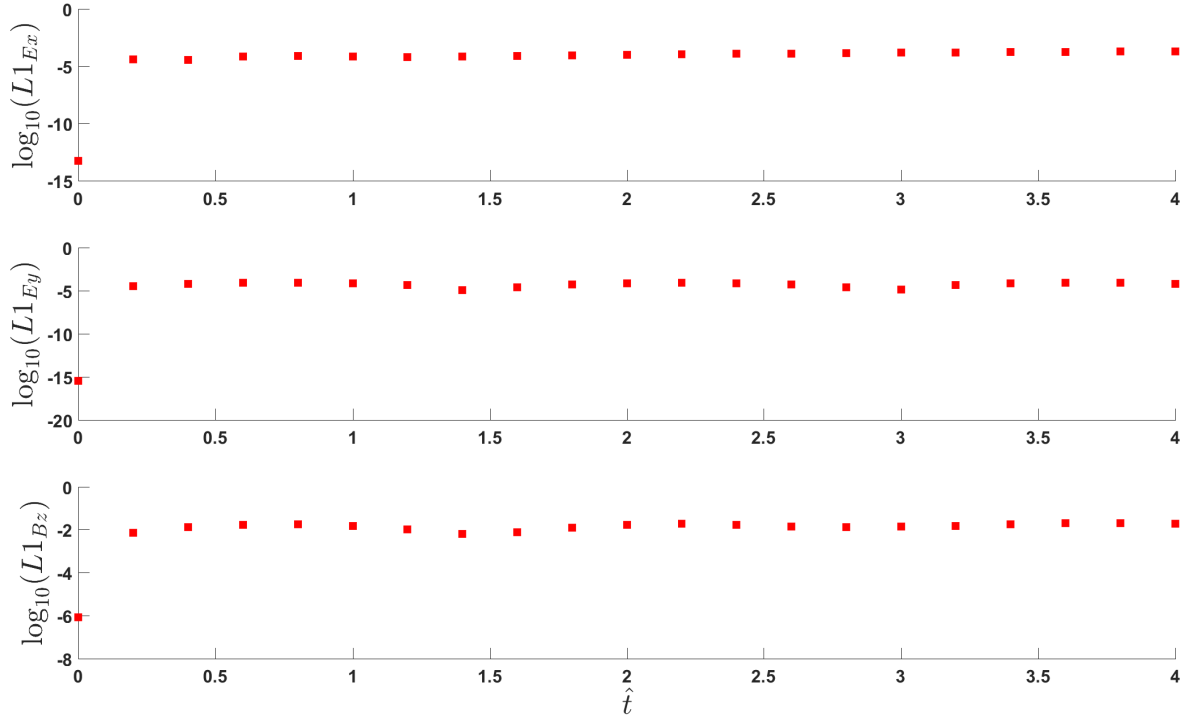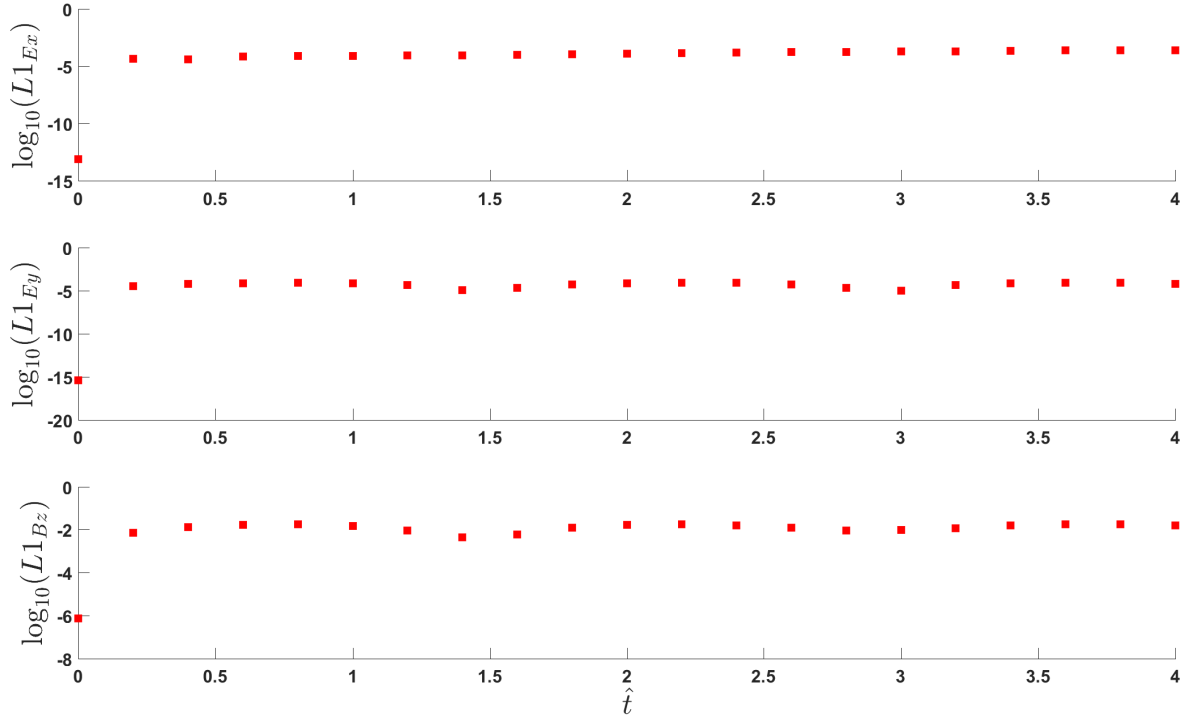
Figure 5.10: Base-10 logarithm of the normalized L_1 error for electromagnetic fields for $\hat{t} = 0 - 4$ for the driven electron fluid case – approximate square wave

5.2.2 Full System Evolution

Next the full system is tested allowing it to evolve from the given initial state, and compared to the analytical solution. Figures 5.11 and 5.12 compare the spatial solution of the electron fluid quantities ρ_e, u_e, v_e, and T_e, and the electromagnetic fields E_x, E_y, and B_z at non-dimensional time $\hat{t} = 4$ for a single wave mode.
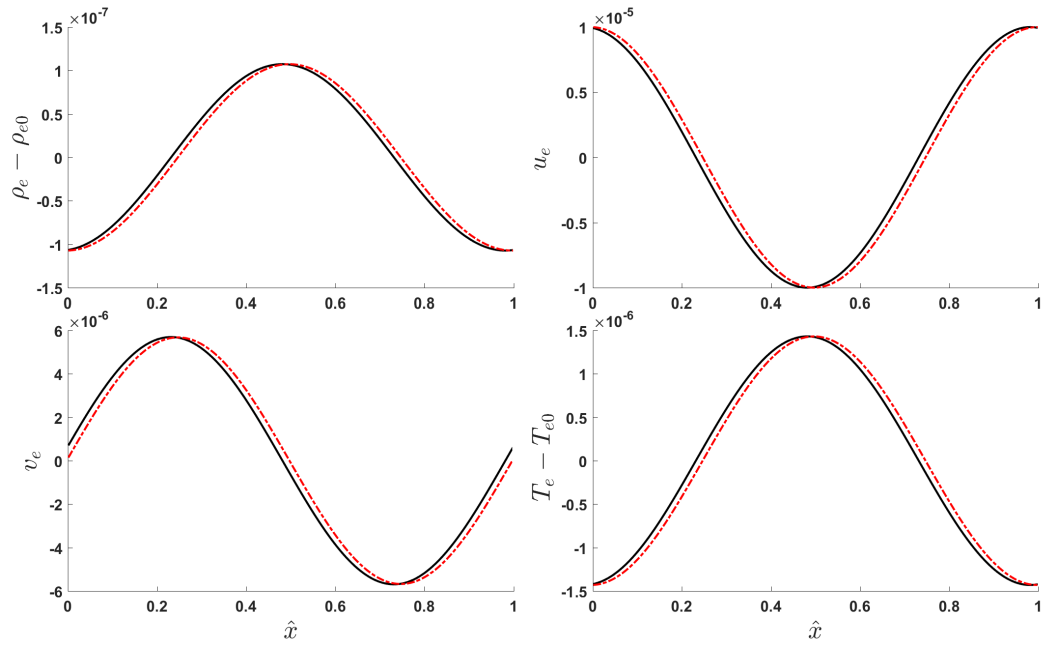
Figure 5.11: Electron fluid variables at $\hat{t} = 4$. Analytic solution (solid black) vs. the computed solution (dashed red) for a single mode
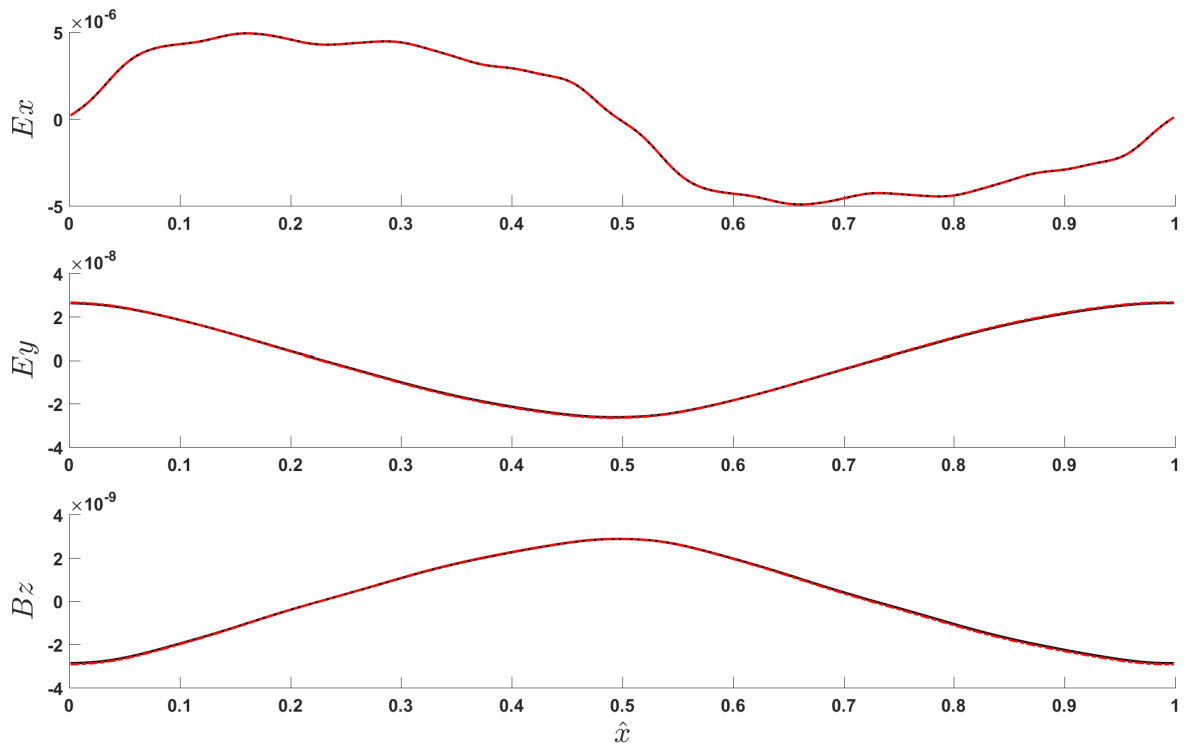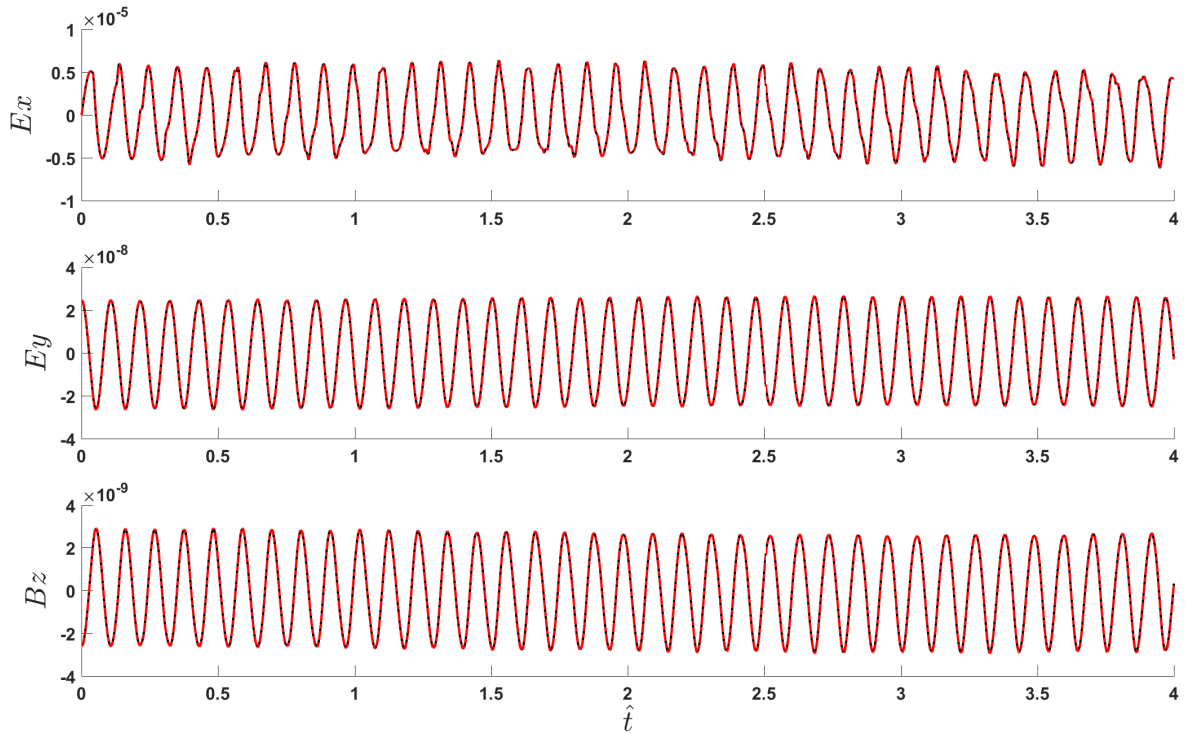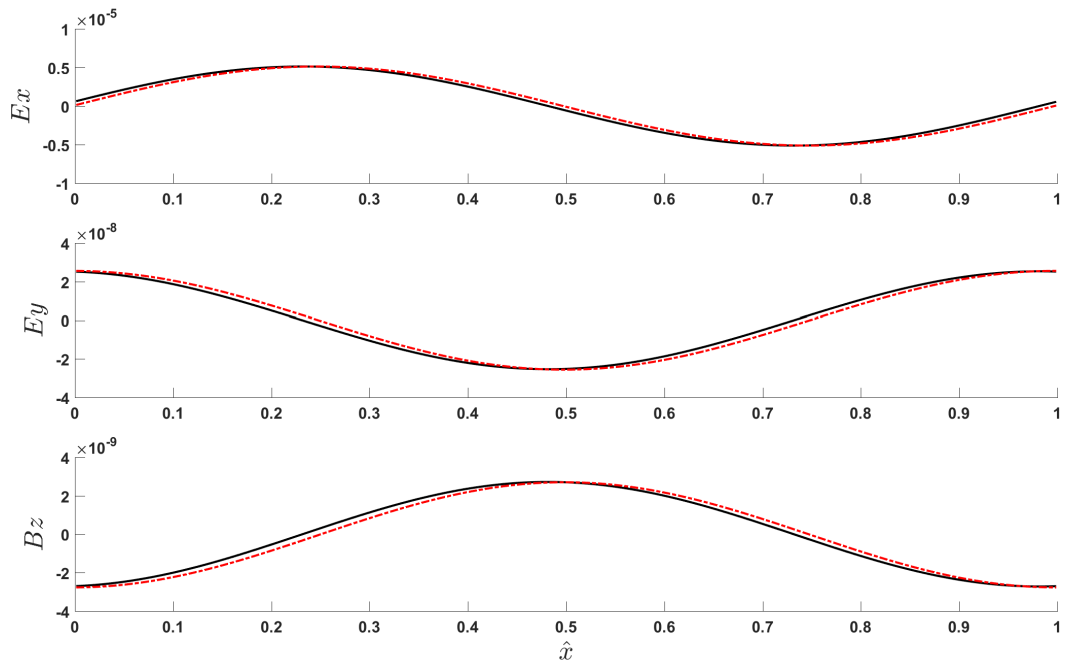

Figure 5.12: Electromagnetic fields at $\hat{t} = 4$. Analytic solution (solid black) vs. the computed solution (dashed red) for a single mode

In all cases the computed solutions are very close to the analytical solution, with only a slight drift in phase. Figures 5.13 and 5.14 compare the numerical and analytic solutions in

Figure 5.13: Electron fluid variables at $\hat{x} = 0.25$ for $\hat{t} = 0 - 4$. Analytic solution (solid black) vs. the computed solution (dashed red) for a single mode

time for the electron fluid and electromagnetic fields at $\hat{x} = 0.25$. While Figures 5.13 and 5.14 may appear to not have any drift error like that seen in Figures 5.11 and 5.12, we can see in Figures 5.15 and 5.16 as we zoom to the first and last periods of oscillation for the electron fluid properties and electromagnetic fields – $\hat{t} = 0 - 0.1075$ and $\hat{t} = 3.8925 - 4.0$, respectively – that there is indeed a similar phase error in the temporal oscillation at $\hat{x} = 0.25$, which grows over time from $\hat{t} = 0$ to $\hat{t} = 4.0$. The observed phase drift may come from either the underlying nonlinearity of the governing equations, or due to accumulated errors in integration. To examine this, two additional coarser grids were used – $Nx = 200$ and $Nx = 100$ – with proportionally larger Δt. The results can be seen in Figure 5.17, which clearly shows that the drift error is equal for all grids. A zoomed inset for the electron

Figure 5.14: Electromagnetic fields at $\hat{x} = 0.25$ for $\hat{t} = 0 - 4$. Analytic solution (solid black) vs. the computed solution (dashed red) for a single mode
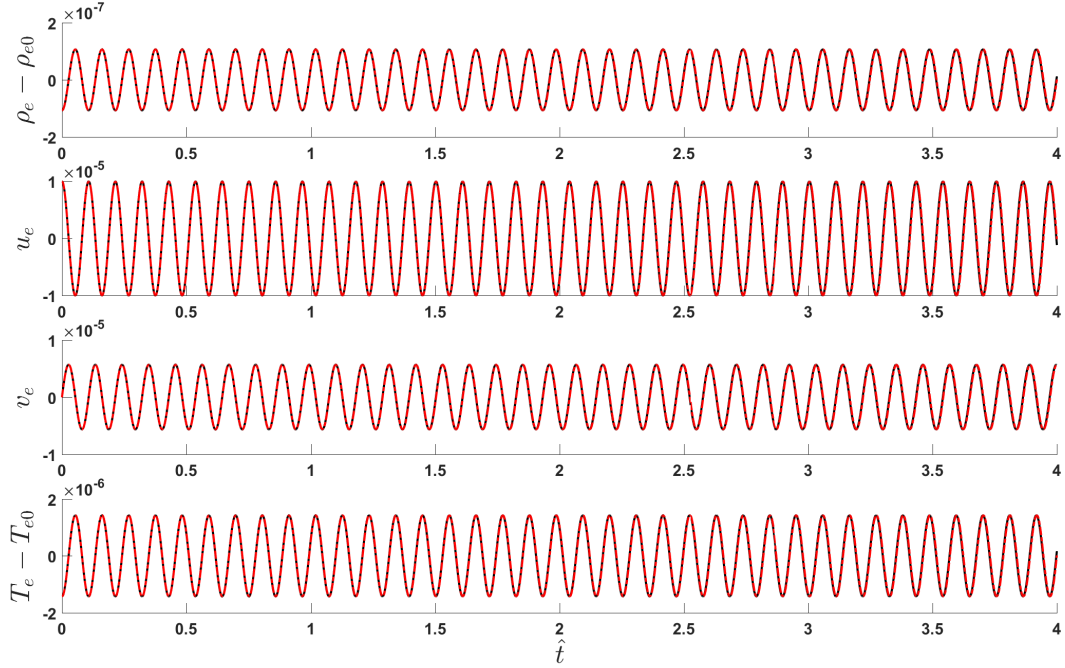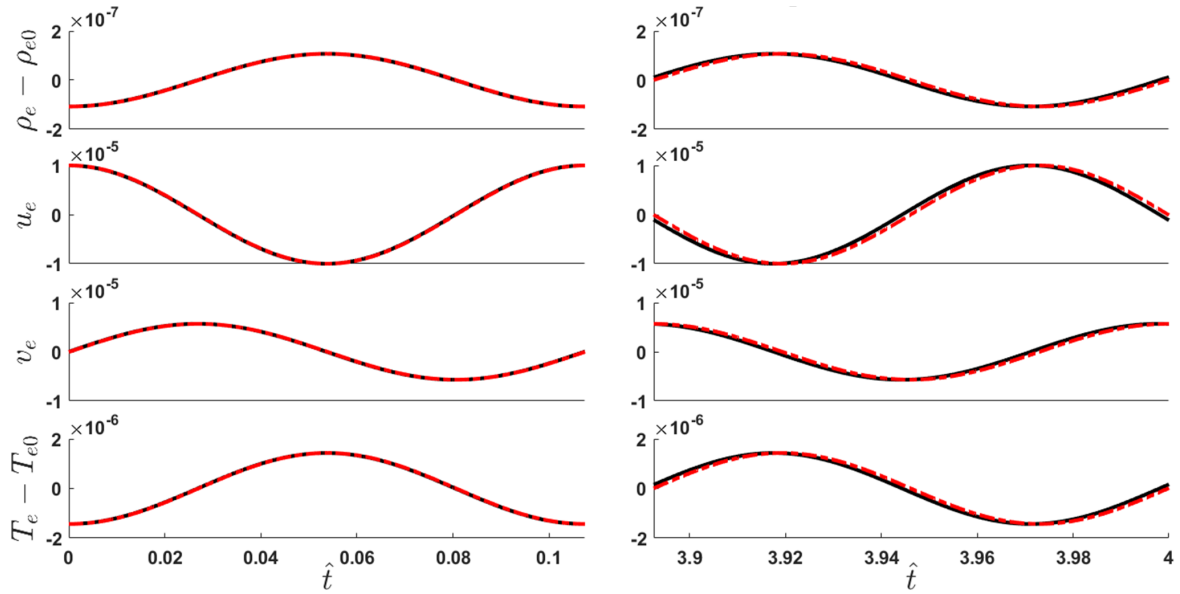

Figure 5.15: Electromagnetic fields at $\hat{x} = 0.25$ for $\hat{t} = 0 - 0.1075$ and $\hat{t} = 3.8925 - 4.0$. Analytic solution (solid black) vs. the computed solution (dashed red) for a single mode

64

Figure 5.16: Electron fluid variables at $\hat{x} = 0.25$ for $\hat{t} = 0 - 0.1075$ and $\hat{t} = 3.8925 - 4.0$. Analytic solution (solid black) vs. the computed solution (dashed red) for a single mode

Figure 5.17: Electron fluid variables at $\hat{t} = 4$ comparing grids for $Nx = [100, 200, 400]$ in space for the single mode

density ρ_e shows the peak of the wave, where the lowest resolution case ($Nx = 100$) can be clearly seen to be more dissipative due to the increased numerical diffusion. We thus

conclude that the drift error is a consequence of the solution for the full nonlinear governing equations being compared to the analytic solutions for the linearized system, particularly given the relatively long simulation time of ~ 40 periods. The normalized L_1 error for the

Figure 5.18: Base-10 logarithm of the normalized L_1 error for electron fluid variables for $\hat{t} = 0 - 4$ for a single mode

fluid variables in time is depicted in Figure 5.18 and Figure 5.19 shows the L_1 error for the electromagnetic fields. The error in the EM fields appears very steady after an initial jump, while the fluid quantities exhibit a slow increase in error relative to the analytic solution over time. It is most likely that this is due to growing nonlinearities. Recall that while the analytic solution is linear, the governing equations are not.
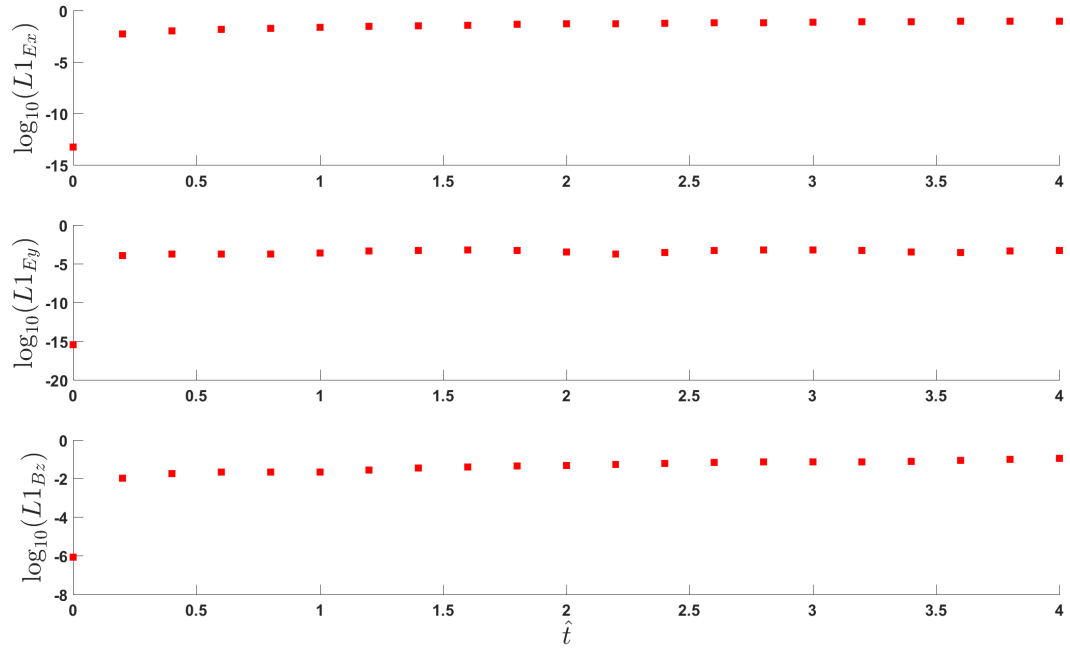
Figure 5.19: Base-10 logarithm of the normalized L_1 error for electromagnetic fields for $\hat{t} = 0 - 4$ for a single mode

Next the full system with multiple wave modes is studied. Figures 5.20 and 5.21 compare the spatial solution of the electron fluid quantities ρ_e, u_e, v_e, and T_e, and the electromagnetic fields E_x, E_y, and B_z at non-dimensional time $\hat{t} = 4$.
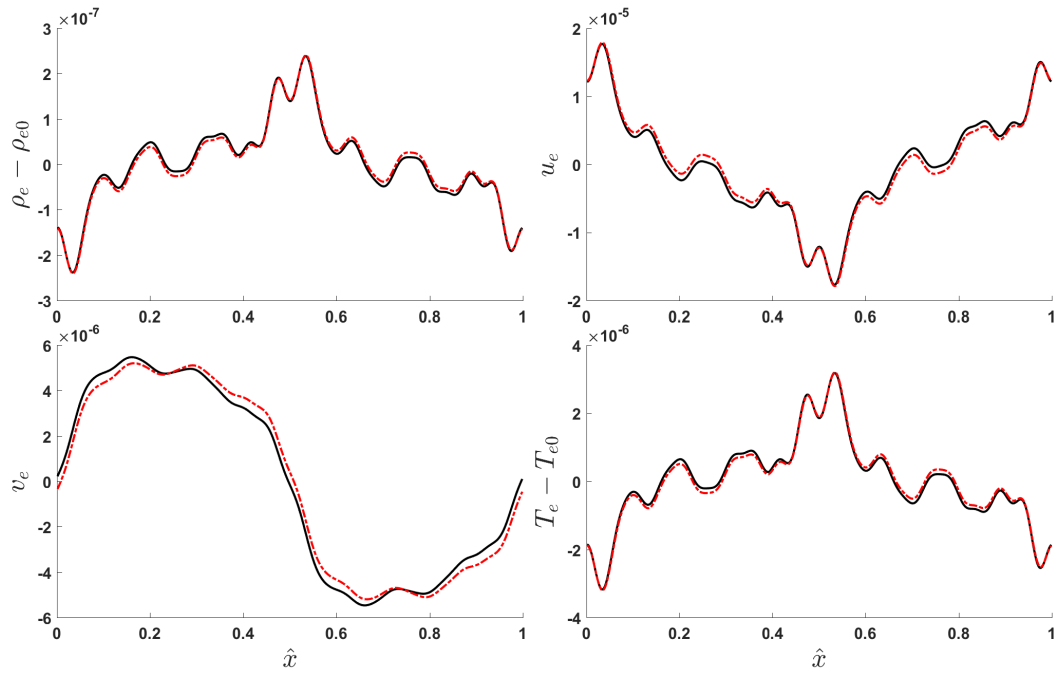
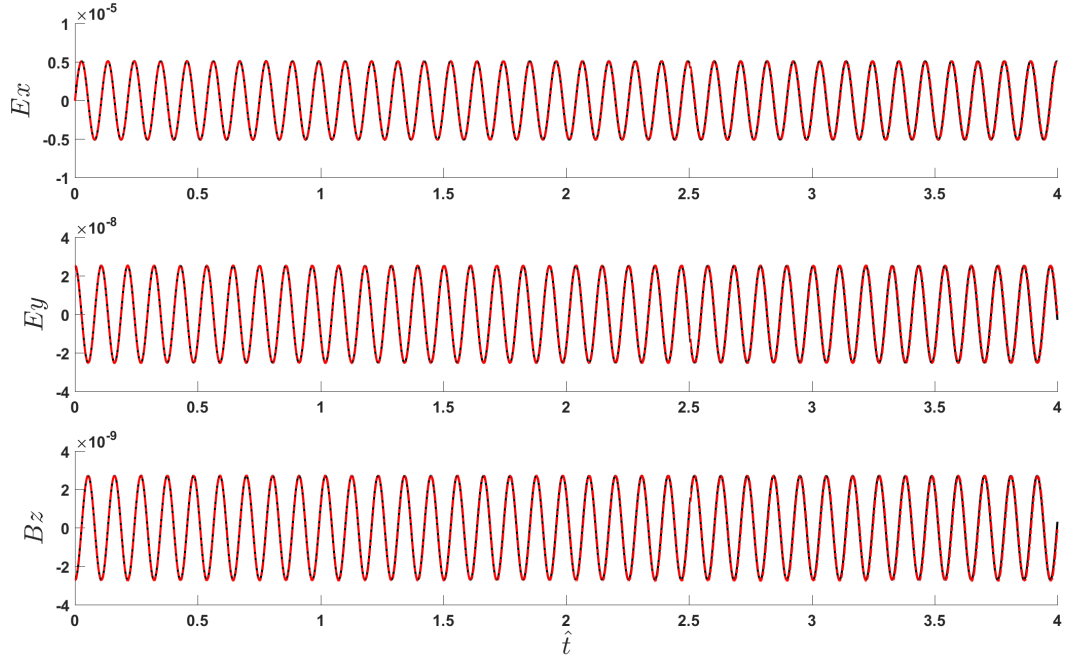Figure 5.20: Electron fluid variables at $\hat{t} = 4$. Analytic solution (solid black) vs. the computed solution (dashed red) – approximate square wave
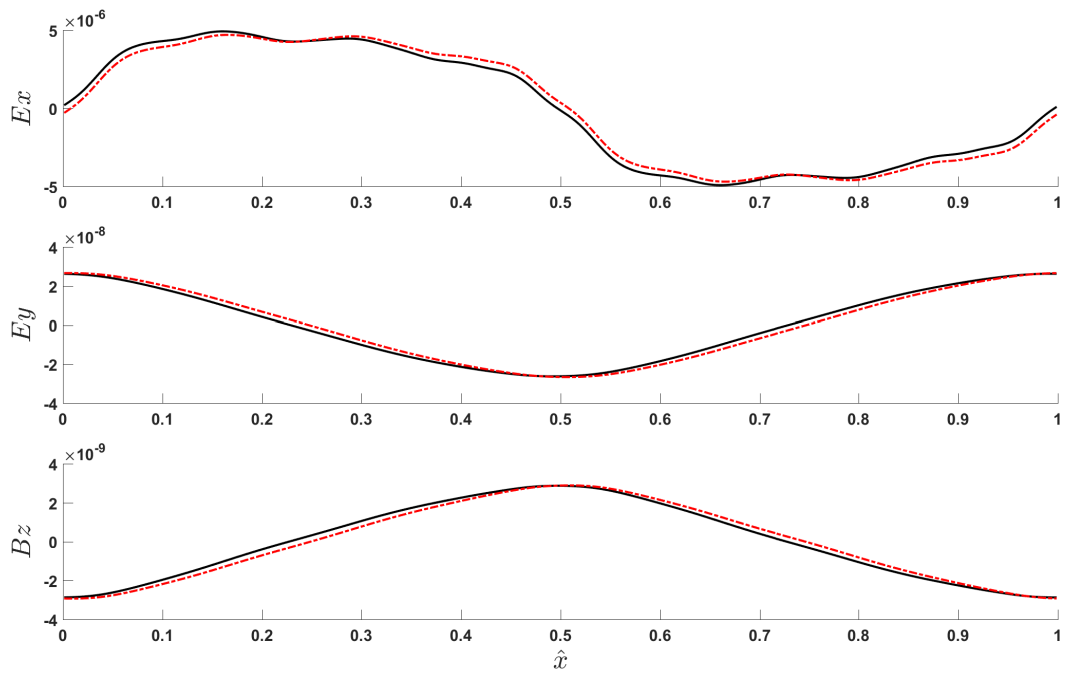
Figure 5.21: Electromagnetic fields at $\hat{t} = 4$. Analytic solution (solid black) vs. the computed solution (dashed red) – approximate square wave

In both cases the computed solutions are very close to the analytical solution, with once again only a slight drift in phase. Figure 5.22 once again depicts a comparison to the $Nx = 200$
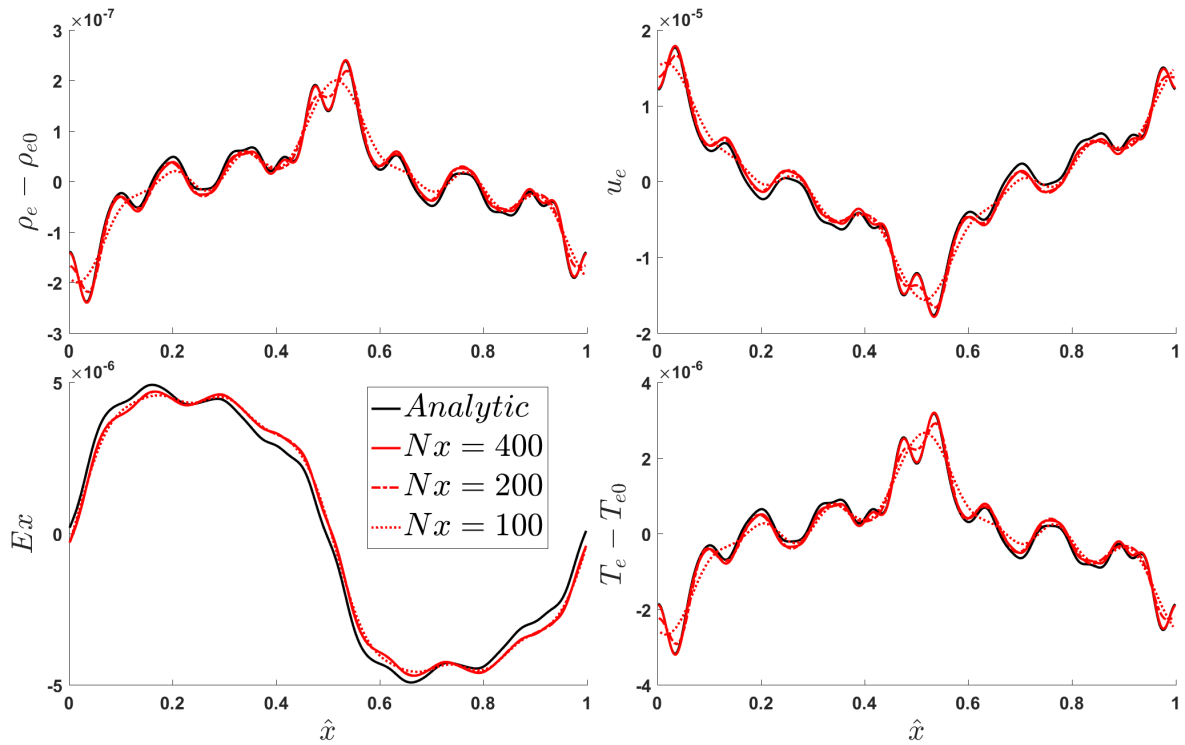
Figure 5.22: Electron fluid variables at $\hat{t} = 4$ comparing grids for $Nx = [100, 200, 400]$ in space for the approximate square wave

and $Nx = 100$ grids, where it can be clearly seen that while the phase – or drift – error is independent of the grid resolution, the coarser grids are noticeably more dissipative. This is particularly noticeable in this case due to the higher wave modes which are much less resolved on the coarser grids.
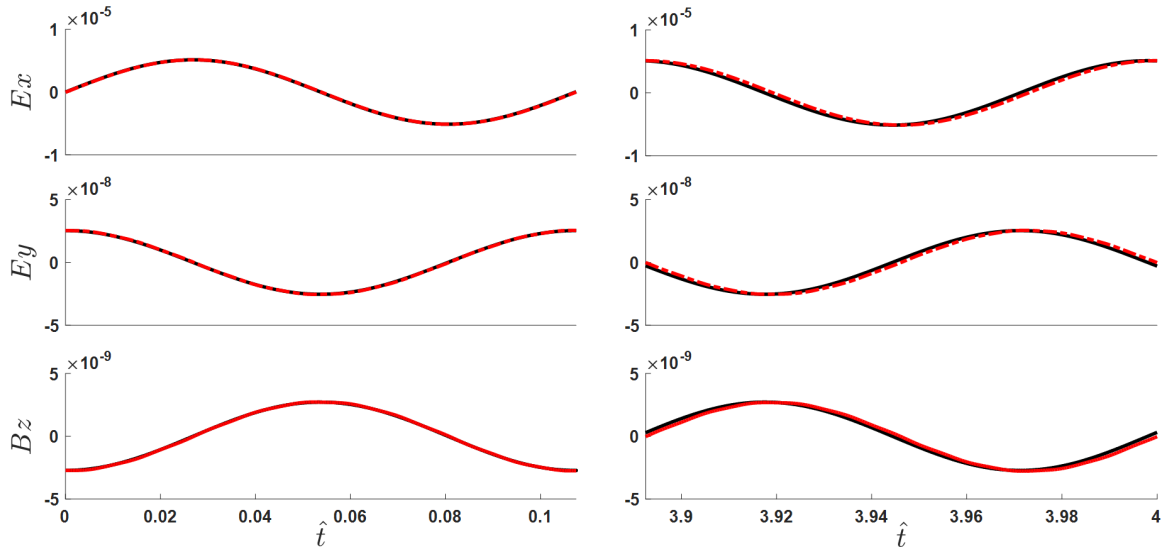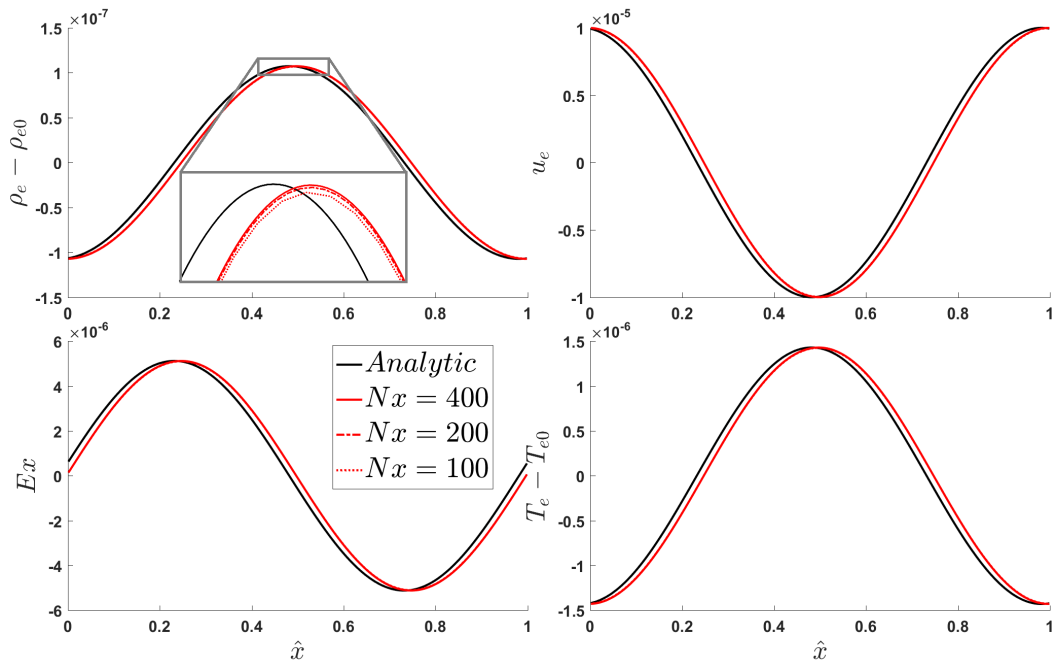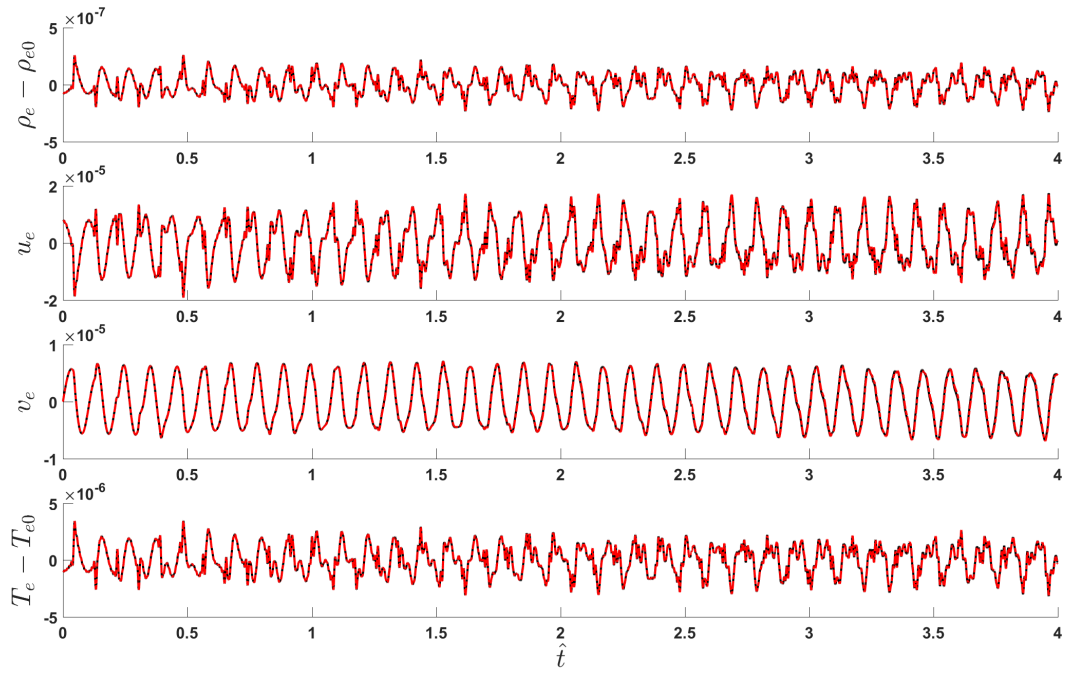
Figure 5.23: Electron fluid variables at $\hat{x} = 0.25$ for $\hat{t} = 0 - 4$. Analytic solution (solid black) vs. the computed solution (dashed red) – approximate square wave
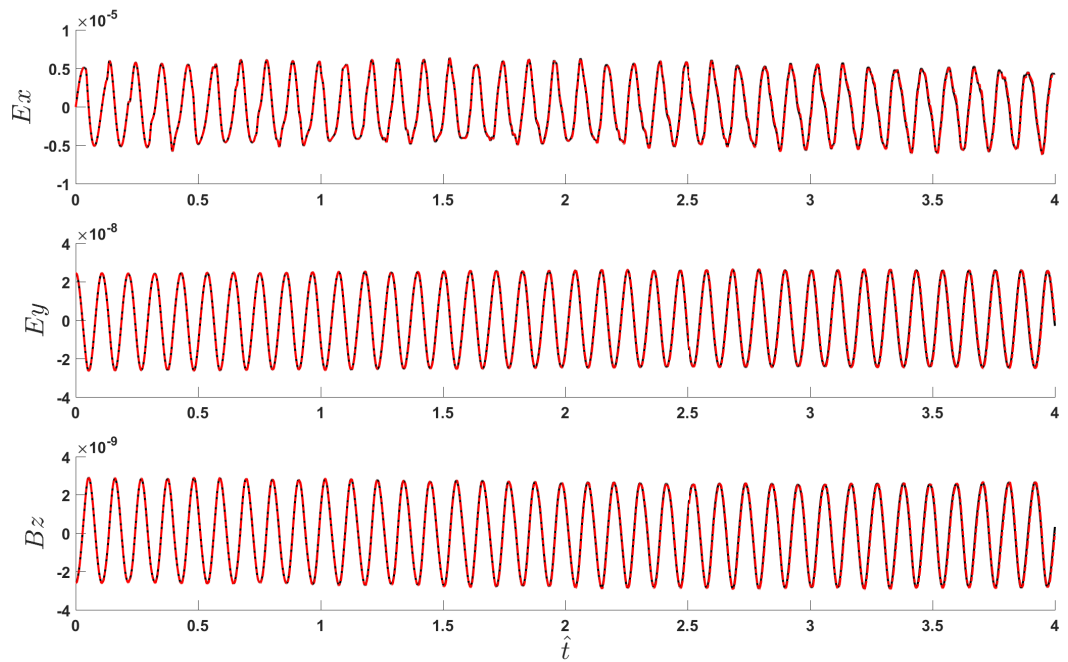
Figure 5.24: Electromagnetic fields at $\hat{x} = 0.25$ for $\hat{t} = 0 - 4$. Analytic solution (solid black) vs. the computed solution (dashed red) – approximate square wave

Figures 5.23 and 5.24 compare the numerical and analytic solutions in time for the electron fluid and electromagnetic fields at $\hat{x} = 0.25$. The normalized L_1 error for the fluid variables in time is depicted in Figure 5.25 and Figure 5.26 shows the L_1 error for the electromagnetic fields. The error in the EM fields appears very steady after an initial jump, while the fluid quantities exhibit a slow increase in error relative to the analytic solution over time. As discussed, this is due mostly to developing nonlinearities in the governing equations.
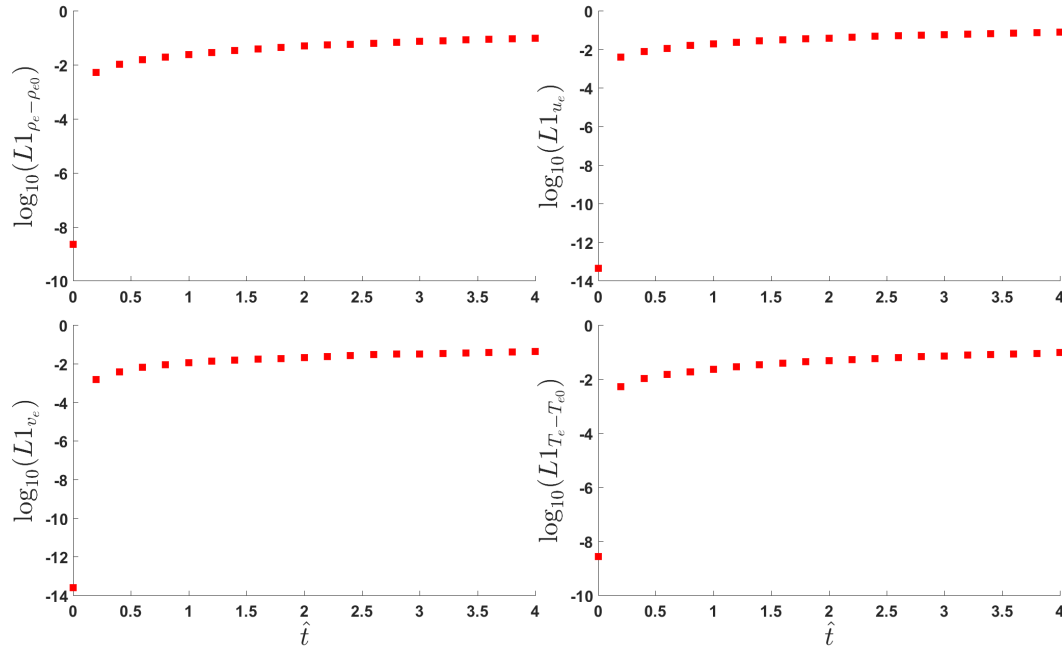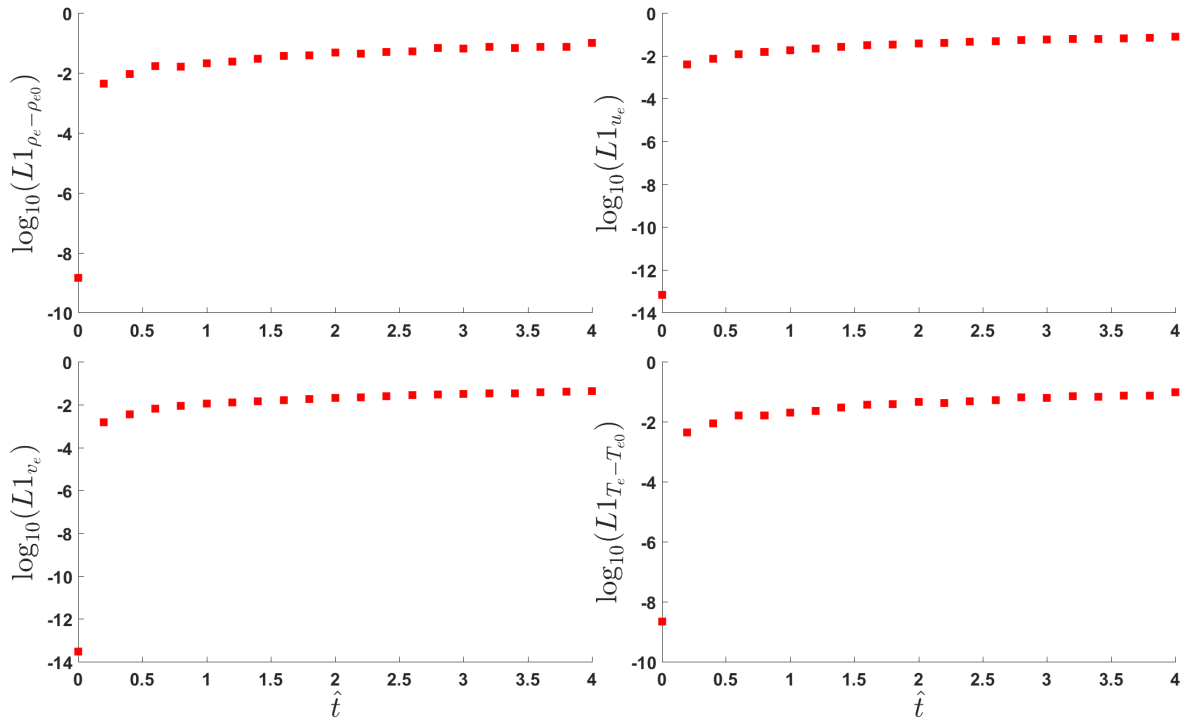

Figure 5.25: Base-10 logarithm of the normalized L_1 error for electron fluid variables for $\hat{t} = 0 - 4$ – approximate square wave
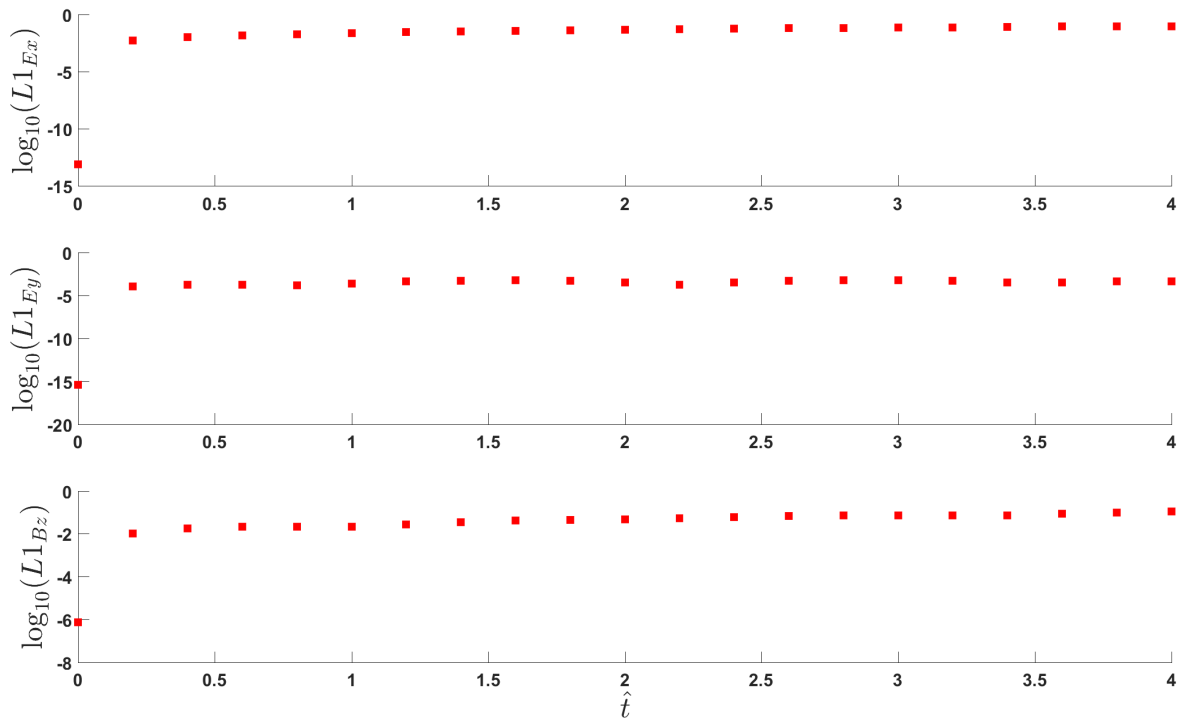
Figure 5.26: Base-10 logarithm of the normalized L_1 error for electromagnetic fields for $\hat{t} = 0 - 4$ – approximate square wave

5.2.3 Inter-species Collisional Damping

Here we demonstrate the resistive effects in the linearized case. For this case we use only the single wave mode as the scheme has demonstrated that multiple wave modes work equally well.
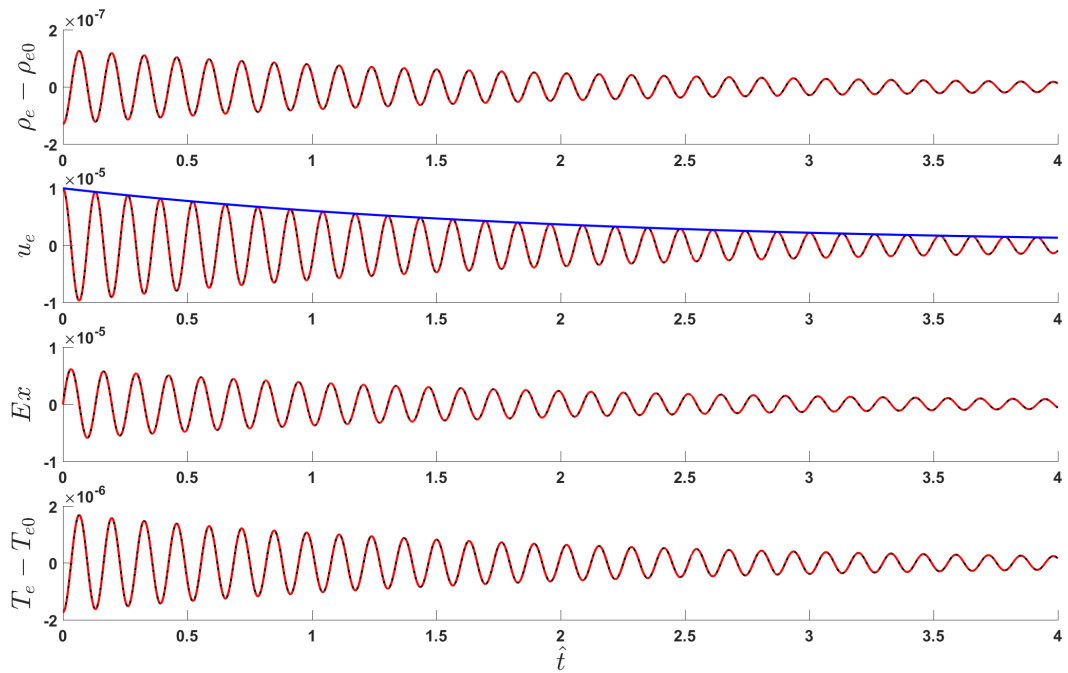
Figure 5.27: U_x, T, ρ and E_x at $\hat{x} = 0.25$ for $\hat{t} = 0 - 4$. Analytic solution (solid black) vs. the computed solution (dashed red) for a single mode and no B_z, E_y, U_y. The blue line is the exponential decay for $\exp[-\Im(\omega)t]$
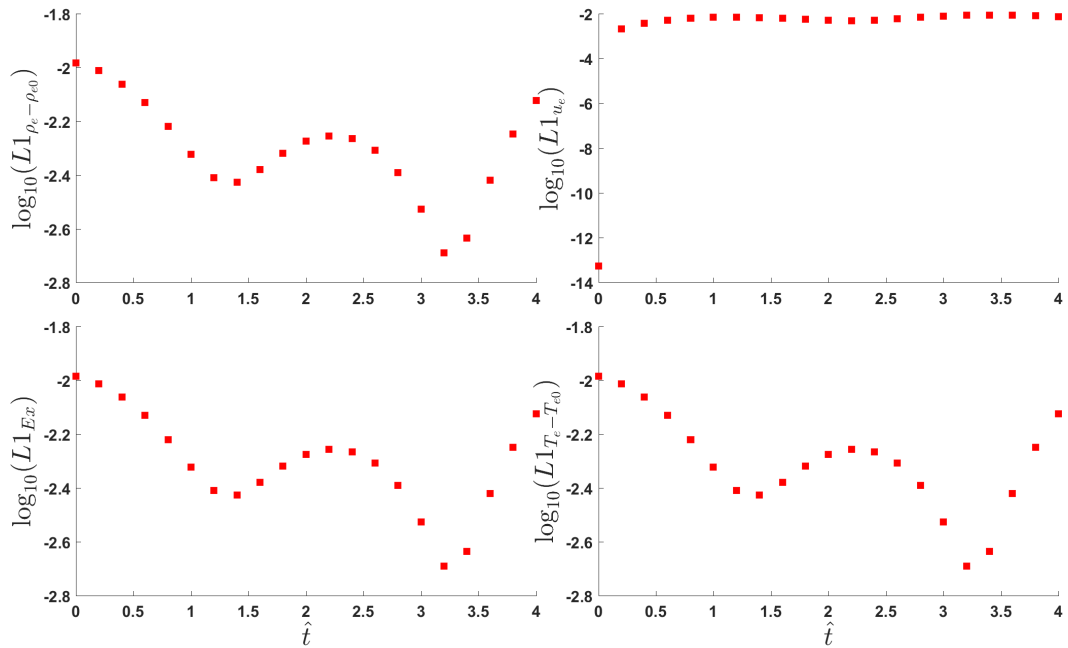
Figure 5.28: Base-10 logarithm of normalized L_1 error for $\hat{t} = 0 - 4$

In Figure 5.27 we see the solution for the electron fluid properties at a single point for the entire solution time, similar to Figure 5.13. Overlaid on the graph of electron x-velocity u_e is a blue line for $u_0 \exp\left(-\frac{t}{2\tau_{ei}}\right)$. It is easy to see that the exponential decay rate predicted by the linear analysis is obtained exactly. For this problem the ions have been fixed to be stationary (approximating their much larger mass and slower response time), so the perturbations all decay towards zero.

5.2.4 Conclusions

In this Chapter we present a linearized analysis of the governing equations for a two-fluid plasma. The linearization assumes infinitely massive stationary ions, and a non-relativistic plasma – $\omega \ll ck$. The two-fluid plasma GKS scheme is benchmarked against linearized analytic solutions for both a single wave mode – $k = 2\pi$ – as well as solutions corresponding to an approximate square wave for the electron x-velocity u_e. Simulations compare both the full system evolution, as well as a comparison of the PHM solver by itself by prescribing the fluid variables to their analytic solutions. For the single-mode full-system simulations The inter-species resistive term is tested. We make several observations from these simulations:

1. The solutions of the PHM equations using the prescribed analytic fluid solutions are very good, with very small relative error which does not appear to grow appreciably even for long times.

2. Overall the agreement between the full TFPGKS scheme and the analytic solutions is very good, particularly for the initialization for an approximate square mode. However, at long times some nonlinear error begins to appear – e.g., 40 periods for the $k = 2\pi$ mode or longer.

3. The resistive TFPGKS solutions match the analytic exponential damping rate derived from the linearized resistive governing equations.

74

6. NUMERICAL SIMULATIONS: VERIFICATION, VALIDATION, AND PARAMETRIC STUDIES

The objective of this Section is to perform numerical simulations using the Two-Fluid Plasm GKS method to exhibit its applicability in various parametric regimes. Specifically four types of computations are performed:

1. *Implied constitutive relationship*: The intent of these zero-dimensional calculations is to demonstrate that TFPGKS yields the known constitutive relationships for stress and heat flux when corresponding distributions are used as initial conditions. As mentioned in earlier sections, TFPGKS is developed to capture transient effects due to evolution in the distribution function. Yet it is equally important to demonstrate that the correct effective constitutive relationship is recovered from the initial TFPGKS distribution. The focus will be on capturing the anisotropy in the TFPGKS flux stress and heat flux due to the presence of the magnetic field as the Hall parameter ϖ is varied.

2. *Validation against established data*: The purpose of these calculations is to demonstrate that TFPGKS captures the correct governing equations in the linearized limit, and that it replicates well-known 1-D computational results. The goal is not only to establish validity of the model, but also to exhibit computational viability.

3. *Parametric study to demonstrate improved capability*: In these simulations we aim to explore transient behavior and new physics of the electromagnetic shocks in the collisional regime. The goal of these simulations is also to demonstrate the improved physics capturing capability over previous iterations of the TFPGKS scheme.

6.1   Analysis of Stress and Heat Flux Constitutive Relationships

As a benchmark to verify that the analytic expression of the TFPGKS flux behaves as expected, a zero-dimensional implementation of equation (3.74) was done in Mathematica.

In this implementation, the analytic expressions of the gradients $\frac{\partial g}{\partial x}$ and $\frac{\partial g}{\partial t}$ with respect to the gradients $\frac{\partial \rho}{\partial x}$, $\frac{\partial T}{\partial x}$, and $\frac{\partial u}{\partial x}$ are directly implemented. For this analysis we assume a smooth solution of the flow variables, and specify the state of the flow – including gradients – at an arbitrary point in space in time. Only one species is examined in this analysis, which is taken to be the electrons for convenience. The analysis is valid for either species, as the primary parameter of significance is the Hall parameter ϖ.

We calculate the time-dependent heat flux and viscous stress using TFPGKS, while comparing to the constitutive model of Woods [34] – which we expect to recapture in this limit – as well as Braginskii's model [53]. The TFPGKS flux is calculated using both the "Coupled" flux, as well as the "Uncoupled" flux which ignores the effects of the acceleration on the MoC solution and the modification to the non-equilibrium portion of the distribution $f^{(1)}$.

For this problem, the coordinate system is taken to be oriented such that the magnetic field is aligned along the z-axis, i.e. $\boldsymbol{B} = B\hat{\boldsymbol{z}}$. The temperature and velocity gradients are chosen somewhat arbitrarily to be

$$\boldsymbol{\nabla} T = \begin{bmatrix} 1.0 \\ -1.0 \\ 1.0 \end{bmatrix}, \quad (6.1) \qquad \boldsymbol{\nabla}\boldsymbol{u} = \begin{bmatrix} 1.5 & 1.3 & 1.0 \\ 0.5 & -1.0 & -1.0 \\ -2.0 & 1.0 & 2.0 \end{bmatrix}, \qquad (6.2)$$

such that they are partially aligned along the magnetic field. Other values of $\boldsymbol{\nabla} T$ and $\boldsymbol{\nabla}\boldsymbol{u}$ were also tested, and exhibited identical behavior as expected.

$$\langle \boldsymbol{\xi} \bar{f} \rangle = \bar{\boldsymbol{F}}^\rho = \overline{\rho \boldsymbol{u}} \qquad (6.3)$$

To calculate the TFPGKS stress and heat flux, we define the TFPGKS momentum in equation (6.3). To obtain the TFPGKS fluid velocity, we define the TFPGKS density to be $\bar{\rho} \equiv \rho$.

$$\overline{\boldsymbol{u}} \approx \frac{\boldsymbol{F}^\rho}{\rho} \qquad (6.4)$$

76

Thus, equation (6.4) will provide the TFPGKS mean velocity, defined in terms of the TF-PGKS mass flux. From this, we recall the definition of the stress and heat flux, given by equations (6.5) and (6.6).

$$\overline{\underline{\Phi}} \equiv \langle (\boldsymbol{\xi} - \overline{\boldsymbol{u}})(\boldsymbol{\xi} - \overline{\boldsymbol{u}})\bar{f} \rangle \tag{6.5}$$

$$\overline{\boldsymbol{q}} \equiv \langle \frac{1}{2}(\boldsymbol{\xi} - \overline{\boldsymbol{u}})(\boldsymbol{\xi} - \overline{\boldsymbol{u}})^2 \bar{f} \rangle \tag{6.6}$$

From equations (6.5) and (6.6), we can define the TFPGKS stress and heat flux in terms of the TFPGKS fluxes and TFPGKS mean velocity.

$$\overline{\underline{\Phi}} = \underline{\boldsymbol{F}}^{\rho u} - \rho \overline{\boldsymbol{u}}\overline{\boldsymbol{u}} \tag{6.7}$$

$$\overline{\boldsymbol{q}} = \boldsymbol{F}^{\varepsilon} - \frac{1}{2}\rho \overline{\boldsymbol{u}}\overline{\boldsymbol{u}}^2 - \frac{1}{2}\overline{\boldsymbol{u}}\operatorname{Tr}\left(\underline{\boldsymbol{F}}^{\rho u}\right) + \frac{1}{2}\overline{\boldsymbol{u}}^2 \boldsymbol{F}^{\rho} - \overline{\boldsymbol{u}} \cdot \underline{\boldsymbol{F}}^{\rho u} + \overline{\boldsymbol{u}}\overline{\boldsymbol{u}} \cdot \boldsymbol{F}^{\rho} \tag{6.8}$$

The results presented are normalized by the absolute value of the $\hat{b}$-parallel component, and are scaled so that the heat fluxes all converge in the $\varpi \to 0$ limit. The heat fluxes for Woods' [34] and Braginskii's [53] models are given in equations (6.9) – (6.10):

$$q_{W,i} \equiv -\kappa_{W,ij}\frac{\partial T}{\partial x_j}, \tag{6.9}$$

$$q_{B,i} \equiv -\kappa_{B,ij}\frac{\partial T}{\partial x_j}. \tag{6.10}$$

Where the tensor thermal conductivities $\kappa_{W,ij}$ and $\kappa_{B,ij}$ are defined by

$$\kappa_{W,ij} \equiv \kappa_{\parallel}b_i b_j + \kappa_{W,\perp}\left[\delta_{ij} - b_i b_j\right] - \kappa_{W,\wedge}\epsilon_{ikj}b_k, \tag{6.11}$$

$$\kappa_{B,ij} \equiv \kappa_{\parallel}b_i b_j + \kappa_{B,\perp}\left[\delta_{ij} - b_i b_j\right] - \kappa_{B,\wedge}\epsilon_{ikj}b_k. \tag{6.12}$$

The perpendicular ($\perp$) and transverse ($\wedge$) thermal conductivity are defined for each to be

$$\kappa_{W,\perp} \equiv \kappa_{\parallel} \frac{1}{1 + \varpi^2} \tag{6.13}$$

$$\kappa_{W,\wedge} \equiv \kappa_{\parallel} \frac{\varpi}{1 + \varpi^2} \tag{6.14}$$

$$\kappa_{B,\perp} \equiv \kappa_{\parallel} \frac{1 + 0.756\varpi^2}{1 + 3.988\varpi^2 + 1.477\varpi^4} \tag{6.15}$$

$$\kappa_{B,\wedge} \equiv \kappa_{\parallel} \frac{\varpi \left(0.954 + 1.758\varpi^2\right)}{1 + 3.988\varpi^2 + 1.477\varpi^4} \tag{6.16}$$

Clearly, the expected behavior is that the components parallel to B will be unaffected in all models, while the component of the "Fourier" heat flux – i.e. the heat flux in the $\varpi \to 0$ limit – perpendicular to B will be reduced as ϖ increases due to the action of the magnetic field to reduce transport across itself. Further, the "transverse" component which does not exist in the $\varpi \to 0$ limit, will initially increase as ϖ increases, but will also asymptote to zero at large ϖ. This can be rationalized physically by thinking of it as the perpendicular heat flux being "redirected" by the magnetic field. The viscous stresses behave in a qualitatively similar manner, and the details of their models may respectively be found in Section 12.7 of [34] (pp. 296–299) and Section 4 of [53] (pp. 249–253).

Figure 6.1 shows the three components of the heat flux vector comparing Coupled TF-PGKS with Woods' and Braginskii's models, as well as with the naive Uncoupled TFPGKS implementation which neglects the effects of the electromagnetic fields. It can be seen that the Uncoupled TFPGKS flux is not affected by variation in ϖ, while for the Coupled TF-PGKS, Woods, and Braginskii models the heat flux is only constant for q_3 – the component parallel to $\hat{b}$. For the x- and y- components of heat flux – q_1 and q_2 – there is significant dependence on ϖ between $10^{-0.8} \lesssim \varpi \lesssim 10^{0.8}$. Outside this boundary the components of heat flux asymptote to the unmagnetized value for low ϖ and to 0 at large ϖ. This indicates that the stronger magnetic field will eliminate cross-field collisional heat transport.

Figure 6.2 shows the six independent components of the stress tensor (less the isotropic pressure component $p\underline{1}$), comparing Coupled and Uncoupled TFPGKS with Woods' and
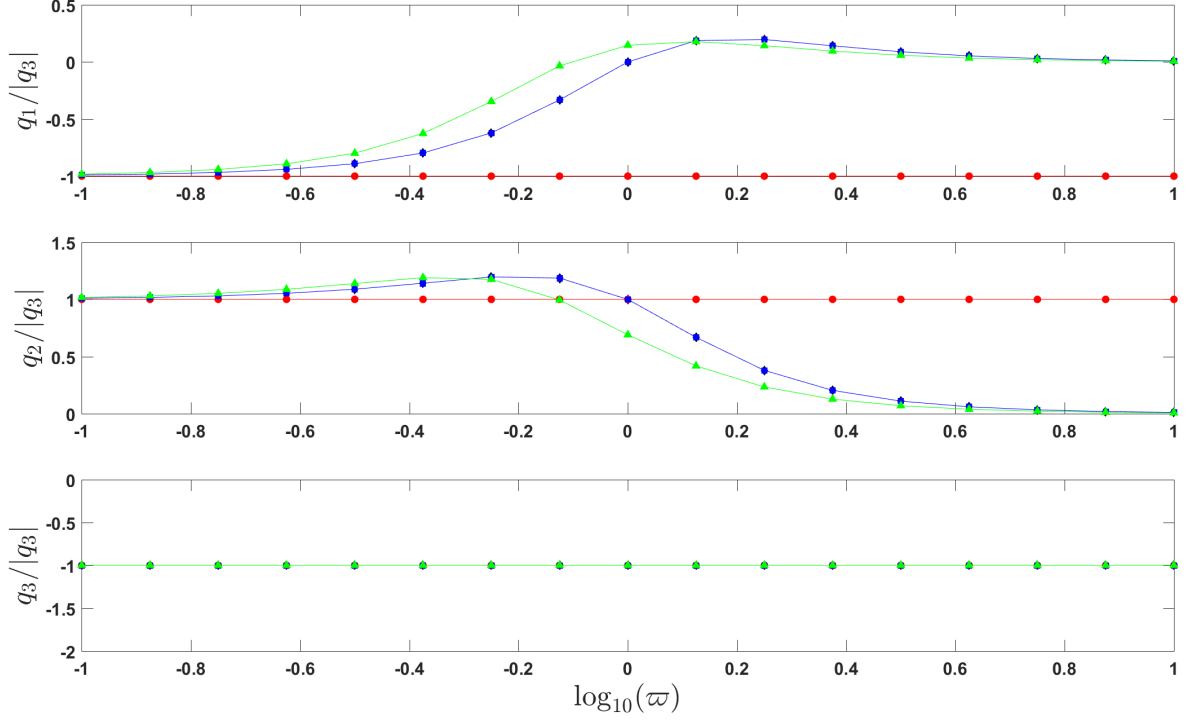
Figure 6.1: Top: X-component of heat flux; Middle: Y-component of heat flux; Bottom: Z-component of heat flux, normalized by the parallel heat flux vs. base-10 logarithm of the Hall parameter. Comparing TFPGKS and Woods (blue) to Braginskii (green), and the Uncoupled TFPGKS flux (red). $\boldsymbol{B} = |B|\hat{\boldsymbol{z}}$

Braginskii's models. Again, it can be seen that the Uncoupled TFPGKS stress is not affected by variation in ϖ, while for the Coupled TFPGKS, Woods, and Braginskii models the stress is only constant for S_{33} – the component purely parallel to $\hat{b}$. For the other components there is again significant dependence on ϖ between $10^{-0.8} \lesssim \varpi \lesssim 10^{0.8}$. For large ϖ, the transverse components of stress – S_{12}, S_{13}, and S_{23} – all asymptote to zero. Note that the S_{11} and S_{22} components do not go to zero, since $\mathrm{Tr}\,\overline{\overline{\boldsymbol{\Phi}}} = 0$ must be true. This assumes that the scalar pressure p is defined $p \equiv -\frac{1}{3}\,\mathrm{Tr}\,\underline{\boldsymbol{P}}$, where $\underline{\boldsymbol{P}}$ is the total stress tensor.
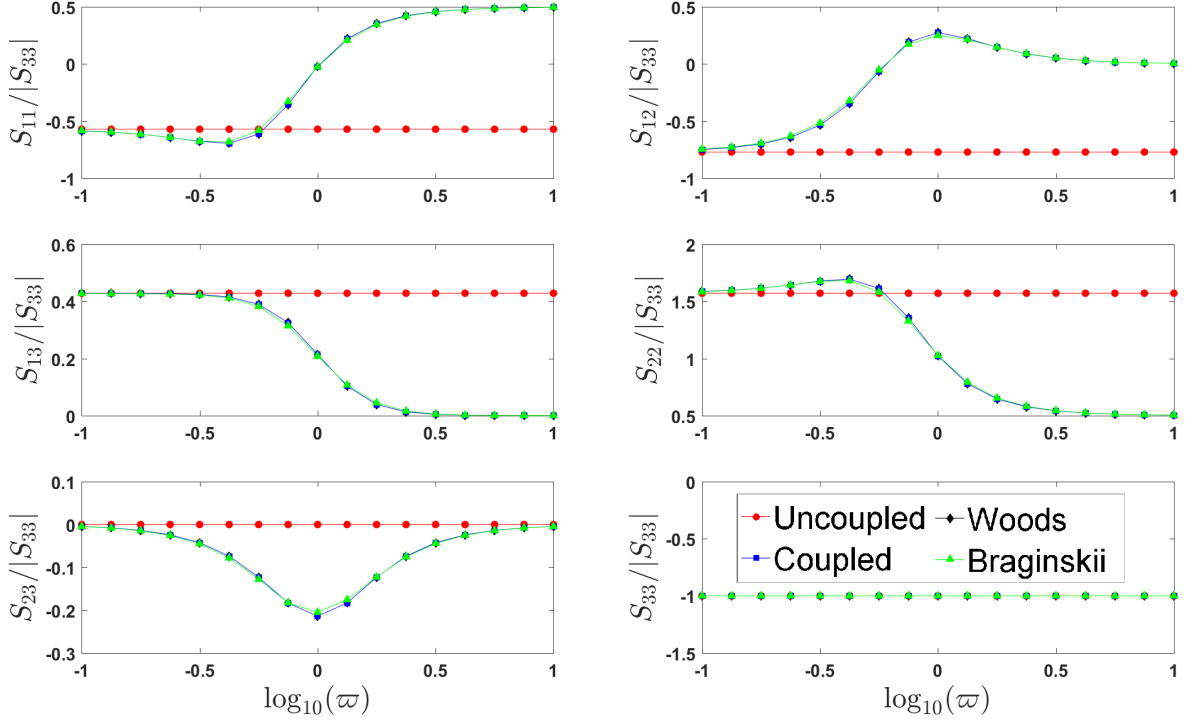
Figure 6.2: Comparison of individual components of the viscous stress tensor, normalized by the purely parallel component vs. base-10 logarithm of the Hall parameter. Comparing TFPGKS and Woods (blue) to Braginskii (green), and the non-magnetized TFPGKS flux (red). $\boldsymbol{B} = |B|\hat{\boldsymbol{z}}$

6.2 Two-Fluid Electromagnetic Shocks

The two-fluid electromagnetic shock is a generalization of the problem conceived by Brio and Wu [52] for ideal MHD. It has been used in references [2, 3, 4, 5, 6] as a canonical problem for benchmarking solvers for the ideal two-fluid plasma equations. In the problem set up the ratio of the Larmor radius and Debye length is fixed to $\hat{r}_L/\hat{\lambda}_D = 10^2$. The mass ratio is set to a realistic value of $M = 1836$ to mirror the electron-proton mass ratio. The problem is one-dimensional with $\hat{x} = [0, 1]$. The variables are split with a discontinuity at $\hat{x} = 0.5$. Table 6.1 shows the initialization of the left- and right-hand states. The boundary conditions are straightforward zero-gradient Neumann boundaries for all quantities except ϕ and ψ which are set to zero [48]. A typical simulation for these cases comprises a domain of $Nx = 1000$ cells – i.e. $\Delta x = 0.001$, with $\Delta t = 1 \times 10^{-6}$. All the results presented here are

reasonable well grid-resolved.

Table 6.1: Initialization for EM shock

	Left	**Right**
ρ_e	$1.0\frac{1}{M}$	$0.125\frac{1}{M}$
p_e	0.5	0.05
ρ_i	1.0	0.125
p_i	0.5	0.05
B_x	0.75	0.75
B_y	1.0	-1.0

Figure 6.3 shows the ion density for $\hat{r}_L = 10^3$ compared to the total density of the gasdynamic solution (replicated from [2]). It can be seen that for the parametric regime of
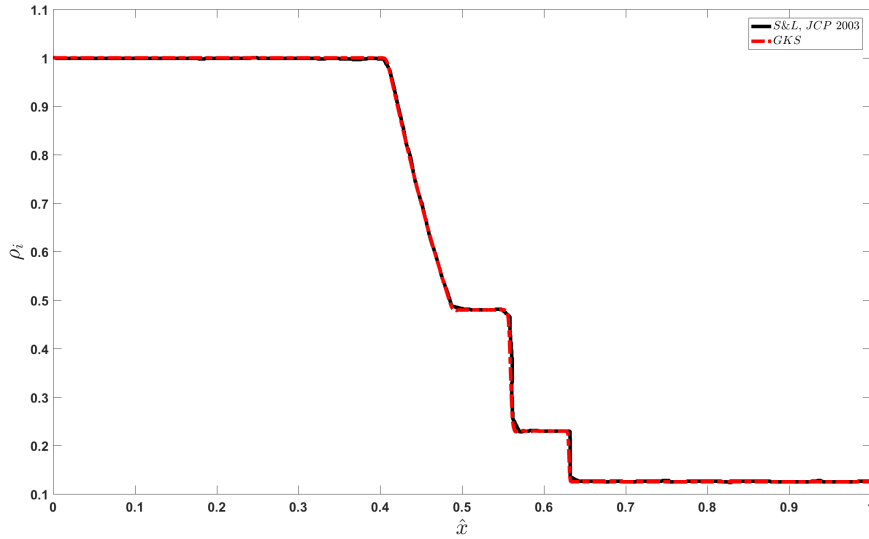
Figure 6.3: Electromagnetic shock, solution of ρ_i for $\hat{r}_L = 10^3$, compared to the gasdynamic solution from Shumlak and Loverich [2]

large $\hat{r}_L$, the shock evolution is essentially identical to the gasdynamic solution. The electron
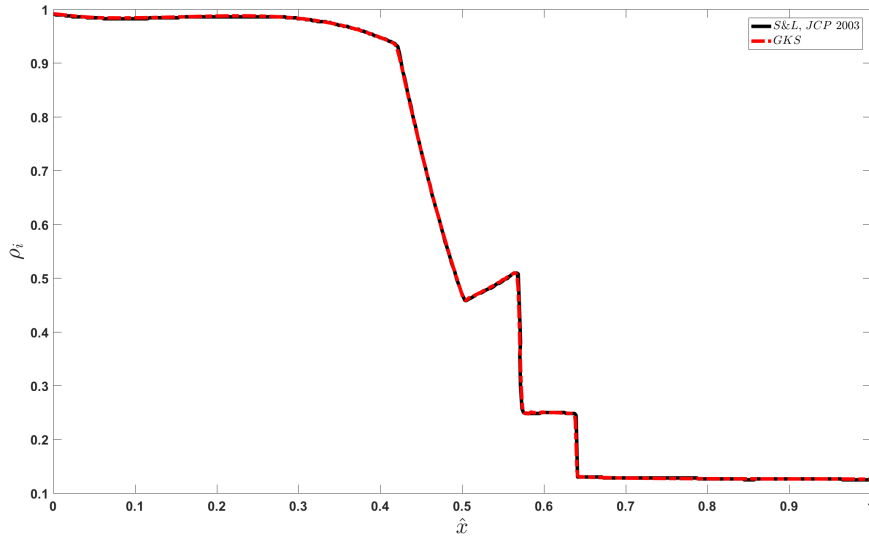
Figure 6.4: Electromagnetic shock, solution of ρ_i for $\hat{r}_L = 10^1$, compared to Shumlak and Loverich [2]

density is not depicted here but it is essentially decoupled entirely from the ion solution. The solution of ρ_i for $\hat{r}_L = 10^1$ is shown in Figure 6.4, where comparison is made to [2]. The results are essentially indistinguishable here, where we can see that the solution has begun to deviate very noticeably from the pure gasdynamic solution. The electromagnetic coupling between the electron and ion fluids is still quite weak in this regime. The solution of ρ_i for $\hat{r}_L = 10^0$ is shown in Figure 6.5, where comparison is made to [2, 3, 4]. The results for TFPGKS agree very closely with [2] and [3], while there is some very slight deviation from [4] near $\hat{x} = 0.2$ and $\hat{x} = 0.5$ (see the enlarged insets in Figure 6.5). Here the solution has deviated significantly from the gasdynamic solution and very distinctly captures the two-fluid physics which would not be captured in even the Hall-MHD solution. In this regime the coupling between the electrons and ions is more significant, and Figure 6.6 compares the electron density – multiplied by the mass ratio M – to the results of [3, 4]. Like the ion density, the agreement here is very close. Figure 6.7 depicts the TFPGKS EM shock solution for ρ_i compared to Loverich et al. [5]. We note that for both the TFPGKS an HLS solutions here, the solution domain is the center 10% of the computational domain – i.e. the numerical
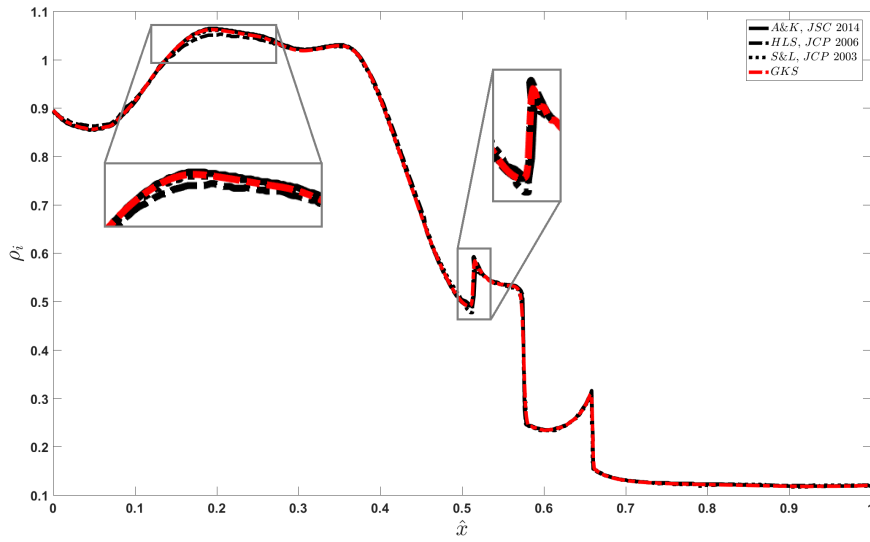
Figure 6.5: Electromagnetic shock, solution of ρ_i for $\hat{r}_L = 10^0$, compared to Abgrall and Kumar [3], Hakim et al. [4], and Shumlak and Loverich [2]
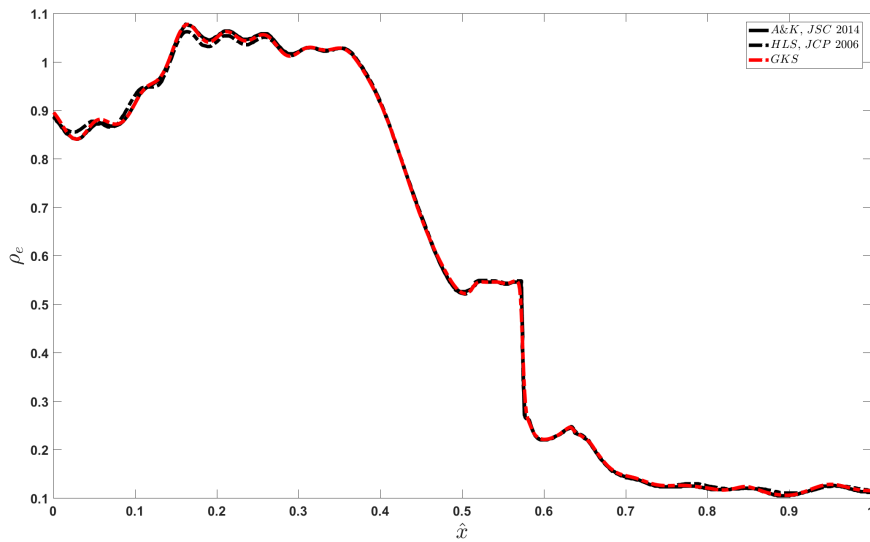
Figure 6.6: Electromagnetic shock, solution of ρ_e for $\hat{r}_L = 10^1$, compared to Abgrall and Kumar [3] and Hakim et al. [4]

boundaries are effectively at $\hat{x} = \pm 4.5$. This is done to minimize boundary effects on the solution in the domain $\hat{x} = [0, 1]$. Here the solution has started to exhibit more of the features
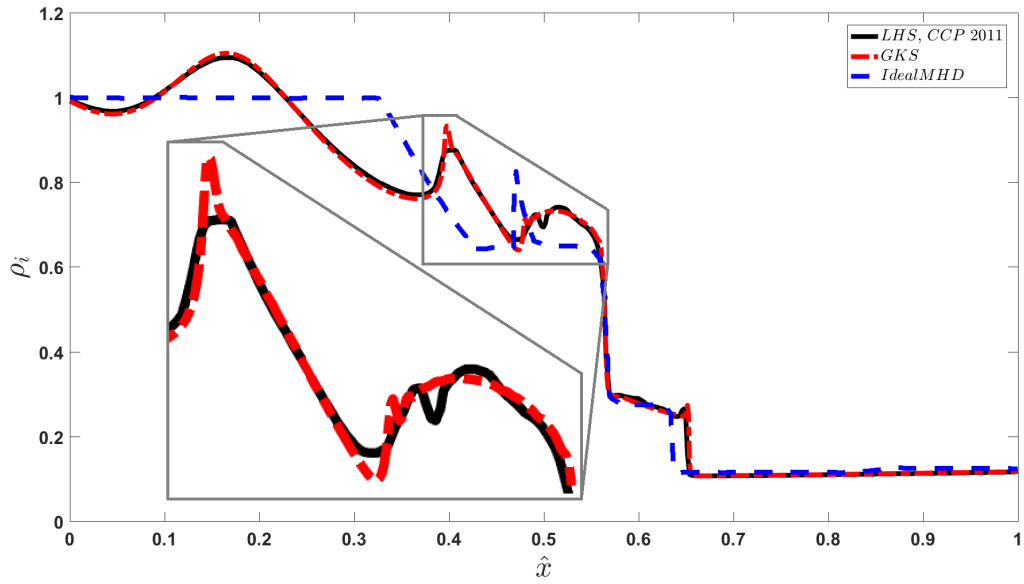
Figure 6.7: Electromagnetic shock, solution of ρ_i for $\hat{r}_L = 10^{-1}$, compared to Loverich et al. [5]

of the canonical Brio and Wu MHD solution [52] – particularly the characteristic "spike" at $\hat{x} = 0.5$ – though they are not quite in the same place. This is due to charge separation effects and incomplete magnetization at finite $\hat{r}_L$; the MHD solution effectively resides in the $\hat{r}_L \to 0$ limit. As quasineutrality becomes more strongly enforced due to decreasing $\hat{\lambda}_D$, and both species become more tightly bound to the magnetic field due to decreasing $\hat{r}_L$, the solution will continue to approach the ideal MHD solution. The agreement between TFPGKS and [5] is reasonably good, with the most significant differences appearing in the peak near $\hat{x} = 0.4$ and the hump at $\hat{x} = 0.5$ (shown in the enlarged inset of Figure 6.7). The difference is primarily due to the result of Loverich et al. [5] having more numerical diffusion. This is because of their result being obtained on a slightly coarser grid.

6.3 PHM Validation

In Chapter 5 we looked at an initial benchmark of the PHM solver using the linearized analytical solution of the governing equations. No significant errors were observed; however, this may have been a result of the simplistic nature of that test. To further test the PHM solver

we will look at the electromagnetic shock with $\hat{r}_L = 10^0$ for several values of ζ_ϕ. As $\zeta_\phi \to 0$, the PHM equations will go towards the regular Maxwell's equations. As $\zeta_\phi \to \infty$ we expect that violations of equation (2.18) to be eliminated asymptotically $-\boldsymbol{\nabla}\cdot\boldsymbol{E} - \frac{\rho_Q}{\epsilon_0} \to 0$. However, for $\zeta_\phi > 1$ there will be an impact to numerical efficiency as the characteristic speed for eliminating divergence errors from $\boldsymbol{E}$ is $\zeta_\phi \hat{c}$.
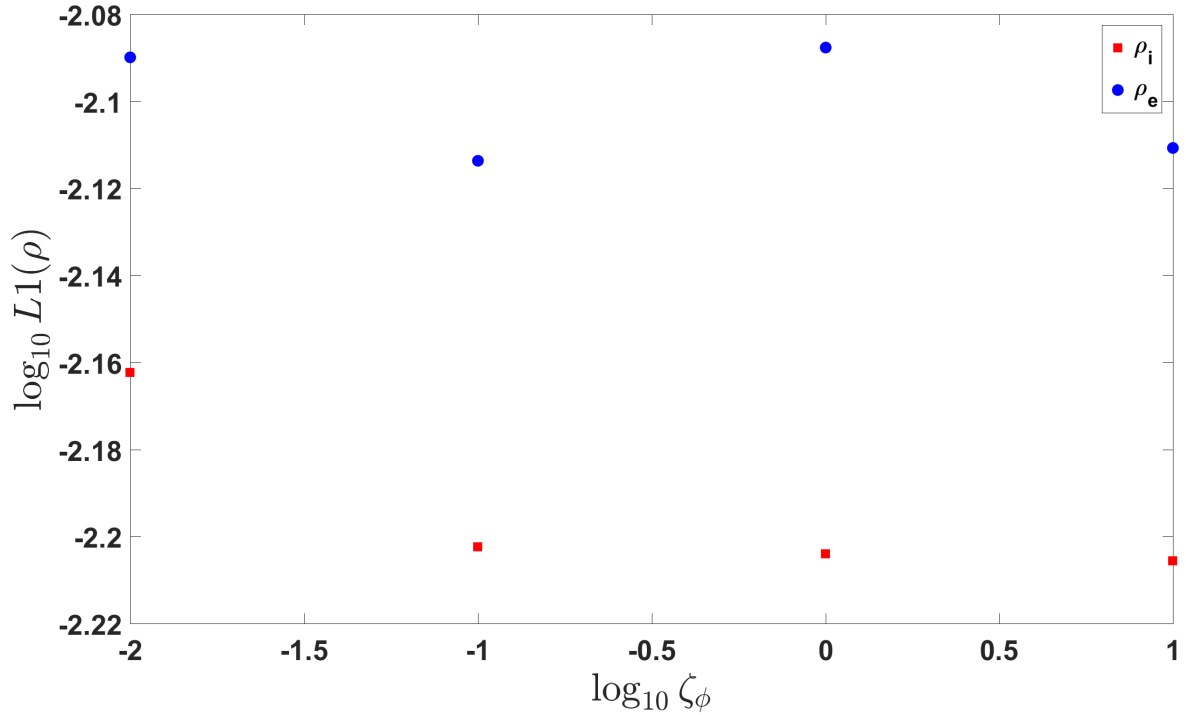
Figure 6.8: Log base 10 of L_1 difference in ρ_e and ρ_i for $\hat{r}_L = 10^0$ relative to the digitized data of Abgrall and Kumar [3]

In Figure 6.8 the L_1 norm of error in the ion and electron densities relative to the data digitized from [3] – see figures 6.5 and 6.6 – and normalized by the L_1 norm of the data from Abgrall and Kumar. For the electrons the error appears to be steady, and although it fluctuates slightly, does not appreciably increase or decrease. For the ions, the error is initially not very significant but decreases from $\zeta_\phi = 10^{-2}$ to $\zeta_\phi = 10^{-1}$ and is steady after that. The actual divergence errors in the electric field can be seen in Figure 6.9 which depicts the L_1 norm
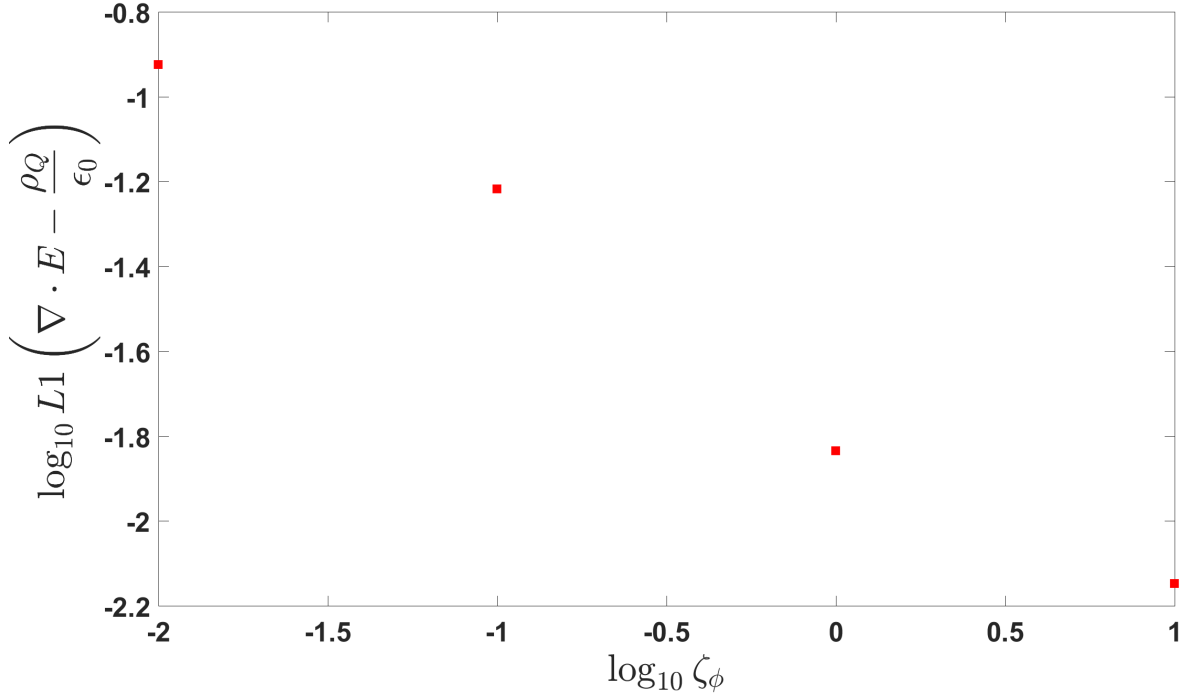
Figure 6.9: Log base 10 of L_1 difference in $\boldsymbol{\nabla} \cdot \boldsymbol{E}$

of $\boldsymbol{\nabla} \cdot \boldsymbol{E} - \frac{\rho_Q}{\epsilon_0}$ normalized by the L_1 norm of the electric field divergence. As expected, the divergence error decreases asymptotically with increasing ζ_ϕ. Further it appears that the effects of changing ζ_ϕ are most significant between $0.1 < \zeta_\phi < 1.0$. However, as we saw in Figure 6.8 the effect on actual error in the physical quantities – ρ_i or ρ_e – was not as significant. Figures 6.10 and 6.11 show the charge density and the electric field respectively for the EM shock with $\hat{r}_L = 10^0$ while varying ζ_ϕ. It can be seen that there is no real appreciable change in the physical quantities even through three orders of magnitude in ζ_ϕ – although a decrease in divergence error by an order of magnitude is achieved. Clearly for at least these simple problems, small changes in ζ_ϕ do not have a significant effect on the overall numerical solution of the conserved quantities.

The reason for this is most likely that for a one-dimensional computation such as this the divergence error is quite low to begin with and the problem is not complex enough to truly give rise to errors in $\boldsymbol{\nabla} \cdot \boldsymbol{E}$ or $\boldsymbol{\nabla} \cdot \boldsymbol{B}$ which would cause significant errors in the resulting

86
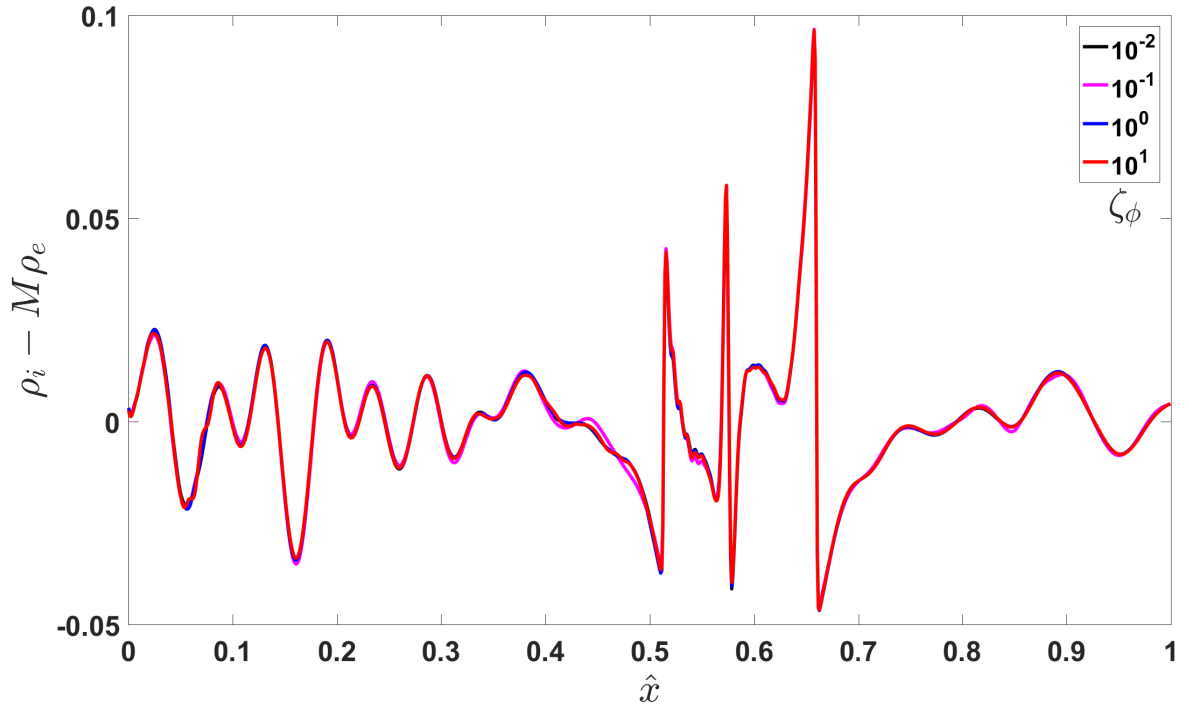
Figure 6.10: Charge density along shock tube for $\hat{r}_L = 10^0$ for different ζ_ϕ

solution. A two-dimensional implementation of this problem such as in [43] where the shock is skewed across the domain would be much more appropriate for testing the Gauss' Law preserving qualities of the PHM equations for this implementation.
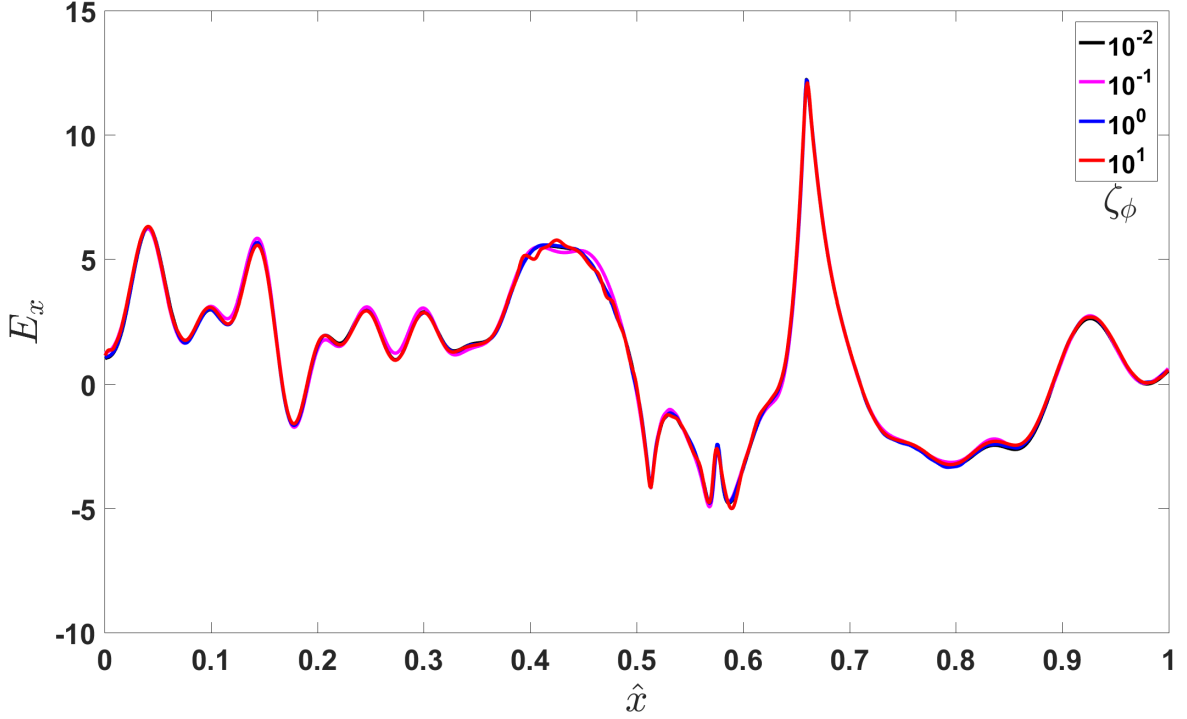
Figure 6.11: Axial electric field along shock tube for $\hat{r}_L = 10^0$ comparing various values of ζ_ϕ

6.4 Ion Acoustic Solitons

The simulation of ion acoustic solitons has also been studied by a number of authors [6, 54, 55, 56, 57], wherein it is established that an initial state of a density spike or hump in the two-fluid system will generate the soliton waves. This has also been observed experimentally in experiments with a density step excitation [58]. While the Kortewig-de-Vries (KdV) equation [59] is well known for being able to describe soliton wave propagation, the density-hump excited soliton solutions that are presented here and seen in e.g., [6] and [57] cannot be captured by the KdV equation because of the very strong nonlinear behavior. For this problem the mass ratio is set to $M = 25$. The electron pressure is $p_e = 5$ and the electron/ion temperature ratio is $T_e/T_i = 100$. The ratio of Larmor radius to Debye length is $\hat{r}_L/\hat{\lambda}_D = 1$, and they are set to $\hat{r}_L = \hat{\lambda}_D = 10^{-2}$. The problem is 1D with periodic boundaries. The domain is $\hat{x} = [0, L]$ where $L = 12l_i$. The ion skin depth is $l_i = \omega_{pi}/c$. The speed of light is

set to $\hat{c} = 100$. The initial profile for the ion density is given by equation (6.17) and shown in Figure 6.12.

$$\rho_i = 1 + \exp\left(-300\left|\frac{x}{L} - \frac{1}{3}\right|\right) \tag{6.17}$$

This profile is identical for ρ_e. The temperatures T_e and T_i are uniform, and all other variables are initialized to zero.
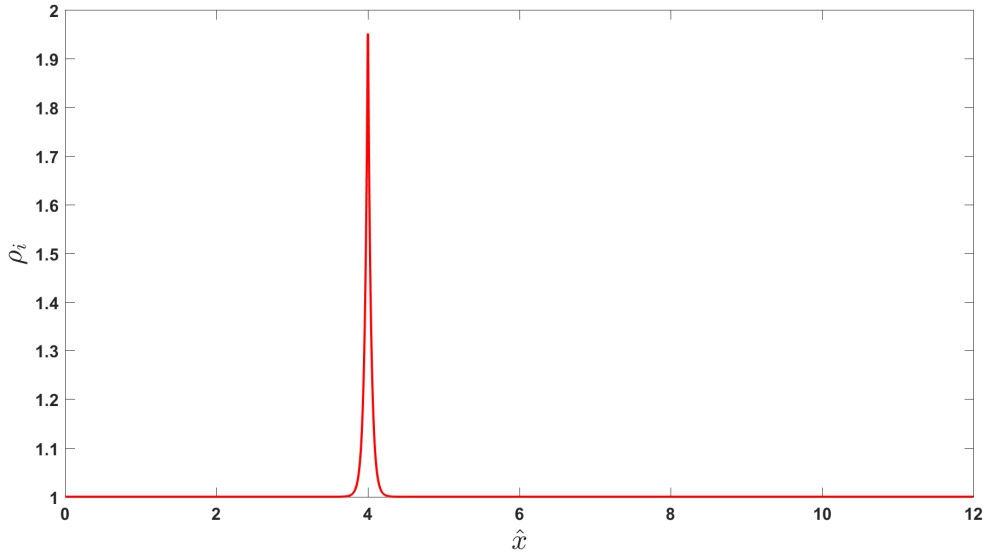
Figure 6.12: Ion acoustic soliton initial profile for density and pressure, equation (6.17)

The plasma acoustic speed may be defined $\hat{c}_s \equiv \sqrt{(\gamma_i \hat{T}_i + \gamma_e \hat{T}_e)\frac{M}{M+1}}$. The speed of the ion acoustic wave in the computed solution is roughly $\hat{c}_s = 2.9$, which is approximately 2% smaller than the theoretical value.

Figure 6.13 depicts the result at $\hat{t} = 5$ compared to [6]. The result of Kumar and Mishra was obtained on a grid of $10,000$ cells while the TFPGKS solution used only $3,000$ cells and is reasonably well-resolved. For a higher resolution the TFPGKS solution does not change appreciably. Kumar and Mishra observed that the entropy stable scheme they used in obtaining the results reproduced in Figure 6.13 was more diffusive than other schemes [6].
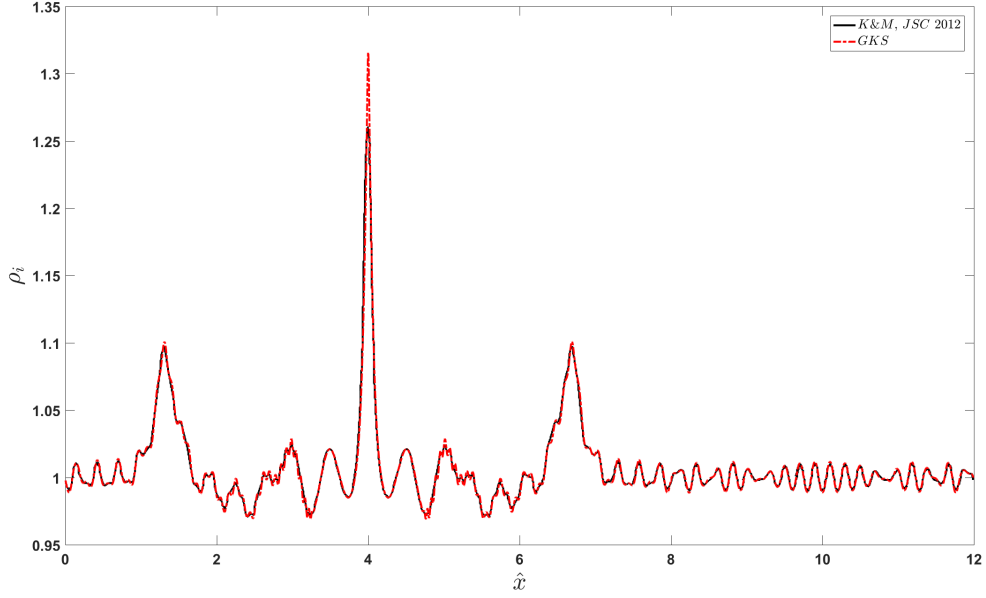
Figure 6.13: Ion acoustic soliton, comparison with Kumar and Mishra [6]

6.5 Parametric Study of Collisional EM Shocks

6.5.1 Setup and Parametrization

To examine the effects of finite collisionality and magnetization on the TFPGKS scheme, a parametric study was performed of the electromagnetic shocks seen in Section 6.2 in the regime of finite electron and ion self collision times τ_{ee} and τ_{ii}. Here we refer to the "Coupled" TFPGKS scheme as the current TFPGKS scheme, and the "Uncoupled" TFPGKS scheme as the previously developed TFPGKS scheme which neglects the effects of the electromagnetic fields (particuarly $\boldsymbol{B}$) and inter-species collisions on the TFPGKS flux evolution. The electromagnetic shock simulations were performed in the same manner as in Chapter 6 for $\hat{r}_L = 10^0$ and $\hat{r}_L = 10^{-1}$ while varying the ion-ion and electron-electron collision times. Figures 6.1 and 6.2 depicted the effects of varying the Hall parameter ϖ on the stress and heat flux. To clarify the notation used, here $\hat{r}_L$ is used to denote the parametric Larmor radius appearing in the non-dimensionalized equations (4.42), (4.43), (4.44),

and (4.47). This is distinguished from the effective normalized Larmor radius $r_{L,\alpha}$ for each species α.

$$r_{L,e} \equiv \frac{v_{th,e}}{\omega_{c,e}} = \frac{\sqrt{T_e}\hat{r}_L}{\sqrt{M}|\boldsymbol{B}|} \tag{6.18}$$

$$r_{L,i} \equiv \frac{v_{th,i}}{\omega_{c,i}} = \frac{\sqrt{T_i}\hat{r}_L}{|\boldsymbol{B}|} \tag{6.19}$$

$$\omega_{c,e} \equiv \frac{\hat{r}_L}{M|\boldsymbol{B}|} \tag{6.20}$$

$$\omega_{c,i} \equiv \frac{\hat{r}_L}{|\boldsymbol{B}|} \tag{6.21}$$

Equations (6.18) and (6.19) give the definition of the effective Larmor radius $r_{L,\alpha}$ while equations (6.20) and (6.21) give the definition of the effective cyclotron frequency $\omega_{c,\alpha}$. Note that the thermal velocities of each species are $v_{th,i} \equiv \sqrt{T_i}$ and $v_{th,e} \equiv \sqrt{MT_e}$ respectively.

$$\tau_{ee} \equiv \frac{\hat{\mu}_e}{\rho_e M T_e M^{\frac{1}{2}}} \tag{6.22}$$

$$\tau_{ii} \equiv \frac{\hat{\mu}_i}{\rho_i T_i} \tag{6.23}$$

The normalized self-collision times for ions and electrons are defined in equations (6.22) and (6.23). The normalized viscosity parameters $\hat{\mu}_e$ and $\hat{\mu}_i$ are essentially defined as the inverse Reynolds number for each species, relative to the species thermal velocity. That is, $\hat{\mu}_e \equiv \left(\frac{\rho_e v_{th,e} x_0}{\mu_e}\right)^{-1}$, where the quantities to the right of the equals sign are not non-dimensionalized. Thus, for the same non-dimensional viscosity, the ratio of self-collision times is $\tau_{ee}/\tau_{ii} = M^{-1/2}$, which is consistent with the analyses in Section 3.12 of [36], Section 1.1 of [60], and Section 5.3 of [31].

$$\varpi_e \equiv \tau_{ee}\omega_{c,e} = \frac{\hat{\mu}_e\sqrt{M}|\boldsymbol{B}|}{T_e M \rho_e \hat{r}_L} \tag{6.24}$$

$$\varpi_i \equiv \tau_{ii}\omega_{c,i} = \frac{\hat{\mu}_i|\boldsymbol{B}|}{T_i \rho_i \hat{r}_L} \tag{6.25}$$

From the collision time and the cyclotron frequency, the species Hall parameters are determined by equations (6.24) and (6.25). Thus, we see if the collision time ordering mentioned above is maintained by $\hat{\mu}_i \approx \hat{\mu}_e$, then the Hall parameter for the electrons will be larger by a factor of $\sim \sqrt{M}$.

$$\lambda_{ee} \equiv \tau_{ee} v_{th,e} = \frac{\hat{\mu}_e}{\sqrt{T_i} \rho_i} \tag{6.26}$$

$$\lambda_{ii} \equiv \tau_{ii} v_{th,i} = \frac{\hat{\mu}_i}{\sqrt{T_e} M \rho_e} \tag{6.27}$$

Alternatively the species mean free path $\lambda_{\alpha\alpha}$ may be defined from equations (6.26) and (6.27) using the effection collision time and thermal velocity of each species. From the mean free paths and the Larmor radii the species Hall parameters may alternatively be determined by equations (6.28) and (6.29).

$$\varpi_e \equiv \frac{\lambda_{ee}}{r_{L,e}} \tag{6.28}$$

$$\varpi_i \equiv \frac{\lambda_{ii}}{r_{L,i}} \tag{6.29}$$

Note that the definitions in equations (6.28) and (6.29) are equivalent to equations (6.24) and (6.25).

In the parametric study presented here, the collision times are varied such that the parametric sweep of ϖ is the same for both cases of $\hat{r}_L$. Table 6.2 shows the nominal parameters for each case. The initialization of the shocks is identical to the setup used in Section 6.2.

Table 6.2: Parametric variation for collisional EM shocks

Case	1.1	1.2	1.3	1.4	2.1	2.2	2.3	2.4
$\hat{r}_L$	10^0				10^{-1}			
$\hat{\mu}_e \times 10^4$	1.25	2.5	5.0	10.	0.125	0.25	0.5	1.0
$\hat{\tau}_{ee} \times 10^4$	4.7	9.3	19.	37.	0.47	0.93	1.9	3.7
$\hat{\lambda}_{ee} \times 10^3$	4.5	8.9	18.	36.	4.5	8.9	18.	36.
$\hat{\varpi}_e \times 10^0$	0.19	0.38	0.77	1.5	0.19	0.38	0.77	1.5
$\hat{\mu}_i \times 10^4$	1.25	2.5	5.0	10.	0.125	0.25	0.5	1.0
$\hat{\tau}_{ii} \times 10^2$	2.0	4.0	8.0	16.	0.2	0.4	0.8	1.6
$\hat{\lambda}_{ii} \times 10^3$	4.5	8.9	18.	36.	4.5	8.9	18.	36.
$\hat{\varpi}_i \times 10^2$	0.45	0.89	1.8	3.6	0.45	0.89	1.8	3.6

Note again that the viscosity (and collision time or mean free path) is lower for the case with lower Larmor radius so that the variation of ϖ_α is the same between cases 1.X and 2.X. For the parameter sets in Table 6.2, we expect that the EM shocks will in general be significantly more diffusive relative to the ideal/inviscid shocks in Section 6.2, with more diffusion apparent for the case of $\hat{r}_L = 10^0$ than $\hat{r}_L = 10^{-1}$.

6.5.2 Parametric Study Results

Figures 6.14 and 6.15 depict the TFPGKS shock solutions in the present study compared to the ideal (inviscid) shock solution.
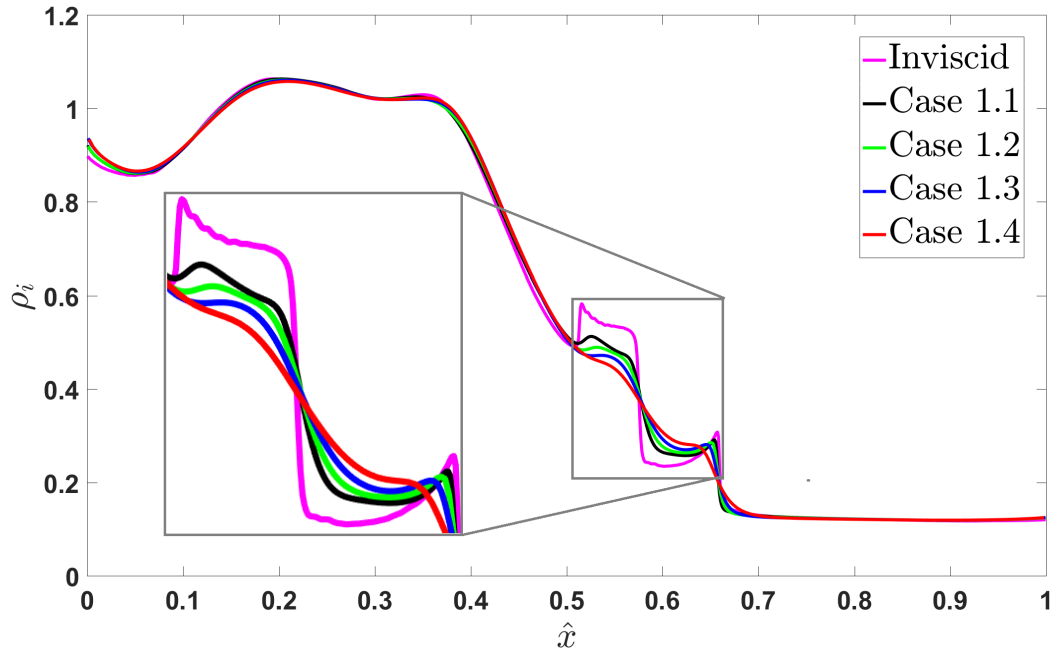
Figure 6.14: Electromagnetic shock, ion density for $\hat{r}_L = 10^0$, ideal shock solution compared to collisional shocks
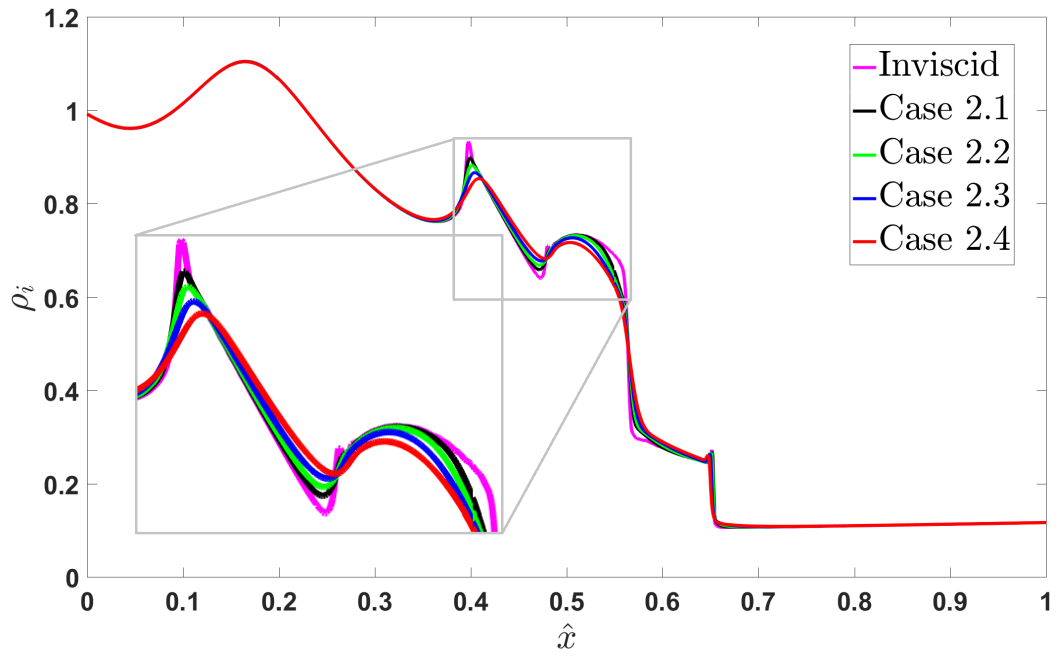
Figure 6.15: Electromagnetic shock, ion density for $\hat{r}_L = 10^{-1}$, ideal shock solution compared to collisional shocks

The increased diffusion is apparent by the smoothing of the shocks, especially for the case with $\hat{r}_L = 10^0$ where a larger collision time is used to achieve the same Hall parameter. In particular the shock structure of the $\hat{r}_L = 10^0$ shock around $\hat{x} = 0.5$ and $\hat{x} = 0.6$ – shown in the enlarged inset – has completely collapsed for the largest value of τ_{ii} and τ_{ee}. The enlarged inset for $\hat{r}_L = 10^{-1}$ in Figure 6.15 shows that the shock structure has not degraded nearly as much as for the $\hat{r}_L = 10^0$ case. This is because of the significantly smaller dissipation due to smaller τ_{ii} and τ_{ee}. Because of the difference in characteristic speeds between ions and electrons for this problem – $v_{th,e}/v_{th,i} \approx \sqrt{M}$ – we will show results for the ions at the full computational time $\hat{t}_{fin} = 0.1$ and for electrons at $\hat{t}_e \sim \hat{t}_{fin}M^{-1/2}$ the computational time. A mass ratio of $M = 1836$ will give $t_e \sim t_{fin}/40 = 0.0025$.

6.5.3 Larmor Radius of 10^0

First we will present the results for the $\hat{r}_L = 10^0$ shock. Figures 6.16 and 6.17 show the variation of the effective Hall parameter (red), mean free path (solid blue) and Larmor radius (dashed blue) along the direction of shock propagation for the case of largest collision time (case 1.4: $\hat{\tau}_{ii} = 0.16$, $\hat{\tau}_{ee} = 0.0037$). If we recall the analysis in Section 6.1 of
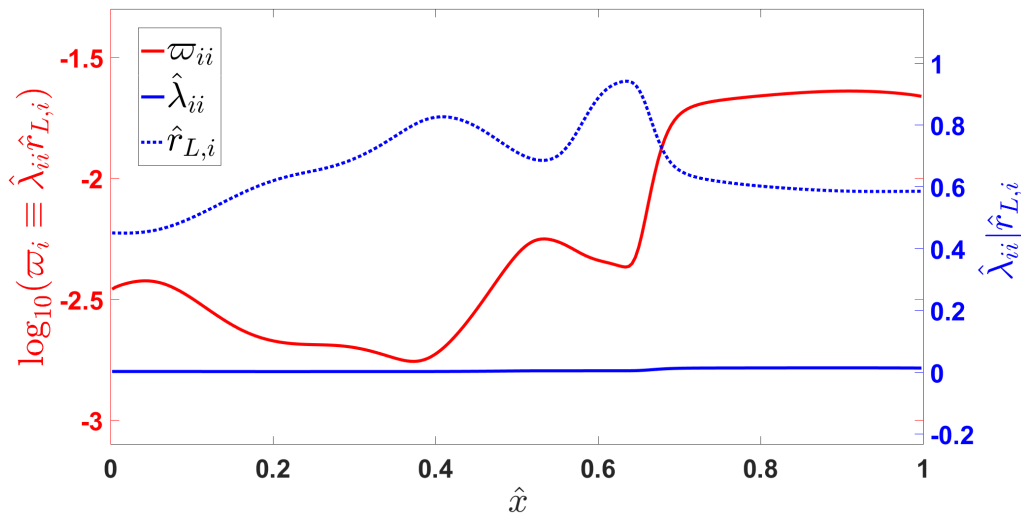
Figure 6.16: Effective electron Hall parameter, mean free path, and Larmor radius along $\hat{x}$ at $\hat{t} = 0.1$ for $\hat{r}_L = 10^0$
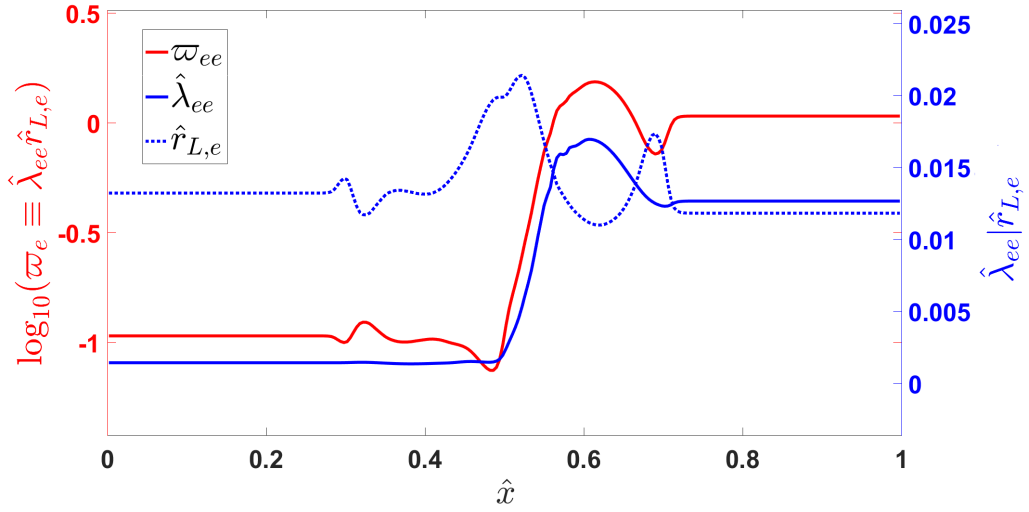
Figure 6.17: Effective ion Hall parameter, mean free path, and Larmor radius along $\hat{x}$ at $\hat{t} = 0.0025$ for $\hat{r}_L = 10^0$

the magnetized stress and heat flux we saw in figures 6.1 and 6.2 that for $\varpi < 10^{-1}$ we should not expect to see significant deviation from the "Uncoupled" scheme. From Figure 6.16 we can clearly see that the ion Hall parameter is never larger than $\sim 10^{-1.6}$, and thus it is unlikely that we will see significant differences between the Coupled and Uncoupled TFPGKS schemes for the ions in this set of simulations. In Figure 6.17 we see that the electrons Hall parameter is appreciably larger than 10^{-1} for $x > 0.5$, thus we expect some differences will be apparent in this region for the electrons.

In addition to the Hall parameter ϖ, the directionality of the magnetic field is also important. The action of the magnetic field will be to impede transport perpendicular to itself but not along it. Thus, since the problem is one-dimensional along x – all gradients are limited to $\frac{\partial}{\partial x}$ – the component of the magnetic field perpendicular to x is of particular interest. Figure 6.18 depicts the variation of the components of the normalized magnetic field parallel (b_x) and perpendicular ($\sqrt{b_y^2 + b_z^2}$) to the shock-tube. We can clearly see that apart from a small region near $\hat{x} \approx 0.69$ the perpendicular component of the magnetic field is of the same order of magnitude – or larger than – the parallel component. Thus, if ϖ is large enough

96
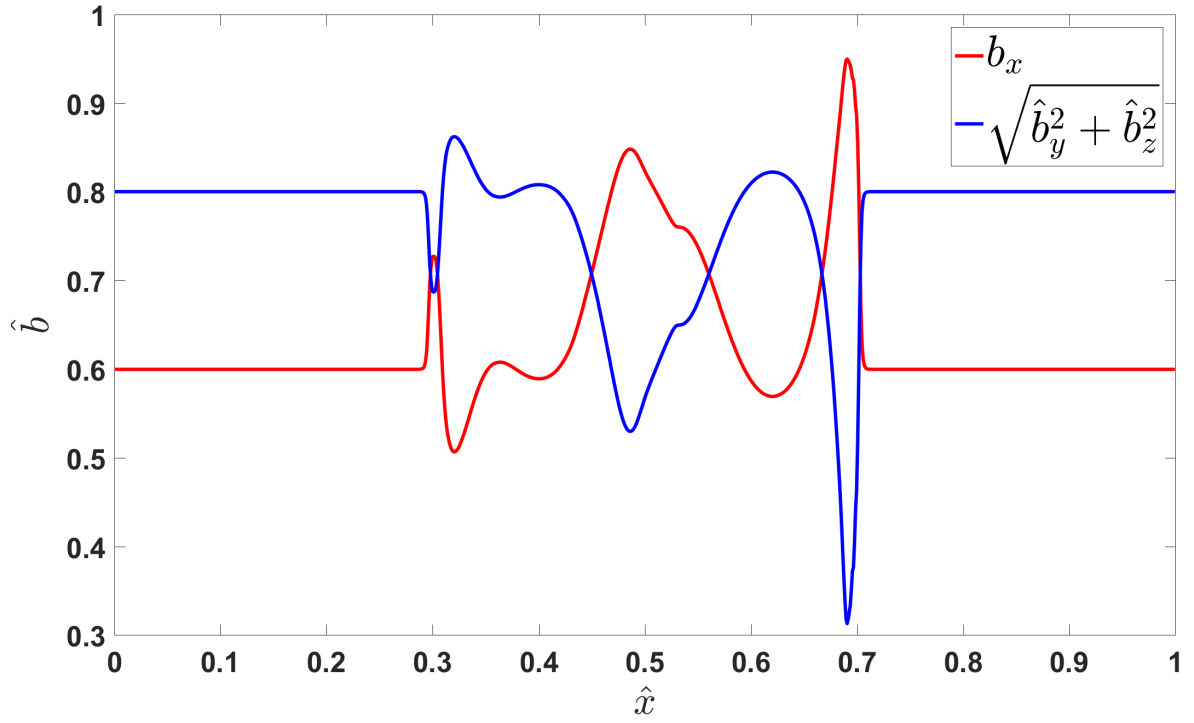
Figure 6.18: Normalized magnetic field along $\hat{x}$ at $\hat{t} = 0.0025$, components parallel and perpendicular to x-axis

we may expect to see variations in the collisional transport behavior at any point along the shock-tube.
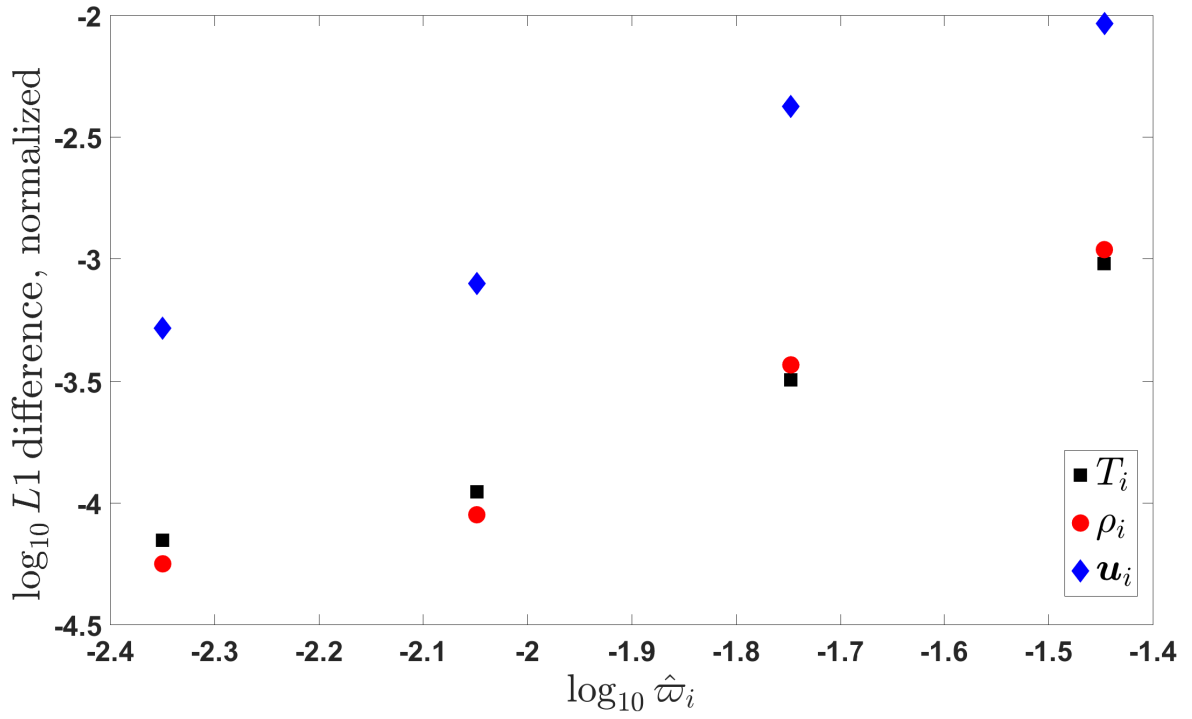
Figure 6.19: L_1 difference for ions vs. $\hat{\varpi}_i$ at $\hat{t} = 0.1$, $\hat{r}_L = 10^0$
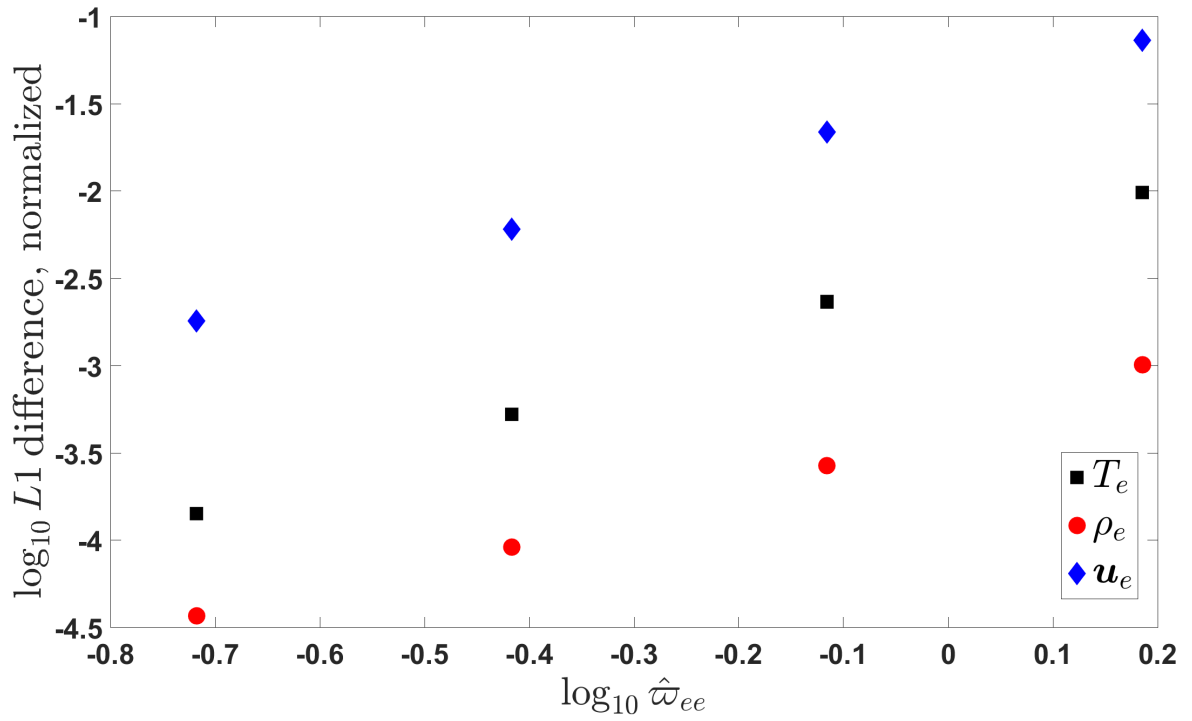
Figure 6.20: L_1 difference for electrons vs. $\hat{\varpi}_e$ at $\hat{t} = 0.0025$, $\hat{r}_L = 10^0$

Figures 6.19 and 6.20 depict the normalized L_1 difference of the Uncoupled TFPGKS scheme relative to the Coupled scheme, which is calculated by equation (6.30):

$$L1(T_e) = \frac{\sum_{j=1}^{N} |T_{e,C} - T_{e,U}|}{\sum_{j=1}^{N} T_{e,C}}.$$

(6.30)

In equation (6.30) the summation is done over all the cells in the domain. Here we distinguish between the Coupled and Uncoupled solutions by the subscripts C and U, respectively. For both, the difference increases with ϖ because the solution becomes more affected by physical effects – i.e. magnetization – which are not captured by the Uncoupled scheme. We can see in Figure 6.19 that the differences are not very significant, with the L_1 difference below 1% even for the largest value of $\hat{\varpi}_i$. For the electrons, however, we can see that the aggregate difference is approximately 8% for the largest value of $\hat{\varpi}_e$. In the remaining figures we will specifically look at the physical quantities for the electrons, ρ_e, $\boldsymbol{u}_e$, and T_e.
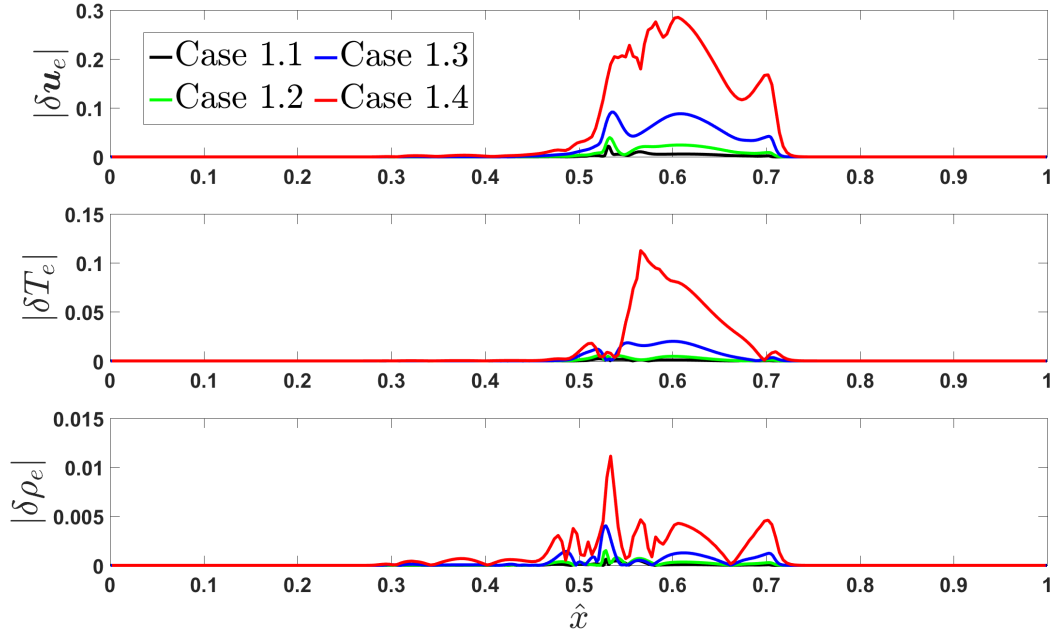
Figure 6.21: Relative difference in the solutions of velocity magnitude, temperature, and density for the electrons along the shock-tube: $\hat{r}_L = 10^0$

99

Figure 6.21 depicts the normalized relative difference in the solution along x for ρ_e, $\boldsymbol{u}_e$, and T_e, which is defined by equation (6.31).

$$\delta|\boldsymbol{u}| \equiv \frac{|\boldsymbol{u}_{e,C} - \boldsymbol{u}_{e,U}|}{\sqrt{\frac{1}{N}\sum_{j=1}^{N}|\boldsymbol{u}_{e,C}|^2}} \tag{6.31}$$

For case 1.4 – the red line, $\hat{\varpi}_e = 1.5$ – it can be clearly seen that there is a difference in the Coupled and Uncoupled solutions for the electron velocity magnitude, temperature, and density in the shock region for $0.5 \lesssim x \lesssim 0.7$. The difference increases from the black line (case 1.1) to the red line (case 1.4). In Figure 6.21 we can clearly see that the most significant differences between the Uncoupled and Coupled scheme are in the electron velocity and temperature, while the effect on the density is much less significant. This is generally what we would expect, as the non-equilibrium collisional effects have direct contributions to the evolution of the temperature and velocity via the heat flux and viscous transport. The effects on the density evolution are secondary rather than direct.

In Figure 6.22 we see the electron density, velocity magnitude, and temperature plotted along the shock-tube for cases 1.1 (black) and 1.4 (red) – these correspond to $\hat{\varpi}_e = 0.19$ and $\hat{\varpi}_e = 1.5$, respectively. The solid lines are the Coupled TFPGKS solution and the dashed lines depict the Uncoupled solution. While there is no visible difference for case 1.1 (black) for any of the variables, between $0.5 < \hat{x} < 0.7$ there are clear differences in $|\boldsymbol{u}_e|$ and T_e for case 1.4 (red). Figure 6.23 shows a zoomed version of Figure 6.22 between $0.45 < \hat{x} < 0.75$ for the velocity magnitude and temperature. It appears that the primary cause of difference is that the Uncoupled scheme overestimates the degree of collisional diffusion and transport in the regions of large Hall parameter. While the both the Coupled and Uncoupled TFPGKS solutions are more diffuse in the case with larger collision time, the Coupled scheme predicts that the diffusiveness due to collisional transport will be less. This is what we would expect on physical grounds due to the action of the magnetic field.
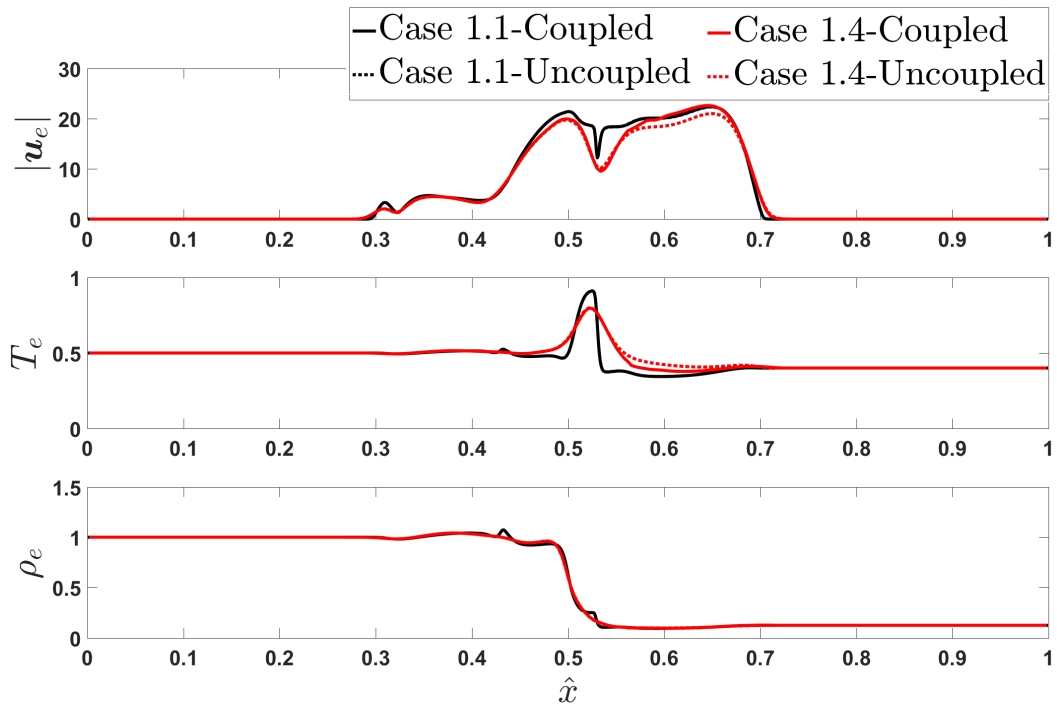
Figure 6.22: Comparison of solution for ρ_e, $\boldsymbol{u}_e$, and T_e along $\hat{x}$ at $\hat{t} = 0.0025$. Coupled (solid) and Uncoupled (dashed) TFPGKS for cases 1.1 (black) and 1.4 (red)
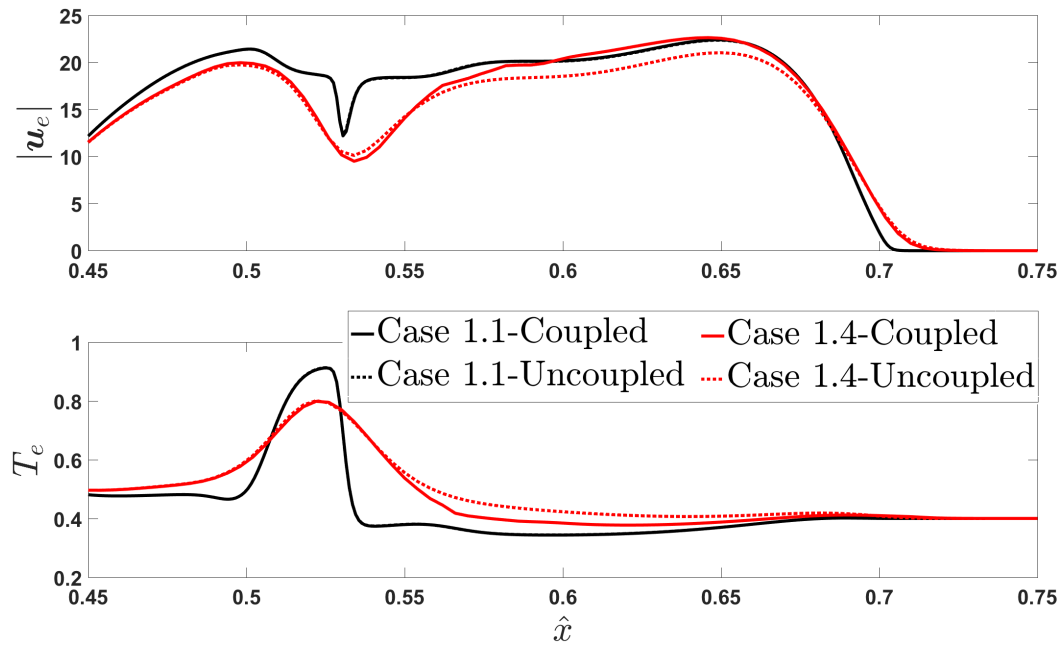
Figure 6.23: Comparison of solution for $\boldsymbol{u}_e$ and T_e zoomed to $0.45 < \hat{x} < 0.75$ at $\hat{t} = 0.0025$. Coupled (solid) and Uncoupled (dashed) TFPGKS for cases 1.1 (black) and 1.4 (red)

6.5.4 Larmor Radius of 10^{-1}

Next we present the results for the $\hat{r}_L = 10^{-1}$ shock from cases 2.1-2.4.
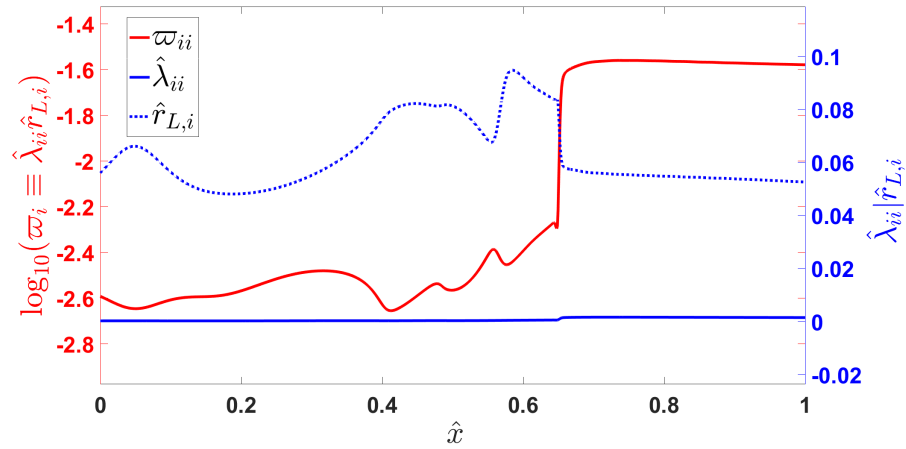
Figure 6.24: Effective electron Hall parameter, mean free path, and Larmor radius along $\hat{x}$ at $\hat{t} = 0.1$ for $\hat{r}_L = 10^{-1}$
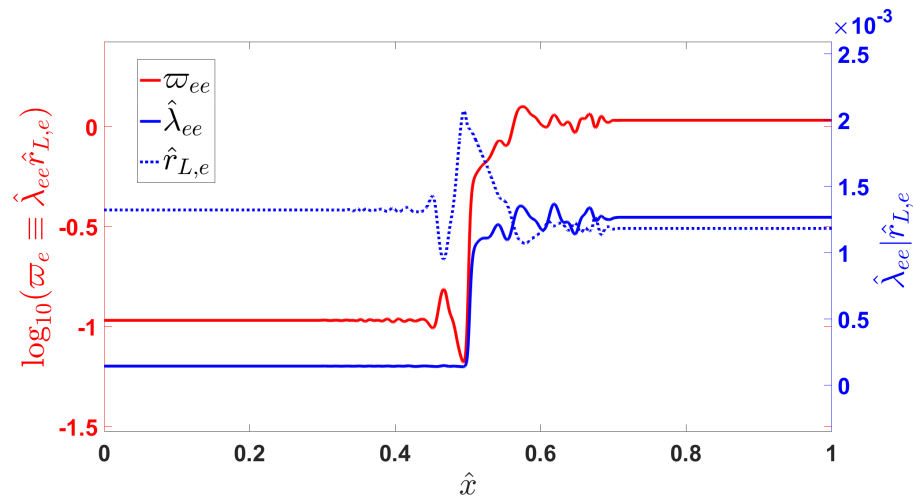
Figure 6.25: Effective ion Hall parameter, mean free path, and Larmor radius along $\hat{x}$ at $\hat{t} = 0.0025$ for $\hat{r}_L = 10^{-1}$

Recall from Table 6.2 that the approximate ion and electron Hall parameters for cases 2.X are the same as for the cases 1.X for the $\hat{r}_L = 10^0$ shock, but that the species collision times are proportionally smaller. Figures 6.24 and 6.25 show the variation of the effective Hall parameter (red), mean free path (solid blue) and Larmor radius (dashed blue) along the direction of shock propagation for the case of largest collision time (case 2.4: $\hat{\tau}_{ii} = 0.016$, $\hat{\tau}_{ee} = 0.00037$). From Figure 6.24 we can again clearly see that at its largest the ion Hall parameter is approximately $\varpi_i \approx 10^{-1.6}$, and thus it is unlikely that we will see significant differences between the Coupled and Uncoupled TFPGKS schemes for the ions in this set of simulations. In Figure 6.25 we see that the electrons Hall parameter is appreciably larger than 10^{-1} for $x > 0.5$, thus we expect some differences will be apparent in this region for the electrons.
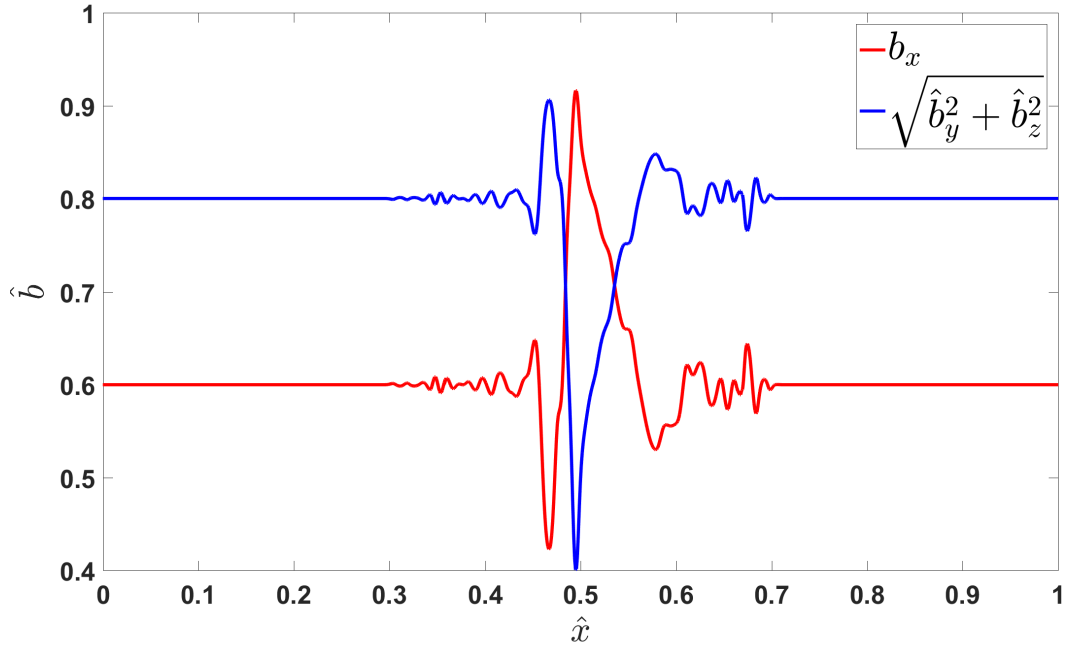
Figure 6.26: Normalized magnetic field along $\hat{x}$ at $\hat{t} = 0.0025$, components parallel and perpendicular to x-axis

We again investigate the directionality of the normalized magnetic field in Figure 6.26 which depicts the variation of the components of the magnetic field parallel (b_x) and perpendicular ($\sqrt{b_y^2 + b_z^2}$) to the shock-tube. Again it is clear that the component of the magnetic field perpendicular to the flow gradients is greater than the parallel component throughout the majority of the shock-tube. The notable exception is in the vicinity of $\hat{x} = 0.5$, where b_x and $\sqrt{b_y^2 + b_z^2}$ switch briefly when b_y passes through zero from $+1$ at $x < 0.5$ to -1 at $x \geq 0.5$.
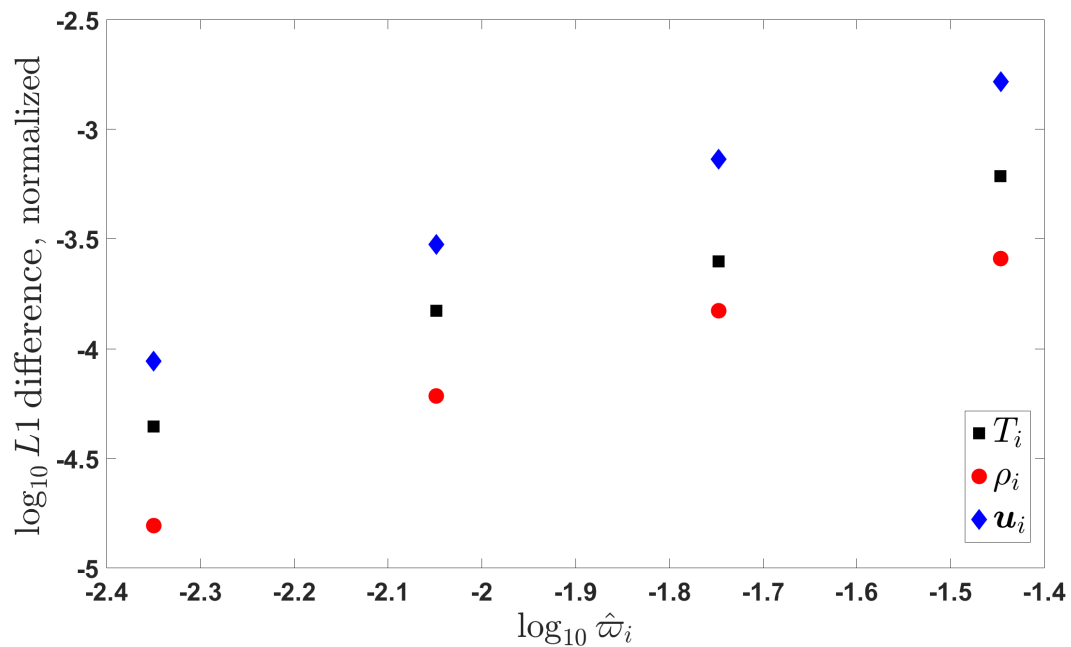
Figure 6.27: L_1 difference for ions vs. $\hat{\varpi}_i$ at $\hat{t} = 0.1$, $\hat{r}_L = 10^{-1}$

Figures 6.27 and 6.28 depict the normalized L_1 difference for cases 2.1-2.4, which is again calculated by equation (6.30). We can see again in Figure 6.27 that the difference in the ion solution for this case is not very significant, with the L_1 difference below 1% even for the largest value of $\hat{\varpi}_i$. For the electrons, however, we can again see that the aggregate difference is significantly larger, approaching $\sim 12\%$ for the largest value of $\hat{\varpi}_e$ in this case.
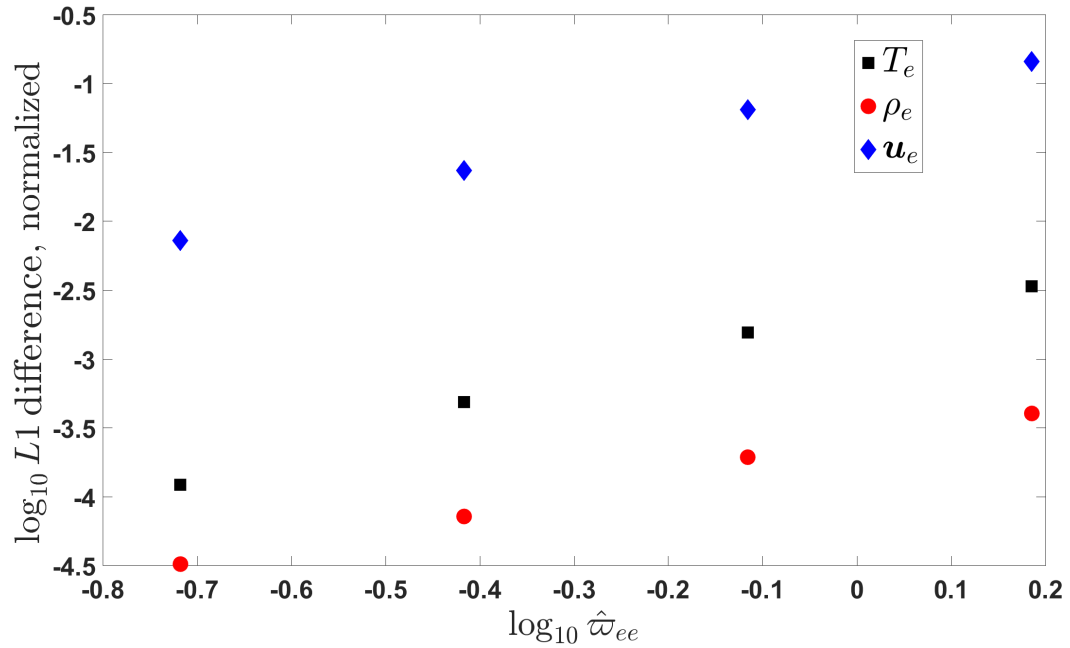
Figure 6.28: L_1 difference for electrons vs. $\hat{\varpi}_e$ at $\hat{t} = 0.0025$, $\hat{r}_L = 10^{-1}$

Figure 6.29 depicts the relative difference in the solution along x for ρ_e, $\boldsymbol{u}_e$, and T_e, which is again defined by equation (6.31). For case 2.4 – the red line, $\hat{\varpi}_e = 1.5$ – the difference is again much more pronounced for the velocity and temperature – with local normalized relative difference of > 0.5 and > 0.05, respectively – than for the density, and is confined to $0.5 < \hat{x} < 0.7$.
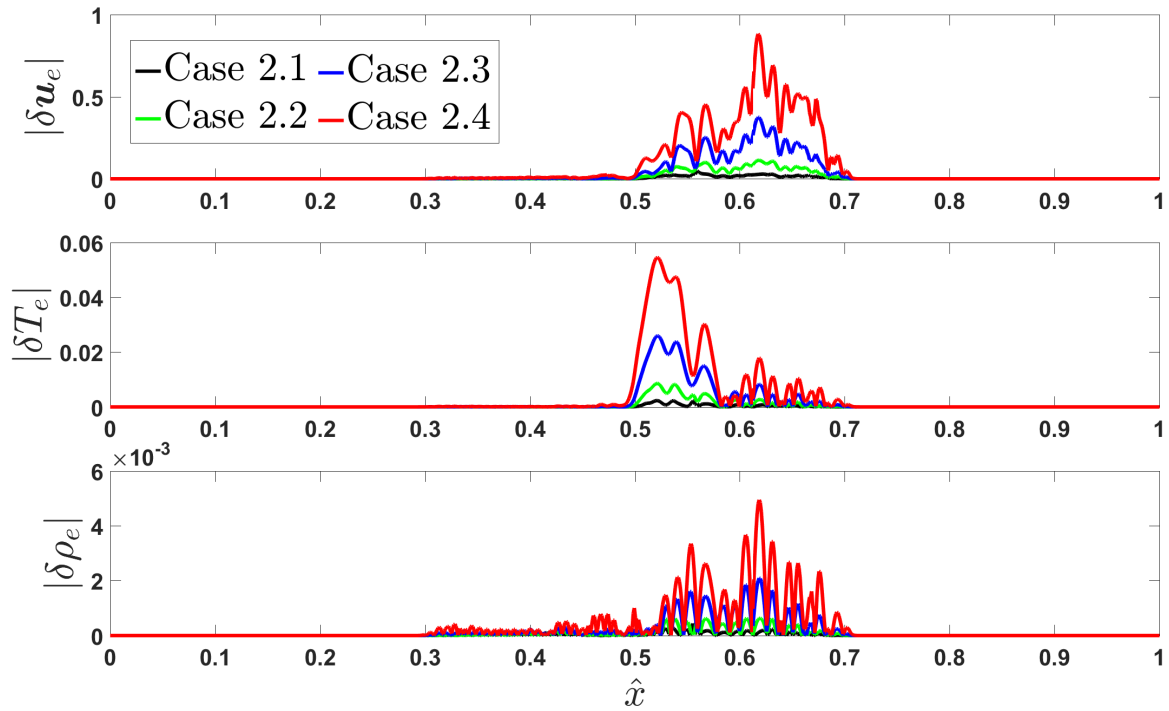
Figure 6.29: Relative difference in the solutions of velocity magnitude, temperature, and density for the electrons along the shock-tube: $\hat{r}_L = 10^{-1}$
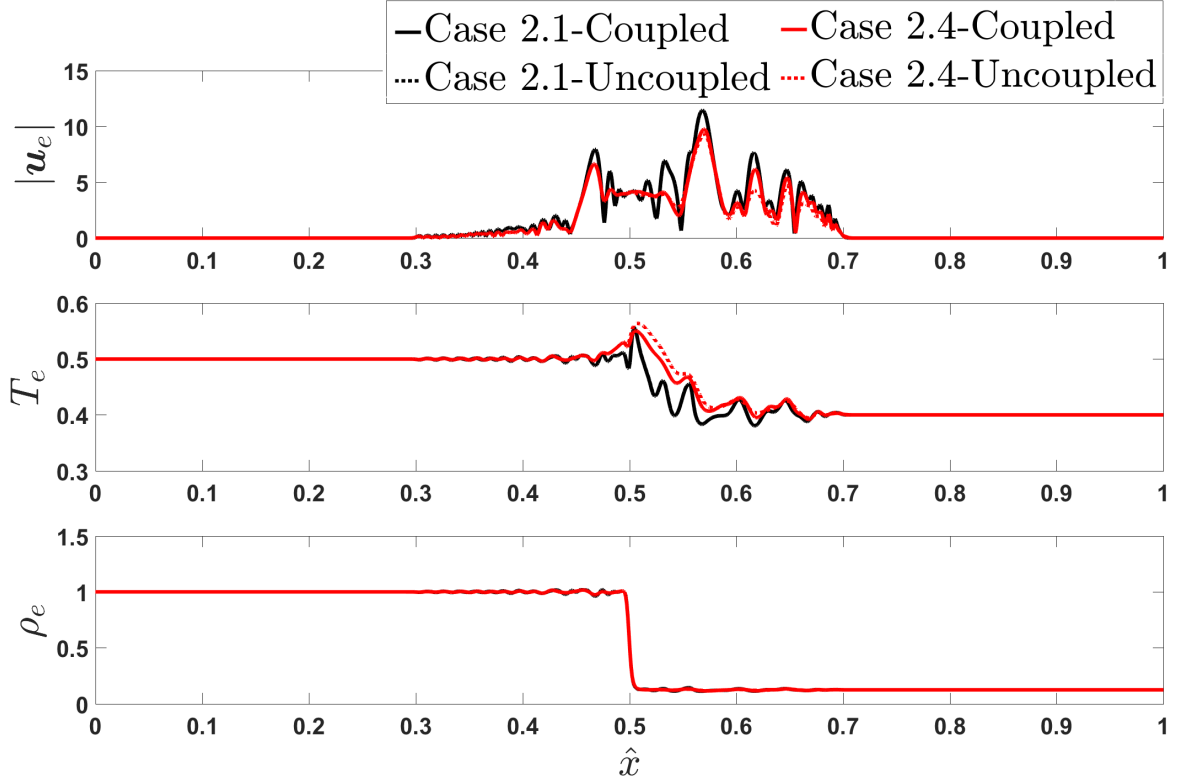
Figure 6.30: Comparison of solution for ρ_e, $\boldsymbol{u}_e$, and T_e along $\hat{x}$ at $\hat{t} = 0.0025$. Coupled (solid) and Uncoupled (dashed) TFPGKS for cases 2.1 (black) and 2.4 (red)

In Figure 6.30 we see the electron density, velocity magnitude, and temperature plotted along the shock-tube for cases 2.1 (black) and 2.4 (red). The solid lines are the Coupled TF-PGKS solution and the dashed lines depict the Uncoupled solution. While there is no visible difference for case 2.1, between $0.5 < \hat{x} < 0.7$ there are again clearly visible differences for $|\boldsymbol{u}_e|$ and T_e. Figure 6.31 shows a zoomed version of Figure 6.30 between $0.45 < \hat{x} < 0.75$ for the velocity magnitude and temperature. Relative to figures 6.22 and 6.23 for $\hat{r}_L = 10^0$, figures 6.30 and 6.31 for $\hat{r}_L = 10^{-1}$ exhibit much more dispersive, oscillatory behavior. This is due to the smaller Larmor radius and Debye Length in the $\hat{r}_L = 10^{-1}$ case, which increases the naturally dispersive behavior of the governing equations of the two-fluid plasma system [57]. Additionally we can see that the magnitude of the electron velocity for $\hat{r}_L = 10^{-1}$ is significantly lower than for $\hat{r}_L = 10^0$, which is primarily due to the electrons being "bound"
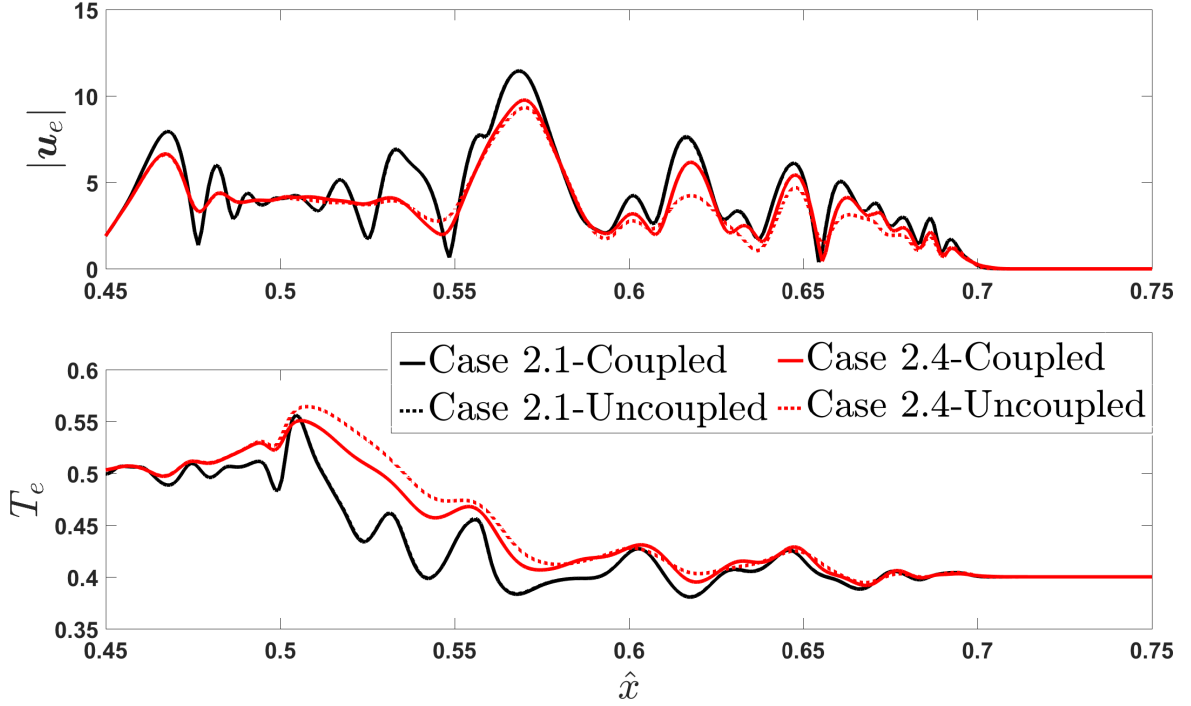
Figure 6.31: Comparison of solution for $\boldsymbol{u}_e$ and T_e zoomed to $0.45 < \hat{x} < 0.75$ at $\hat{t} = 0.0025$. Coupled (solid) and Uncoupled (dashed) TFPGKS for cases 2.1 (black) and 2.4 (red)

more tightly by the electric field (which is parametrically due to the smaller Deybe length in this case). Again, the source of the differences for the Uncoupled scheme are that it overestimates diffusivity in the regions of large ϖ. Recall that the Coupled scheme both includes the electromagnetic forces in the TFPGKS flux evolution and the effects of magnetization on the non-equilibrium distribution, while the Uncoupled scheme does not. Thus, the Uncoupled scheme does not capture the same physical effects at large Hall parameter ϖ. This is particularly noticeable around $\hat{x} = 0.63$ and $\hat{x} = 0.68$ for the electron velocity. Further, the degree of "pre-shock heating" – visible in T_e as the area of increased temperature immediately to the right of $\hat{x} = 0.5$ – is greater for increased collision time and mean free path, but is overestimated by the Uncoupled TFPGKS scheme which does not account for the effect of the magnetization in limiting the cross-field transport, thereby reducing the effective collision time perpendicular to $\boldsymbol{B}$.

6.6 Conclusions

In this Chapter we perform numerical simulations using the Two-Fluid Plasma TFPGKS (TFPGKS) method which exhibit its applicability in various parametric regimes. The zero-dimensional analysis of TFPGKS fluxes shows that the constitutive relationship for stress and heat flux of Woods [34] is recovered and differs only somewhat from the more physically accurate model of Braginskii [53]. This is primarily due to the difference between the Woods and Braginskii models. The results of the linearized analytic solution comparison together with the comparison to published computations of 1-D EM shocks and ion acoustic solitons demonstrate the validity of the TFPGKS proof-of-concept and numerical implementation. Finally, the improved capability of the new scheme over the previous naïve implementation regarding the effect of accelerations on the flux evolution is demonstrated in the parametric studies of collisional EM shocks.

7. SUMMARY AND CONCLUSIONS

7.1 Summary of Work

The objective of this dissertation is to develop the theoretical framework for computational study of plasma flows using the gas-kinetic scheme. An overview of the advantages of the Gas-Kinetic Scheme (GKS) relative to other continuum and near-continuum approaches is discussed. The motivation for extending GKS to plasma flows is explained. The theoretical framework towards a coupled GKS approach for a two-fluid plasma of electrons and singly-charged positive ions is presented and termed the Two Fluid Plasma Gas-Kinetic Scheme (TFPGKS). In this development a Method-of-Characteristics type approach is taken to obtain a solution to the Boltzmann equation for each species (singly-charged positive ions and electrons) using the BGK collision operator. The Perfectly Hyperbolic Maxwell's (PHM) equations [46, 47, 48] are used to integrate the electromagnetic fields and mitigate errors in the divergence constraints of Gauss's law for the electric and magnetic fields.

A "first-order" verification of the approach is performed by implementing the TFPGKS flux in isolation using Mathematica. In this approach the effects of magnetization on the heat flux and stress tensor are analyzed and compared to the transport models of Woods [34] and Braginksii [53]. The results indicated that the TFPGKS flux agreed exactly with the model of Woods, as expected for the purely smooth zero-dimensional case, and agreed reasonably well with Braginskii's transport model. This is because both the Woods transport model and the TFPGKS flux are based on the BGK collision operator, while Braginskii's approach uses the more rigorous – albeit more complicated – Fokker-Planck-Landau collision operator.

A one-dimensional version of the scheme is implemented to further validate the theory and demonstrate the proof-of-concept. The TFPGKS is benchmarked against a variety of zero- and one-dimensional problems to verify the numerical implementation and to ensure that appropriate asymptotic limits are preserved. To assist the validation process, a linearized

version of the governing equations is derived and an analytic solution is obtained. The TF-PGKS scheme performed well in the benchmark against the linearized solutions, exhibiting only a small accumulation of nonlinear "drift" away from the linearized solutions after nearly 40 periods of the longest waveform. In addition, the TFPGKS scheme is benchmarked against published computational data for the two-fluid electromagnetic shock – a generalization of Brio and Wu's shock [52] – as well as solutions of ion acoustic solitons [54]. In all cases, the TFPGKS scheme agreed very well with published data, verifying that the scheme performs as expected and recovers appropriate two-fluid solutions in the asymptotic limit of vanishing electron and ion self-collision times τ_{ee} and τ_{ii}.

A basic set of parametric studies is also performed to asses the behavior of the scheme in the collisional regime – ie, with finite $\tau_{\alpha\alpha}$. The electromagnetic shocks for $\hat{r}_L = 10^0$ and $\hat{r}_L = 10^{-1}$ are simulated for a range of collision times, maintaining $\tau_{ii} = \sqrt{M}\tau_{ee}$ [36, 60, 31]. Comparison is made to a previously developed "Uncoupled" version of the TFPGKS scheme which neglected the effects of the electromagnetic fields on the TFPGKS flux calculations [21]. Overall as τ_{ii} and τ_{ee} are increased the shock solutions become significantly more diffuse, to the point that the shock structures collapse almost entirely for the largest values of τ. For the cases with largest τ and correspondingly largest Hall parameter $\varpi \equiv \tau\omega_c$ – cases 1.4 and 2.4 – the Uncoupled scheme exhibits significant differences relative to the Coupled scheme for the electrons – as much as 12% – while the differences for the ions are relatively insignificant – less than 1% at the most. The reason for the large disparity between the electrons and ions is due to the mass ratio ($M = 1836$) which causes a correspondingly large disparity in the species' Hall parameters ϖ_e and ϖ_i.

7.2 Recommendations for Future Work

7.2.1 General Improvements

First, the existing scheme will be extended to two- and three-dimensional implementation, which would allow a much wider array of interesting problems and relevant physics to

be studied. In addition, we suggest in no particular order a number of improvements which would improve both its numerical characteristics and applicability to an extended range of problems.

1. Implementation on axisymmetric or other non-cartesian grids would also allow more interesting problems to be studied. There are possible cylindrical modifications which may not require the Gas-Kinetic scheme itself to be significantly modified – see e.g., Chapter 4 of Srinivasan [61].

2. To reduce the computational burden due to disparate timescales between the electromagnetic fields, electrons, and ions, a sub-cycling scheme which "nests" iterations of the faster components within those of slower components could be implemented [62]. This approach has been used for the previously developed MHD-GKM scheme of Araya et al. [21] for sub-cycling the Hall term in the magnetic field evolution. In mitigating the stiffness of the Hall physics this approach has shown itself capable of reducing computational time by up to an order of magnitude [62, 63].

3. Amano [64] developed a "quasi-neutral two-fluid" scheme which retains electrons inertial effects while avoiding issues of timescales related to the plasma frequency. A similar approach could be applied to TFPGKS, as the primary difference is in the solution of the electromagnetic fields. The benefit of this approach would be to improve numerical efficiency by removing high frequency Langmuir oscillations which generally do not contribute significantly to the macroscopic system dynamics [64].

7.2.2 GKS Improvements

For the gas-kinetic scheme itself, there are a variety of improvements which may be helpful in improving the scheme's applicability for a wide range of problems.

1. The Unified Gas Kinetic Scheme (UGKS) is an approach to implementing GKS which employs a discretized velocity space [22, 65]. This allows the scheme to be applied to flows at a much larger Knudsen number than the current approach.

2. Extension of the BGK-based scheme to higher fidelity via Burnett or Super-Burnett expansion has been done for other GKS implementations and could be useful to extended the validity of the current scheme for higher Knudsen numbers [66, 67]. Another possibility would be to use a "regularization" of the BGK collision operator wherein the collision time τ is generalized to depend on both the macroscopic variables and their gradients in the rarefied regime [68, 69]. These approaches allow the scheme to be applied to higher Knudsen number flows without requiring discretization of the velocity space as in the UGKS approach.

3. In the development from equation (3.57), it is assumed that variations in U_β, E, and B can be neglected in the characteristic solution for $f(t)$. A more rigorous derivation and implementation would include Taylor expansions for these quantities as well.

4. Extension of the present approach to allow for anisotropic pressure and temperature – i.e. higher moments – would be useful for a variety of applications with highly magnetized plasmas. GKS implementations have been done for multiple temperatures – translational, vibrational, and rotational [70, 71] – and could be extended to the anisotropy due to strong magnetization.

5. Implementation of a more sophisticated collisional model than the BGK approach would also allow for a more accurate capturing of the transport properties. As seen in Section 6.1, the BGK model does not quite follow the more accurate transport model derived by Braginskii from the Fokker-Planck-Landau collision operator. UGKS implementations have been done with the full Boltzmann collision model [23].

6. For highly magnetized applications such as Tokamaks, gyro-kinetic and gyro-fluid type approaches have been employed [72, 73]. It may be possible to extend gyro-averaging theory to the GKS equations.

7. For multi-species plasmas, it would be straightforward to add as many ion or neu-

tral species as desired, using GKS to calculate the fluxes for each species. Further, GKS has been previously applied to chemically reacting flows [17], and thus could be extended to flows with ionization and recombination of species.

REFERENCES

[1] D. B. Araya, "Resistive MHD simulations of laminar round jets with application to magnetic nozzle flows," Master's Thesis, Texas A&M University, 2011.

[2] U. Shumlak and J. Loverich, "Approximate Riemann solver for the two-fluid plasma model," *J. Comput. Phys.*, vol. 187, no. 2, pp. 620–638, 2003.

[3] R. Abgrall and H. Kumar, "Robust finite volume schemes for two-fluid plasma equations," *J. Sci. Comput.*, vol. 60, no. 3, pp. 584–611, 2014.

[4] A. Hakim, J. Loverich, and U. Shumlak, "A high resolution wave propagation scheme for ideal two-fluid plasma equations," *J. Comput. Phys.*, vol. 219, no. 1, pp. 418–442, 2006.

[5] J. Loverich, A. Hakim, and U. Shumlak, "A discontinuous galerkin method for ideal two-fluid plasma equations," *Commun. Comput. Phys.*, vol. 9, no. 2, pp. 240–268, 2011.

[6] H. Kumar and S. Mishra, "Entropy stable numerical schemes for two-fluid plasma equations," *J. Sci. Comput.*, vol. 52, no. 2, pp. 401–425, 2012.

[7] F. R. Chang-Díaz, "The VASIMR rocket," *Sci. Am.*, vol. 283, no. 5, pp. 90–97, 2000.

[8] E. A. Bering, B. W. Longmier, M. Ballenger, C. S. Olsen, J. P. Squire, and F. R. Chang-Díaz, "Performance studies of the VASIMR ® VX-200," in *49th AIAA Aerosp. Sci. Meet.*, January 2011, pp. 4–7.

[9] J. D. Huba, *NRL plasma formulary*, 2013. [Online]. Available: http://wwwppd.nrl.navy.mil/nrlformulary/

[10] G. Kumar, "Modal analysis of instability, turbulence and novel control strategies in high mach number shear flows," PhD Dissertation, Texas A&M University, 2012.

[11] G. Kumar, S. S. Girimaji, and J. Kerimo, "WENO-enhanced gas-kinetic scheme for direct simulations of compressible transition and turbulence," *J. Comput. Phys.*, vol. 234, no. 1, pp. 499–523, 2013. [Online]. Available: http://dx.doi.org/10.1016/j.jcp.2012.10.005

[12] K. Xu, "A gas-kinetic BGK scheme for the Navier-Stokes equations and its connection with artificial dissipation and Godunov method," *J. Comput. Phys.*, vol. 171, no. 1, pp. 289–335, 2001. [Online]. Available: http://www.sciencedirect.com/science/article/pii/ S0021999101967907

[13] ——, "Gas-kinetic schemes for unsteady compressible flow simulations," in *von Karman Inst. Fluid Dyn. Lect. Ser. 29th Comput. Fluid Dyn.*, 1998.

[14] M. Su, K. Xu, and M. Ghidaoui, "Low-speed flow simulation by the gas-kinetic scheme," *J. Comput. Phys.*, vol. 150, no. 1, pp. 17–39, 1999. [Online]. Available: http://www.sciencedirect.com/science/article/pii/S0021999198961629

[15] K. Xu, "BGK-based scheme for multicomponent flow calculations," *J. Comput. Phys.*, vol. 134, no. 1, pp. 122–133, 1997. [Online]. Available: http://www.sciencedirect. com/science/article/pii/S0021999197956771

[16] L. Pan, G. Zhao, B. Tian, and S. Wang, "A gas kinetic scheme for the simulation of compressible multicomponent flows," *Commun. Comput. Phys.*, vol. 14, no. 5, pp. 1347–1371, 2013.

[17] Y. Lian and K. Xu, "A gas-kinetic scheme for multimaterial flows and its application in chemical reaction," NASA Langley - ICASE, Hampton, Virginia, U.S.A., Tech. Rep., 1999.

[18] K. Xu, "Gas-kinetic theory based flux splitting method for ideal magnetohydrodynamics," *J. Comput. Phys.*, vol. 352, pp. 334–352, 1998.

[19] H.-Z. Tang and K. Xu, "A high-order gas-kinetic method for multidimensional ideal magnetohydrodynamics," *J. Comput. Phys.*, vol. 165, no. 1, pp. 69–88, 2000. [Online]. Available: http://linkinghub.elsevier.com/retrieve/pii/S0021999100965975

[20] H.-Z. Tang, K. Xu, and C. Cai, "Gas-kinetic BGK scheme for three dimensional magnetohydrodynamics," *Numer. Math. Theory, Methods Appl.*, vol. 3, no. 4, pp. 387–404, 2010.

[21] D. B. Araya, F. H. Ebersohn, S. E. Anderson, and S. S. Girimaji, "Magneto-gas kinetic

method for nonideal magnetohydrodynamics flows: verification protocol and plasma jet simulations," *J. Fluids Eng.*, vol. 137, p. 081302, 2015.

[22] V. Venugopal and S. S. Girimaji, "Unified gas kinetic scheme and direct simulation Monte Carlo computations of high-speed lid-driven microcavity flows," *Commun. Comput. Phys.*, vol. 17, no. 05, pp. 1127–1150, 2015. [Online]. Available: http://www.journals.cambridge.org/abstract{_}S1815240615000365

[23] C. Liu, K. Xu, Q. Sun, and Q. Cai, "A unified gas-kinetic scheme for continuum and rarefied flows IV: full Boltzmann and model equations," *J. Comput. Phys.*, 2016. [Online]. Available: http://arxiv.org/abs/1405.4479

[24] S. Chen and K. Xu, "A comparative study of an asymptotic preserving scheme and unified gas-kinetic scheme in continuum flow limit," *J. Comput. Phys.*, vol. 288, pp. 52–65, may 2015.

[25] P. L. Bhatnagar, E. P. Gross, and M. Krook, "A model for collision processes in gases. I. Small amplitude processes in charged and neutral one-component systems," *Phys. Rev.*, vol. 94, no. 3, p. 511, 1954.

[26] M. A. Gallis and J. R. Torczynski, "A collective collision operator for DSMC," Sandia National Laboratories, Albuquerque, New Mexico, U.S.A., Tech. Rep. September 1, 2000.

[27] S. Livi and E. Marsch, "Comparison of the Bhatnagar-Gross-Krook approximation with the exact Coulomb collision operator," *Phys. Rev. A*, vol. 34, no. 1, pp. 533–540, 1986.

[28] R. Kumar, E. V. Titov, D. A. Levin, N. E. Gimelshein, and S. F. Gimelshein, "Assessment of Bhatnagar-Gross-Krook approaches for near continuum regime nozzle flows," *AIAA J.*, vol. 48, no. 7, pp. 1531–1541, 2010. [Online]. Available: http://arc.aiaa.org/doi/10.2514/1.J050208

[29] L. Mieussens and H. Struchtrup, "Numerical comparison of Bhatnagar-Gross-Krook models with proper Prandtl number," *Phys. Fluids*, vol. 16, no. 8, pp. 2797–2813, 2004.

[30] Q.-H. Sun, C.-P. Cai, and W. Gao, "On the validity of the Boltzmann-BGK model

through relaxation evaluation," *Acta Mech. Sin.*, vol. 30, no. 2, pp. 133–143, 2014.

[31] A. Sitenko and V. Malnev, *Plasma physics theory*. London: Chapman & Hall, 1995.

[32] K. Xu and K. H. Prendergast, "Numerical Navier-Stokes solutions from gas kinetic theory," vol. 114, no. 1, pp. 9–17, 1994. [Online]. Available: http://www.sciencedirect.com/science/article/pii/S0021999184711454

[33] K. H. Prendergast and K. Xu, "Numerical hydrodynamics from gas-kinetic theory," vol. 109, no. 1, pp. 53–66, 1993.

[34] L. C. Woods, *Principles of magnetoplasma dynamics*. Oxford: Oxford University Press, 1987.

[35] D. B. Araya, S. Girimaji, M. D. Carter, and C. S. Olsen, "Parameterization of magnetic nozzle flow physics for an in-space propulsion application," in *42nd AIAA Plasmadynamics Lasers Conf.*, pp. 1–13.

[36] R. Fitzpatrick, *Plasma physics: An introduction*. Boca Raton: CRC Press, Taylor & Francis, 2014.

[37] B. M. Riley, "Magnetohydrodynamic lattice boltzmann simulations of turbulence and rectangular jet flow," Master's Thesis, Texas A&M University, 2007.

[38] G. Breyiannis and D. Valougeorgis, "Lattice kinetic simulations in three-dimensional magnetohydrodynamics," *Phys. Rev. E - Stat. Nonlinear, Soft Matter Phys.*, vol. 69, no. 6 2, pp. 1–4, 2004.

[39] M. N. Kogan, *Rarefied gas dynamics*. New York: Springer Science+Business Media, 1969, vol. 1.

[40] X.-D. Liu, S. Osher, and T. Chan, "Weighted essentially non-oscillatory schemes," vol. 115, no. 1, pp. 200–212, 1994. [Online]. Available: http://linkinghub.elsevier.com/retrieve/pii/S0021999184711879

[41] G.-S. Jiang and C.-W. Shu, "Efficient implementation of weighted ENO schemes," *J. Comput. Phys.*, vol. 126, no. 1, pp. 202–228, 1996. [Online]. Available: http://linkinghub.elsevier.com/retrieve/pii/S0021999196901308

[42] J. U. Brackbill and D. C. Barnes, "The effect of nonzero div(B) on the numerical solution of the magnetohydrodynamic equations," *J. Comput. Phys.*, vol. 35, pp. 426–430, 1980.

[43] G. Toth, "The div(B)=0 constraint in shock-capturing magnetohydrodynamics codes," *J. Comput. Phys.*, vol. 161, pp. 605–652, 2000. [Online]. Available: http://www.sciencedirect.com/science/article/pii/S0021999100965197

[44] A. Dedner, F. Kemm, D. Kröner, C.-D. Munz, T. Schnitzer, and M. Wesenberg, "Hyperbolic divergence cleaning for the MHD equations," *J. Comput. Phys.*, vol. 175, no. 2, pp. 645–673, 2002. [Online]. Available: http://www.sciencedirect.com/science/article/pii/S002199910196961X

[45] D. Yu, F. Miniati, T. W. Jones, and A. Frank, "A divergence-free upwind code for multidimensional magnetohydrodynamic flows," *Astrophys. J.*, vol. 509, pp. 244–255, 1998.

[46] C.-D. Munz, P. Omnes, and R. Schneider, "A three-dimensional finite-volume solver for the Maxwell equations with divergence cleaning on unstructured meshes," *Comput. Phys. Commun.*, vol. 130, pp. 83–117, 2000.

[47] C.-D. Munz, R. Schneider, and U. Voß, "A finite volume method for the Maxwell equations in the time domain," *SIAM J. Sci. Comput.*, vol. 22, no. 2, pp. 449–475, 2000.

[48] C.-D. Munz, P. Omnes, R. Schneider, E. Sonnendrücker, and U. Voß, "Divergence correction techniques for Maxwell solvers based on a hyperbolic model," *J. Comput. Phys.*, vol. 161, no. 2, pp. 484–511, 2000. [Online]. Available: http://www.sciencedirect.com/science/article/pii/S0021999100965070

[49] H. C. Yee, "A class of high-resolution explicit and implicit shock-capturing methods," NASA Ames Research Center, Mountain View, California, U.S.A., Tech. Rep., 1989.

[50] R. J. LeVeque, *Finite-volume nethods for hyperbolic problems*. Cambridge: Cambridge University Press, 2004.

[51] G. Strang, "On the construction and comparison of difference schemes," *SIAM J. Numer. Anal.*, vol. 5, no. 3, pp. 506—-517, 1968.

[52] M. Brio and C. C. Wu, "An upwind differencing scheme for the equations of ideal magnetohydrodynamics," *J. Comput. Phys.*, vol. 75, no. 2, pp. 400–422, 1988. [Online]. Available: http://dx.doi.org/10.1016/0021-9991(88)90120-9

[53] S. I. Braginskii, "Transport processes in a plasma," in *Rev. Plasma Phys.*   Consultants Bureau, 1965, pp. 205–311.

[54] S. Baboolal, "Finite-difference modeling of solitons induced by a density hump in a plasma multi-fluid," *Math. Comput. Simul.*, vol. 55, no. 4-6, pp. 309–316, 2001.

[55] S. Baboolal and R. Bharuthram, "Two-scale numerical solution of the electromagnetic two-fluid plasma-Maxwell equations: Shock and soliton simulation," *Math. Comput. Simul.*, vol. 76, no. 1-3, pp. 3–7, 2007.

[56] S. Baboolal, "High-resolution numerical simulation of 2D nonlinear wave structures in electromagnetic fluids with absorbing boundary conditions," *J. Comput. Appl. Math.*, vol. 234, no. 6, pp. 1710–1716, 2010. [Online]. Available: http://dx.doi.org/10.1016/j.cam.2009.08.019

[57] B. Srinivasan, A. Hakim, and U. Shumlak, "Numerical methods for two-fluid dispersive fast MHD phenomena," *Commun. Comput. Phys.*, vol. 10, no. 1, pp. 183–215, 2011.

[58] D. B. Cohn and K. R. MacKenzie, "Density-step - excited ion acoustic solitons," *Phys. Rev. Lett.*, vol. 30, no. 7, pp. 258–261, 1973.

[59] D. J. Korteweg and G. de Vries, "On the change of form of long waves advancing in a rectangular canal, and on a new type of long stationary waves," *London, Edinburgh, Dublin Philos. Mag. J. Sci.*, vol. 39, no. 240, pp. 422–443, 1895.

[60] P. Helander and D. J. Sigmar, *Collisional transport in magnetized plasmas*.   Cambridge: Cambridge University Press, 2002.

[61] B. Srinivasan, "Numerical methods for 3-dimensional magnetic confinement configurations using two-fluid plasma equations," PhD Dissertation, University of Washington,

2010.

[62] J. D. Huba, "Hall magnetohydrodynamics - A tutorial," *Sp. Plasma Simul.*, no. 1, pp. 166–192, 2003.

[63] F. H. Ebersohn, "Gas kinetic study of magnetic field effects on plasma," Master's Thesis, Texas A&M University, 2012.

[64] T. Amano, "Divergence-free approximate Riemann solver for the quasi-neutral two-fluid plasma model," *J. Comput. Phys.*, vol. 299, pp. 863–886, 2015. [Online]. Available: http://www.sciencedirect.com/science/article/pii/S0021999115004805

[65] J. C. Huang, K. Xu, and P. Yu, "A unified gas-kinetic scheme for continuum and rarefied flows III: Microflow simulations," *Commun. Comput. Phys.*, vol. 14, no. 5, pp. 1147–1173, 2013. [Online]. Available: http://dx.doi.org/10.1016/j.jcp.2010.06.032

[66] K. Xu and L. Zhihui, "Microchannel Flow in the slip regime: gas-kinetic BGK-burnett solutions," *J. Fluid Mech.*, vol. 513, pp. 87–110, 2004.

[67] T. Ohwada and K. Xu, "The kinetic scheme for the full-Burnett equations," *J. Comput. Phys.*, vol. 201, no. 1, pp. 315–332, 2004.

[68] W. Liao, L.-S. Luo, and K. Xu, "Gas-kinetic scheme for continuum and near-continuum hypersonic flows," *J. Spacecr. Rockets*, vol. 44, no. 6, pp. 1232–1240, 2007. [Online]. Available: http://arc.aiaa.org/doi/abs/10.2514/1.30040

[69] K. Xu, "Regularization of the Chapman-Enskog expansion and its description of shock structure," *Phys. Fluids*, vol. 14, no. 4, 2002.

[70] C. Cai, D. D. Liu, and K. Xu, "One-dimensional multiple-temperature gas-kinetic Bhatnagar-Gross-Krook scheme for shock wave computation," *AIAA J.*, vol. 46, no. 5, pp. 1054–1062, 2008.

[71] K. Xu, X. He, and C. Cai, "Multiple temperature kinetic model and gas-kinetic method for hypersonic non-equilibrium flow computations," *J. Comput. Phys.*, vol. 227, no. 14, pp. 6779–6794, 2008.

[72] J. J. Ramos, "Fluid formalism for collisionless magnetized plasmas," *Phys. Plasmas*,

vol. 12, no. 5, pp. 1–14, 2005.

[73] A. J. Brizard and T. S. Hahm, "Foundations of nonlinear gyrokinetic theory," *Rev. Mod. Phys.*, vol. 79, no. 2, pp. 421–468, 2007.

APPENDIX A

CALCULATING GKS COEFFICIENTS

In calculating many of the terms and coefficients required in the GKS procedure, the tensor $M_{\alpha\beta}^{-1}$ frequently appears.

$$M_{\alpha\beta} \equiv \int g\psi_\alpha\psi_\beta d\boldsymbol{\xi} \tag{A.1}$$

As stated in section 4.1.2, $M_{\alpha\beta}$ is defined by equation (A.1), and its inverse may be determined analytically. If we define the Maxwellian g to be $g = \rho \left(\frac{m}{2\pi kT}\right)^{3/2} e^{-\frac{m}{2kT}(\boldsymbol{\xi}-\boldsymbol{u})^2}$, $M_{\alpha\beta}$ is found to be

$$M_{\alpha\beta} = \rho \left\{ \begin{array}{ccccc} 1 & u & v & w & \mathbb{B}_1 \\ u & \frac{kT}{m} + u^2 & uv & uw & \mathbb{B}_2 \\ v & vu & \frac{kT}{m} + v^2 & vw & \mathbb{B}_3 \\ w & wu & wv & \frac{kT}{m} + w^2 & \mathbb{B}_4 \\ \mathbb{B}_1 & \mathbb{B}_2 & \mathbb{B}_3 & \mathbb{B}_4 & \mathbb{B}_5 \end{array} \right\}, \tag{A.2}$$

where u, v, w are the x-, y-, z-components of $\boldsymbol{u}$. The $\mathbb{B}_\eta$ in equation (A.2) are defined by equations (A.3) – (A.7).

$$\mathbb{B}_1 = \frac{1}{2}\left(u^2 + v^2 + w^2\right) + \frac{3}{2}\frac{kT}{m} \tag{A.3}$$

$$\mathbb{B}_2 = u\left(\frac{1}{2}\left(u^2 + v^2 + w^2\right) + \frac{5}{2}\frac{kT}{m}\right) \tag{A.4}$$

$$\mathbb{B}_3 = v\left(\frac{1}{2}\left(u^2 + v^2 + w^2\right) + \frac{5}{2}\frac{kT}{m}\right) \tag{A.5}$$

$$\mathbb{B}_4 = w\left(\frac{1}{2}\left(u^2 + v^2 + w^2\right) + \frac{5}{2}\frac{kT}{m}\right) \tag{A.6}$$

$$\mathbb{B}_5 = \frac{1}{4}\left(u^2 + v^2 + w^2\right)^2 + \frac{5}{2}\frac{kT}{m}(u^2 + v^2 + w^2)^2 + \frac{15}{4}\left(\frac{kT}{m}\right)^2 \tag{A.7}$$

In defining $M_{\alpha\beta}^{-1}$ it is more perspicuous to define it relative to the solution of e.g., a_β given some b_β, such as in equation (A.8).

$$b_\alpha = M_{\alpha\beta}a_\beta \rightarrow a_\beta = M_{\alpha\beta}^{-1}b_\alpha \tag{A.8}$$

First we define the following:

$$R_5 = 2b_5 - (u^2 + v^2 + w^2 + \frac{3}{2\lambda})b_1 \tag{A.9}$$

$$R_4 = b_4 - wb_1 \tag{A.10}$$

$$R_3 = b_3 - wb_1 \tag{A.11}$$

$$R_2 = b_2 - wb_1 \tag{A.12}$$

From equations (A.9)–(A.12), the a_α can be defined by equations (A.17) – (A.13) in terms of $b_\beta \in [b_1, b_2, b_3, b_4, b_5]$:

$$a_5 = \frac{4}{3}\lambda^2 (R_5 - 2uR_2 - 2vR_3 - 2wR_4) \tag{A.13}$$

$$a_4 = 2\lambda R_4 - wa_5 \tag{A.14}$$

$$a_3 = 2\lambda R_3 - va_5 \tag{A.15}$$

$$a_2 = 2\lambda R_2 - ua_5 \tag{A.16}$$

$$a_1 = b_1 - ua_2 - va_3 - wa_4 - \frac{1}{2}a_5 \left(u^2 + v^2 + w^2 + \frac{3}{2\lambda}\right) \tag{A.17}$$

Where in equations (A.17)–(A.13) we define $\lambda \equiv \frac{m}{2kT}$.

APPENDIX B

DISCRETE GKS FLUX EXPRESSIONS

Recalling the left- and right- definitions from section 4.1.3, and the moment definition $\langle \theta \rangle \equiv \int \theta g(\boldsymbol{\xi}) d\boldsymbol{\xi}$, we will for convenience redefine the moments to be

$$\bar{a}_\beta^2 \langle \psi_\beta \xi_j \rangle^0 = \int g^0 \bar{a}_\beta^2 \psi_\beta \xi_j d\boldsymbol{\xi} \tag{B.1}$$

$$\bar{a}_\beta^{1,l} \langle \psi_\beta \xi_j \rangle_{>0}^{0,l} = \int g^0 \bar{a}_\beta^{1,l} \psi_\beta \xi_j d\boldsymbol{\xi} \tag{B.2}$$

$$A_\beta^l \langle \psi_\beta \xi_j \rangle_{>0}^l = \int g^l A_\beta^l \psi_\beta \xi_j d\boldsymbol{\xi} \tag{B.3}$$

From which equation (4.19) will become (in the x-direction):

$$\bar{F}_1^{\psi_\sigma} = \left(\langle \psi_\sigma \xi_1 \rangle^0 \gamma_1 - \gamma_2 \left[\bar{a}_\beta^{1,l} \langle \psi_\beta \psi_\sigma \xi_1^2 \rangle_{>0}^{0,l} + \bar{a}_\beta^{1,r} \langle \psi_\beta \psi_\sigma \xi_1^2 \rangle_{<0}^{0,r} \right. \right.$$

$$\left. + \bar{a}_\beta^2 \langle \psi_\beta \psi_\sigma \xi_1 \xi_2 \rangle^0 + \bar{a}_\beta^3 \langle \psi_\beta \psi_\sigma \xi_1 \xi_3 \rangle^0 \right] + \gamma_3 \bar{A}_\beta \langle \psi_\beta \psi_\sigma \xi_1 \rangle^0 \right)$$

$$+ \left\langle g^0 H(\xi_1) \left(\gamma_1 - \gamma_2 \left[a_\beta^{1,l} \psi_\beta \xi_1 + a_\beta^{2,l} \psi_\beta \xi_2 + a_\beta^3 \psi_\beta \xi_3 \right] + \gamma_3 A_\beta^l \psi_\beta \right.\right.$$

$$\left. - \gamma_4 \left[B_\beta^l \psi_\beta + b_\beta^{1,l} \psi_\beta \xi_1 + b_\beta^{2,l} \psi_\beta \xi_2 + b_\beta^{3,l} \psi_\beta \xi_3 - 2 \left(\frac{m}{2kT} \right) F_{B,i}^l (\xi_i - \bar{u}_i) \right] \right)$$

$$\left[\left(\frac{\tau q}{m} \boldsymbol{E}^l + \frac{\tau \boldsymbol{U}^l}{\tau_\beta} \right) + \frac{\tau q}{m} (\boldsymbol{\xi} \times \boldsymbol{B}^l) \right] \cdot \boldsymbol{\nabla}_{\boldsymbol{\xi}} \left(\psi_\sigma \xi_1 \right)$$

$$+ g^0 (1 - H(\xi_1)) \left(\gamma_1 - \gamma_2 \left[a_\beta^{1,r} \psi_\beta \xi_1 + a_\beta^{2,r} \psi_\beta \xi_2 + a_\beta^3 \psi_\beta \xi_3 \right] + \gamma_3 A_\beta^r \psi_\beta \right.$$

$$\left. - \gamma_4 \left[B_\beta^r \psi_\beta + b_\beta^{1,r} \psi_\beta \xi_1 + b_\beta^{2,r} \psi_\beta \xi_2 + b_\beta^{3,r} \psi_\beta \xi_3 - 2 \left(\frac{m}{2kT} \right) F_{B,i}^r (\xi_i - \bar{u}_i) \right] \right)$$

$$\left. \left[\left(\frac{\tau q}{m} \boldsymbol{E}^r + \frac{\tau \boldsymbol{U}^r}{\tau_\beta} \right) + \frac{\tau q}{m} (\boldsymbol{\xi} \times \boldsymbol{B}^r) \right] \cdot \boldsymbol{\nabla}_{\boldsymbol{\xi}} \left(\psi_\sigma \xi_1 \right) \right\rangle$$

$$+ \left(\langle \psi_\sigma \xi_1 \rangle_{>0}^l \gamma_5 - \gamma_4 \left[a_\beta^{1,l} \langle \psi_\beta \psi_\sigma \xi_1^2 \rangle_{>0}^l + a_\beta^{2,l} \langle \psi_\beta \psi_\sigma \xi_1 \xi_2 \rangle_{>0}^l + a_\beta^{3,l} \langle \psi_\beta \psi_\sigma \xi_1 \xi_3 \rangle_{>0}^l \right] \right.$$

$$
-\tau\gamma_5\Big[B_\beta^l\langle\psi_\beta\psi_\sigma\xi_1\rangle_{>0}^l + b_\beta^{1,l}\langle\psi_\beta\psi_\sigma\xi_1^2\rangle_{>0}^l + b_\beta^{2,l}\langle\psi_\beta\psi_\sigma\xi_1\xi_2\rangle_{>0}^l + b_\beta^{3,l}\langle\psi_\beta\psi_\sigma\xi_1\xi_3\rangle_{>0}^l
$$

$$
- 2\left(\frac{m}{2kT}\right)F_{B,i}^l\left(\langle\psi_\sigma\xi_1\xi_i\rangle_{>0}^l - \langle\psi_\sigma\xi_1\rangle_{>0}^l u_i\right)\Big]\Big)
$$

$$
+\Big(\langle\psi_\sigma\xi_1\rangle_{<0}^r\gamma_5 - \gamma_4\Big[a_\beta^{1,r}\langle\psi_\beta\psi_\sigma\xi_1^2\rangle_{<0}^r + a_\beta^{2,r}\langle\psi_\beta\psi_\sigma\xi_1\xi_2\rangle_{<0}^r + a_\beta^{3,r}\langle\psi_\beta\psi_\sigma\xi_1\xi_3\rangle_{<0}^r\Big]
$$

$$
-\tau\gamma_5\Big[B_\beta^r\langle\psi_\beta\psi_\sigma\xi_1\rangle_{<0}^r + b_\beta^{1,r}\langle\psi_\beta\psi_\sigma\xi_1^2\rangle_{<0}^r + b_\beta^{2,r}\langle\psi_\beta\psi_\sigma\xi_1\xi_2\rangle_{<0}^r + b_\beta^{3,r}\langle\psi_\beta\psi_\sigma\xi_1\xi_3\rangle_{<0}^r
$$

$$
- 2\left(\frac{m}{2kT}\right)F_{B,i}^r\left(\langle\psi_\sigma\xi_1\xi_i\rangle_{<0}^r - \langle\psi_\sigma\xi_1\rangle_{<0}^r u_i\right)\Big]\Big) \qquad \text{(B.4)}
$$

For the fluxes in the y- and z-directions – ie $\bar{F}_2^{\psi_\sigma}$ and $\bar{F}_3^{\psi_\sigma}$ – the same equation may be used by simply rotating all indices. For example, for the y-flux we will have the following.

$$
\begin{bmatrix} \bar{a}_\beta^{1,l}\langle\psi_\beta\psi_\sigma\xi_1^2\rangle_{>0}^{0,l} + \bar{a}_\beta^{1,r}\langle\psi_\beta\psi_\sigma\xi_1^2\rangle_{<0}^{0,r} \\ +\bar{a}_\beta^2\langle\psi_\beta\psi_\sigma\xi_1\xi_2\rangle^0 + \bar{a}_\beta^3\langle\psi_\beta\psi_\sigma\xi_1\xi_3\rangle^0 \end{bmatrix} \rightarrow \begin{bmatrix} \bar{a}_\beta^{2,l}\langle\psi_\beta\psi_\sigma\xi_2^2\rangle_{>0}^{0,l} + \bar{a}_\beta^{2,r}\langle\psi_\beta\psi_\sigma\xi_2^2\rangle_{<0}^{0,r} \\ +\bar{a}_\beta^3\langle\psi_\beta\psi_\sigma\xi_2\xi_3\rangle^0 + \bar{a}_\beta^1\langle\psi_\beta\psi_\sigma\xi_2\xi_1\rangle^0 \end{bmatrix} \qquad \text{(B.5)}
$$

For the z-flux, the repeat the above for one more rotation. Notice that equation (B.4) still contains a great deal of repeated indices – e.g., $a_\beta\psi_\beta$ – and further, that the the terms containing $\nabla_\xi(\psi_\sigma\xi_1)$ must still be applied and expanded.

The coefficients γ in Eq. (B.4) can be defined in terms of the terminology used in the code:

$$
\gamma_1 = A/ADE = TAU - SE1 \qquad \text{(B.6)}
$$

$$
\gamma_2 = -SET2 \qquad \text{(B.7)}
$$

$$
\gamma_3 = B \qquad \text{(B.8)}
$$

$$
\gamma_4 = SETV - SETA = SET1 \qquad \text{(B.9)}
$$

$$
\gamma_5 = SE1 \qquad \text{(B.10)}
$$

$$
\tau\gamma_5 = TE * SE1 = SETA \qquad \text{(B.11)}
$$

$$
\gamma_4 + \tau\gamma_5 = SETV = \gamma_6 \qquad \text{(B.12)}
$$

Further, we define the following terms in the code:

$$A * S1 = \langle \psi_\sigma \xi_1 \rangle^0 \gamma_1 \tag{B.13}$$

$$SET2 * TRIU2 = -\gamma_2 \Big[\bar{a}_\beta^{1,l} \langle \psi_\beta \psi_\sigma \xi_1^2 \rangle_{>0}^{0,l} + \bar{a}_\beta^{1,r} \langle \psi_\beta \psi_\sigma \xi_1^2 \rangle_{<0}^{0,r} + \bar{a}_\beta^2 \langle \psi_\beta \psi_\sigma \xi_1 \xi_2 \rangle^0$$
$$+ \bar{a}_\beta^3 \langle \psi_\beta \psi_\sigma \xi_1 \xi_3 \rangle^0 \Big] \tag{B.14}$$

$$B * ATRIU = \gamma_3 \bar{A}_\beta \langle \psi_\beta \psi_\sigma \xi_1 \rangle^0 \tag{B.15}$$

$$FM1 = \langle \psi_\sigma \xi_1 \rangle_{>0}^l \gamma_5 - \gamma_4 \left[a_\beta^{1,l} \langle \psi_\beta \psi_\sigma \xi_1^2 \rangle_{>0}^l + a_\beta^{2,l} \langle \psi_\beta \psi_\sigma \xi_1 \xi_2 \rangle_{>0}^l + a_\beta^{3,l} \langle \psi_\beta \psi_\sigma \xi_1 \xi_3 \rangle_{>0}^l \right]$$

$$FM2 = \langle \psi_\sigma \xi_1 \rangle_{<0}^r \gamma_5 - \gamma_4 \left[a_\beta^{1,r} \langle \psi_\beta \psi_\sigma \xi_1^2 \rangle_{<0}^r + a_\beta^{2,r} \langle \psi_\beta \psi_\sigma \xi_1 \xi_2 \rangle_{<0}^r + a_\beta^{3,r} \langle \psi_\beta \psi_\sigma \xi_1 \xi_3 \rangle_{<0}^r \right]$$
$$- \tau \gamma_5 \left[b_\beta^{1,r} \langle \psi_\beta \psi_\sigma \xi_1^2 \rangle_{<0}^r + b_\beta^{2,r} \langle \psi_\beta \psi_\sigma \xi_1 \xi_2 \rangle_{<0}^r + b_\beta^{3,r} \langle \psi_\beta \psi_\sigma \xi_1 \xi_3 \rangle_{<0}^r \right]$$
$$\tag{B.17}$$

$$-SETA * FMA = -\tau \gamma_5 \Big[B_\beta^l \langle \psi_\beta \psi_\sigma \xi_1 \rangle_{>0}^l - 2 \left(\frac{m}{2kT} \right) F_{B,i}^l \left(\langle \psi_\sigma \xi_1 \xi_i \rangle_{>0}^l - \langle \psi_\sigma \xi_1 \rangle_{>0}^l u_i \right) \Big]$$
$$- \tau \gamma_5 \Big[B_\beta^r \langle \psi_\beta \psi_\sigma \xi_1 \rangle_{<0}^r - 2 \left(\frac{m}{2kT} \right) F_{B,i}^r \left(\langle \psi_\sigma \xi_1 \xi_i \rangle_{<0}^r - \langle \psi_\sigma \xi_1 \rangle_{<0}^r u_i \right) \Big]$$
$$\tag{B.18}$$

Recall, $\gamma_4 = SETV - SETA = SET1$, $\gamma_5 = SE1$, $\tau \gamma_5 = TE * SE1 = SETA$.

Such that Eq. (B.4) becomes:

$$\Psi^{(\sigma)}(\boldsymbol{x}) = A * S1 + SET2 * TRIU2 + B * ATRIU$$

$$+ g^0 H(\xi_1) \Bigg(\gamma_1 - \gamma_2 \Big[a_\beta^{1,l} \psi_\beta \xi_1 + a_\beta^{2,l} \psi_\beta \xi_2 + a_\beta^3 \psi_\beta \xi_3 \Big] + \gamma_3 A_\beta^l \psi_\beta$$

$$- \gamma_4 \Big[B_\beta^l \psi_\beta + b_\beta^{1,l} \psi_\beta \xi_1 + b_\beta^{2,l} \psi_\beta \xi_2 + b_\beta^{3,l} \psi_\beta \xi_3 - 2 \left(\frac{m}{2kT} \right) F_{B,i}^l (\xi_i - \bar{u}_i) \Big] \Bigg)$$

$$\left[\left(\frac{\tau q}{m} \boldsymbol{E}^l + \frac{\tau \boldsymbol{U}^l}{\tau_\beta} \right) + \frac{\tau q}{m} (\boldsymbol{\xi} \times \boldsymbol{B}^l) \right] \cdot \boldsymbol{\nabla}_{\boldsymbol{\xi}} \Big(\psi_\sigma \xi_1 \Big)$$

$$+ g^0 (1 - H(\xi_1)) \Bigg(\gamma_1 - \gamma_2 \Big[a_\beta^{1,r} \psi_\beta \xi_1 + a_\beta^{2,r} \psi_\beta \xi_2 + a_\beta^3 \psi_\beta \xi_3 \Big] + \gamma_3 A_\beta^r \psi_\beta$$

$$- \gamma_4 \Big[B_\beta^r \psi_\beta + b_\beta^{1,r} \psi_\beta \xi_1 + b_\beta^{2,r} \psi_\beta \xi_2 + b_\beta^{3,r} \psi_\beta \xi_3 - 2 \left(\frac{m}{2kT} \right) F_{B,i}^r (\xi_i - \bar{u}_i) \Big] \Bigg)$$

$$\left[\left(\frac{\tau q}{m} \boldsymbol{E}^r + \frac{\tau \boldsymbol{U}^r}{\tau_\beta} \right) + \frac{\tau q}{m} (\boldsymbol{\xi} \times \boldsymbol{B}^r) \right] \cdot \boldsymbol{\nabla}_{\boldsymbol{\xi}} \Big(\psi_\sigma \xi_1 \Big)$$

$$+ FM1 + FM2 - SETA * FMA \quad \text{(B.19)}$$

We must still define the two extra sets of terms:

$$g^0 H(\xi_1) \Bigg(\gamma_1 - \gamma_2 \Big[a_\beta^{1,l} \psi_\beta \xi_1 + a_\beta^{2,l} \psi_\beta \xi_2 + a_\beta^3 \psi_\beta \xi_3 \Big] + \gamma_3 A_\beta^l \psi_\beta$$

$$- \gamma_4 \Big[B_\beta^l \psi_\beta + b_\beta^{1,l} \psi_\beta \xi_1 + b_\beta^{2,l} \psi_\beta \xi_2 + b_\beta^{3,l} \psi_\beta \xi_3 - 2 \left(\frac{m}{2kT} \right) F_{B,i}^l (\xi_i - \bar{u}_i) \Big] \Bigg)$$

$$\left[\left(\frac{\tau q}{m} \boldsymbol{E}^l + \frac{\tau \boldsymbol{U}^l}{\tau_\beta} \right) + \frac{\tau q}{m} (\boldsymbol{\xi} \times \boldsymbol{B}^l) \right] \cdot \boldsymbol{\nabla}_{\boldsymbol{\xi}} \Big(\psi_\sigma \xi_1 \Big) \quad \text{(B.20)}$$

$$g^0 \left(1 - H(\xi_1)\right) \left(\gamma_1 - \gamma_2 \left[a_\beta^{1,r} \psi_\beta \xi_1 + a_\beta^{2,r} \psi_\beta \xi_2 + a_\beta^3 \psi_\beta \xi_3 \right] + \gamma_3 A_\beta^r \psi_\beta \right.$$

$$\left. - \gamma_4 \left[B_\beta^r \psi_\beta + b_\beta^{1,r} \psi_\beta \xi_1 + b_\beta^{2,r} \psi_\beta \xi_2 + b_\beta^{3,r} \psi_\beta \xi_3 - 2 \left(\frac{m}{2kT} \right) F_{B,i}^r (\xi_i - \bar{u}_i) \right] \right)$$

$$\left[\left(\frac{\tau q}{m} \boldsymbol{E}^r + \frac{\tau \boldsymbol{U}^r}{\tau_\beta} \right) + \frac{\tau q}{m} (\boldsymbol{\xi} \times \boldsymbol{B}^r) \right] \cdot \boldsymbol{\nabla}_{\boldsymbol{\xi}} \left(\psi_\sigma \xi_1 \right) \quad \text{(B.21)}$$

The terms inside the first big set of parentheses remind us of the coefficient definitions we see elsewhere in the development. However, these are modified by the terms in the bracket involving $\boldsymbol{E}$ and $\boldsymbol{B}$ and $\boldsymbol{\nabla}_{\boldsymbol{\xi}} \left(\psi_\sigma \xi_1 \right)$

$$\left[\left(\frac{\tau q}{m} E_1^l + \frac{\tau U_1^l}{\tau_\beta} \right) \left(\psi_\sigma + \xi_1 \frac{\partial \psi_\sigma}{\partial \xi_1} \right) + \left(\frac{\tau q}{m} E_2^l + \frac{\tau U_2^l}{\tau_\beta} \right) \xi_1 \frac{\partial \psi_\sigma}{\partial \xi_2} + \left(\frac{\tau q}{m} E_3^l + \frac{\tau U_3^l}{\tau_\beta} \right) \xi_1 \frac{\partial \psi_\sigma}{\partial \xi_3} \right.$$

$$+ \frac{\tau q}{m} \left(\xi_2 B_3^l - \xi_3 B_2^l \right) \psi_\sigma + \frac{\tau q}{m} \left(\xi_2 \xi_1 B_3^l - \xi_3 \xi_1 B_2^l \right) \frac{\partial \psi_\sigma}{\partial \xi_1}$$

$$\left. + \frac{\tau q}{m} \left(\xi_3 \xi_1 B_1^l - \xi_1^2 B_3^l \right) \frac{\partial \psi_\sigma}{\partial \xi_2} + \frac{\tau q}{m} \left(\xi_1^2 B_2^l - \xi_2 \xi_1 B_1^l \right) \frac{\partial \psi_\sigma}{\partial \xi_3} \right] \quad \text{(B.22)}$$

Here we recall $\psi_\sigma = [1, \xi_1, \xi_2, \xi_3, \frac{1}{2}(\xi^2 + \zeta^2)]$, ζ indicating the internal degrees of freedom, so we have:

$$\frac{\partial \psi_\sigma}{\partial \xi_1} = [0, 1, 0, 0, \xi_1] \quad \text{(B.23)}$$

$$\frac{\partial \psi_\sigma}{\partial \xi_2} = [0, 0, 1, 0, \xi_2] \quad \text{(B.24)}$$

$$\frac{\partial \psi_\sigma}{\partial \xi_3} = [0, 0, 0, 1, \xi_3] \quad \text{(B.25)}$$

Thus, for mass, momentum, and energy fluxes, Eq. (B.22) becomes:

$$\left[\left(\frac{\tau q}{m}E_1^l + \frac{\tau U_1^l}{\tau_\beta}\right) + \frac{\tau q}{m}\left(\xi_2 B_3^l - \xi_3 B_2^l\right)\right] \tag{B.26}$$

$$\left[\left(\frac{\tau q}{m}E_1^l + \frac{\tau U_1^l}{\tau_\beta}\right)(2\xi_1) + 2\frac{\tau q}{m}\left(\xi_2\xi_1 B_3^l - \xi_3\xi_1 B_2^l\right)\right] \tag{B.27}$$

$$\left[\left(\frac{\tau q}{m}E_1^l + \frac{\tau U_1^l}{\tau_\beta}\right)(\xi_2) + \left(\frac{\tau q}{m}E_2^l + \frac{\tau U_2^l}{\tau_\beta}\right)\xi_1 + \frac{\tau q}{m}\left(\xi_2^2 B_3^l - \xi_3\xi_2 B_2^l\right)\right.$$
$$\left. + \frac{\tau q}{m}\left(\xi_3\xi_1 B_1^l - \xi_1^2 B_3^l\right)\right] \tag{B.28}$$

$$\left[\left(\frac{\tau q}{m}E_1^l + \frac{\tau U_1^l}{\tau_\beta}\right)(\xi_3) + \left(\frac{\tau q}{m}E_3^l + \frac{\tau U_3^l}{\tau_\beta}\right)\xi_1 + \frac{\tau q}{m}\left(\xi_2\xi_3 B_3^l - \xi_3^2 B_2^l\right)\right.$$
$$\left. + \frac{\tau q}{m}\left(\xi_1^2 B_2^l - \xi_2\xi_1 B_1^l\right)\right] \tag{B.29}$$

$$\left[\left(\frac{\tau q}{m}E_1^l + \frac{\tau U_1^l}{\tau_\beta}\right)\left(\frac{3}{2}\xi_1^2 + \frac{1}{2}(\xi_2^2 + \xi_3^2)\right) + \left(\frac{\tau q}{m}E_2^l + \frac{\tau U_2^l}{\tau_\beta}\right)\xi_1\xi_2 + \left(\frac{\tau q}{m}E_3^l + \frac{\tau U_3^l}{\tau_\beta}\right)\xi_1\xi_3\right.$$
$$+ \frac{\tau q}{m}\left(\frac{1}{2}\xi_2^3 B_3^l - \frac{1}{2}\xi_3\xi_2^2 B_2^l\right) + \frac{\tau q}{m}\left(\frac{1}{2}\xi_3^2\xi_2 B_3^l - \frac{1}{2}\xi_3^3 B_2^l\right) + \frac{\tau q}{m}\left(\frac{1}{2}\xi_1^2\xi_2 B_3^l\right) - \frac{\tau q}{m}\left(\frac{1}{2}\xi_1^2\xi_3 B_2^l\right)$$
$$\left. + \left(\frac{\tau q}{m}E_1^l + \frac{\tau U_1^l}{\tau_\beta}\right)\left(\frac{1}{2}\zeta^2\right) + \frac{\tau q}{m}\left(\frac{1}{2}\xi_2\zeta^2 B_3^l - \frac{1}{2}\xi_3\zeta^2 B_2^l\right)\right] \tag{B.30}$$

Where Eq. (B.26) is for mass, Eqs. (B.27), (B.28), (B.29) are for momentum, and Eq. (B.30) is for energy.

If we define $\frac{\tau q}{m}E_i^l + \frac{\tau U_i^l}{\tau_\beta} = G_i^l$, and $\frac{\tau q}{m}B_i^l = W_i^l$, the extra sets of terms in Eqs. (B.20) and (B.21) become the following:

For mass:

$$
\begin{aligned}
\Bigg(\gamma_1 - \gamma_2 \Big[a_\beta^{1,l} \psi_\beta \xi_1 + a_\beta^{2,l} \psi_\beta \xi_2 + a_\beta^3 \psi_\beta \xi_3 \Big] + \gamma_3 A_\beta^l \psi_\beta \\
- \gamma_4 \Big[B_\beta^l \psi_\beta + b_\beta^{1,l} \psi_\beta \xi_1 + b_\beta^{2,l} \psi_\beta \xi_2 + b_\beta^{3,l} \psi_\beta \xi_3 - 2 \left(\frac{m}{2kT} \right) F_{B,i}^l \left(\xi_i - \bar{u}_i \right) \Big] \Bigg) \\
\Big[G_1^l + \xi_2 W_3^l - \xi_3 W_2^l \Big]
\end{aligned}
$$

For X-momentum:

$$
\begin{aligned}
\Bigg(\gamma_1 - \gamma_2 \Big[a_\beta^{1,l} \psi_\beta \xi_1 + a_\beta^{2,l} \psi_\beta \xi_2 + a_\beta^3 \psi_\beta \xi_3 \Big] + \gamma_3 A_\beta^l \psi_\beta \\
- \gamma_4 \Big[B_\beta^l \psi_\beta + b_\beta^{1,l} \psi_\beta \xi_1 + b_\beta^{2,l} \psi_\beta \xi_2 + b_\beta^{3,l} \psi_\beta \xi_3 - 2 \left(\frac{m}{2kT} \right) F_{B,i}^l \left(\xi_i - \bar{u}_i \right) \Big] \Bigg) \\
\Big[2 G_1^l \xi_1 + 2 \xi_2 \xi_1 W_3^l - 2 \xi_3 \xi_1 W_2^l \Big]
\end{aligned}
$$

For Y-momentum:

$$
\begin{aligned}
\Bigg(\gamma_1 - \gamma_2 \Big[a_\beta^{1,l} \psi_\beta \xi_1 + a_\beta^{2,l} \psi_\beta \xi_2 + a_\beta^3 \psi_\beta \xi_3 \Big] + \gamma_3 A_\beta^l \psi_\beta \\
- \gamma_4 \Big[B_\beta^l \psi_\beta + b_\beta^{1,l} \psi_\beta \xi_1 + b_\beta^{2,l} \psi_\beta \xi_2 + b_\beta^{3,l} \psi_\beta \xi_3 - 2 \left(\frac{m}{2kT} \right) F_{B,i}^l \left(\xi_i - \bar{u}_i \right) \Big] \Bigg) \\
\Big[G_1^l \xi_2 + G_2^l \xi_1 + \xi_2^2 W_3^l - \xi_3 \xi_2 W_2^l + \xi_3 \xi_1 W_1^l - \xi_1^2 W_3^l \Big]
\end{aligned}
$$

For Z-momentum:

$$
\begin{aligned}
\Bigg(\gamma_1 - \gamma_2 &\Big[a_\beta^{1,l} \psi_\beta \xi_1 + a_\beta^{2,l} \psi_\beta \xi_2 + a_\beta^3 \psi_\beta \xi_3 \Big] + \gamma_3 A_\beta^l \psi_\beta \\
&- \gamma_4 \Big[B_\beta^l \psi_\beta + b_\beta^{1,l} \psi_\beta \xi_1 + b_\beta^{2,l} \psi_\beta \xi_2 + b_\beta^{3,l} \psi_\beta \xi_3 - 2 \left(\frac{m}{2kT} \right) F_{B,i}^l \left(\xi_i - \bar{u}_i \right) \Big] \Bigg) \\
&\qquad\qquad \Big[G_1^l \xi_3 + G_3^l \xi_1 + \xi_2 \xi_3 W_3^l - \xi_3^2 W_2^l + \xi_1^2 W_2^l - \xi_2 \xi_1 W_1^l \Big]
\end{aligned}
$$

For Energy:

$$
\begin{aligned}
\Bigg(\gamma_1 - \gamma_2 &\Big[a_\beta^{1,l} \psi_\beta \xi_1 + a_\beta^{2,l} \psi_\beta \xi_2 + a_\beta^3 \psi_\beta \xi_3 \Big] + \gamma_3 A_\beta^l \psi_\beta \\
&- \gamma_4 \Big[B_\beta^l \psi_\beta + b_\beta^{1,l} \psi_\beta \xi_1 + b_\beta^{2,l} \psi_\beta \xi_2 + b_\beta^{3,l} \psi_\beta \xi_3 - 2 \left(\frac{m}{2kT} \right) F_{B,i}^l \left(\xi_i - \bar{u}_i \right) \Big] \Bigg) \\
& \Big[G_1^l \left(\frac{1}{2} \zeta^2 + \frac{3}{2} \xi_1^2 + \frac{1}{2} (\xi_2^2 + \xi_3^2) \right) + G_2^l \xi_1 \xi_2 + G_3^l \xi_1 \xi_3 + \frac{1}{2} \xi_2^3 W_3^l \\
& - \frac{1}{2} \xi_3 \xi_2^2 W_2^l + \frac{1}{2} \xi_3^2 \xi_2 W_3^l - \frac{1}{2} \xi_3^3 W_2^l + \frac{1}{2} \xi_1^2 \xi_2 W_3^l - \frac{1}{2} \xi_1^2 \xi_3 W_2^l + \frac{1}{2} \xi_2 \zeta^2 W_3^l - \frac{1}{2} \xi_3 \zeta^2 W_2^l \Big]
\end{aligned}
$$

Thus for in terms of the moments $\langle\cdot\rangle$ we get for e.g., mass conservation:

$$
G_1^l\Bigg(\gamma_1\langle 1\rangle_{>0}^{0,l} - \gamma_2\Big[a_\beta^{1,l}\langle\psi_\beta\xi_1\rangle_{>0}^{0,l} + a_\beta^{2,l}\langle\psi_\beta\xi_2\rangle_{>0}^{0,l} + a_\beta^3\langle\psi_\beta\xi_3\rangle_{>0}^{0,l}\Big] + \gamma_3 A_\beta^l\langle\psi_\beta\rangle_{>0}^{0,l}
$$

$$
- \gamma_4\Big[B_\beta^l\langle\psi_\beta\rangle_{>0}^{0,l} + b_\beta^{1,l}\langle\psi_\beta\xi_1\rangle_{>0}^{0,l} + b_\beta^{2,l}\langle\psi_\beta\xi_2\rangle_{>0}^{0,l} + b_\beta^{3,l}\langle\psi_\beta\xi_3\rangle_{>0}^{0,l}
$$

$$
+ 2\left(\frac{m}{2kT}\right)\left(F_{B,i}^l\bar{u}_i\langle 1\rangle_{>0}^{0,l} - F_{B,1}^l\langle\xi_1\rangle_{>0}^{0,l} - F_{B,2}^l\langle\xi_2\rangle_{>0}^{0,l} - F_{B,3}^l\langle\xi_3\rangle_{>0}^{0,l}\right)\Big]\Bigg)
$$

$$
+ W_3^l\Bigg(\langle\gamma_1\xi_2\rangle_{>0}^{0,l} - \gamma_2\Big[a_\beta^{1,l}\langle\psi_\beta\xi_1\xi_2\rangle_{>0}^{0,l} + a_\beta^{2,l}\langle\psi_\beta\xi_2^2\rangle_{>0}^{0,l} + a_\beta^3\langle\psi_\beta\xi_3\xi_2\rangle_{>0}^{0,l}\Big] + \gamma_3 A_\beta^l\langle\psi_\beta\xi_2\rangle_{>0}^{0,l}
$$

$$
- \gamma_4\Big[B_\beta^l\langle\psi_\beta\xi_2\rangle_{>0}^{0,l} + b_\beta^{1,l}\langle\psi_\beta\xi_1\xi_2\rangle_{>0}^{0,l} + b_\beta^{2,l}\langle\psi_\beta\xi_2^2\rangle_{>0}^{0,l} + b_\beta^{3,l}\langle\psi_\beta\xi_3\xi_2\rangle_{>0}^{0,l}
$$

$$
+ 2\left(\frac{m}{2kT}\right)\left(F_{B,i}^l\bar{u}_i\langle\xi_2\rangle_{>0}^{0,l} - F_{B,1}^l\langle\xi_1\xi_2\rangle_{>0}^{0,l} - F_{B,2}^l\langle\xi_2^2\rangle_{>0}^{0,l} - F_{B,3}^l\langle\xi_3\xi_2\rangle_{>0}^{0,l}\right)\Big]\Bigg)
$$

$$
- W_2^l\Bigg(\langle\gamma_1\xi_3\rangle_{>0}^{0,l} - \gamma_2\Big[a_\beta^{1,l}\langle\psi_\beta\xi_1\xi_3\rangle_{>0}^{0,l} + a_\beta^{2,l}\langle\psi_\beta\xi_2\xi_3\rangle_{>0}^{0,l} + a_\beta^3\langle\psi_\beta\xi_3^2\rangle_{>0}^{0,l}\Big] + \gamma_3 A_\beta^l\langle\psi_\beta\xi_3\rangle_{>0}^{0,l}
$$

$$
- \gamma_4\Big[B_\beta^l\langle\psi_\beta\xi_3\rangle_{>0}^{0,l} + b_\beta^{1,l}\langle\psi_\beta\xi_1\xi_3\rangle_{>0}^{0,l} + b_\beta^{2,l}\langle\psi_\beta\xi_2\xi_3\rangle_{>0}^{0,l} + b_\beta^{3,l}\langle\psi_\beta\xi_3^2\rangle_{>0}^{0,l}
$$

$$
+ 2\left(\frac{m}{2kT}\right)\left(F_{B,i}^l\bar{u}_i\langle\xi_3\rangle_{>0}^{0,l} - F_{B,1}^l\langle\xi_1\xi_3\rangle_{>0}^{0,l} - F_{B,2}^l\langle\xi_2\xi_3\rangle_{>0}^{0,l} - F_{B,3}^l\langle\xi_3^2\rangle_{>0}^{0,l}\right)\Big]\Bigg)
$$

In general, these terms for mass, momentum, and energy fluxes are all composed of:

$$
\Pi^l\Bigg\langle\theta\Bigg(\gamma_1 - \gamma_2\Big[a_\beta^{1,l}\psi_\beta\xi_1 + a_\beta^{2,l}\psi_\beta\xi_2 + a_\beta^3\psi_\beta\xi_3\Big] + \gamma_3 A_\beta^l\psi_\beta
$$

$$
- \gamma_4\Big[B_\beta^l\psi_\beta + b_\beta^{1,l}\psi_\beta\xi_1 + b_\beta^{2,l}\psi_\beta\xi_2 + b_\beta^{3,l}\psi_\beta\xi_3
$$

$$
+ 2\left(\frac{m}{2kT}\right)\left(F_{B,i}^l\bar{u}_i - F_{B,1}^l\xi_1 - F_{B,2}^l\xi_2 - F_{B,3}^l\xi_3\right)\Big]\Bigg)\Bigg\rangle \quad\text{(B.31)}
$$

Where the $\Pi^l \theta$ correspond to e.g., $W_3^l \xi_2$ in the following:

$$\left[G_1^l + \xi_2 W_3^l - \xi_3 W_2^l \right] \tag{B.32}$$

$$\left[2G_1^l \xi_1 + 2\xi_2 \xi_1 W_3^l - 2\xi_3 \xi_1 W_2^l \right] \tag{B.33}$$

$$\left[G_1^l \xi_2 + G_2^l \xi_1 + \xi_2^2 W_3^l - \xi_3 \xi_2 W_2^l + \xi_3 \xi_1 W_1^l - \xi_1^2 W_3^l \right] \tag{B.34}$$

$$\left[G_1^l \xi_3 + G_3^l \xi_1 + \xi_2 \xi_3 W_3^l - \xi_3^2 W_2^l + \xi_1^2 W_2^l - \xi_2 \xi_1 W_1^l \right] \tag{B.35}$$

$$\left[G_1^l \left(\frac{1}{2}\zeta^2 + \frac{3}{2}\xi_1^2 + \frac{1}{2}(\xi_2^2 + \xi_3^2) \right) + G_2^l \xi_1 \xi_2 + G_3^l \xi_1 \xi_3 + \frac{1}{2}\xi_2^3 W_3^l \right.$$
$$\left. - \frac{1}{2}\xi_3 \xi_2^2 W_2^l + \frac{1}{2}\xi_3^2 \xi_2 W_3^l - \frac{1}{2}\xi_3^3 W_2^l + \frac{1}{2}\xi_1^2 \xi_2 W_3^l - \frac{1}{2}\xi_1^2 \xi_3 W_2^l + \frac{1}{2}\xi_2 \zeta^2 W_3^l - \frac{1}{2}\xi_3 \zeta^2 W_2^l \right] \tag{B.36}$$

Which boils down to the moments of Eq. (B.31) on the following polynomials in ξ_i and ζ:

1	ξ_1	ξ_2	ξ_3	$\xi_1\xi_2$	$\xi_1\xi_3$	ξ_1^2	ξ_2^2	ζ^2	
$\xi_2\xi_3$	ξ_3^2	ξ_2^3	ξ_3^3	$\xi_2^2\xi_3$	$\xi_3^2\xi_2$	$\xi_1^2\xi_2$	$\xi_1^2\xi_3$	$\xi_2\zeta^2$	$\xi_3\zeta^2$

Which gives us:

$$\Pi^l \left(\gamma_1 \langle \theta \rangle_{>0}^{0,l} - \gamma_2 \left[a_\beta^{1,l} \langle \psi_\beta \xi_1 \theta \rangle_{>0}^{0,l} + a_\beta^{2,l} \langle \psi_\beta \xi_2 \theta \rangle_{>0}^{0,l} + a_\beta^3 \langle \psi_\beta \xi_3 \theta \rangle_{>0}^{0,l} \right] - \gamma_4 \left[b_\beta^{1,l} \langle \psi_\beta \xi_1 \theta \rangle_{>0}^{0,l} \right. \right.$$

$$\left. + b_\beta^{2,l} \langle \psi_\beta \xi_2 \theta \rangle_{>0}^{0,l} + b_\beta^{3,l} \langle \psi_\beta \xi_3 \theta \rangle_{>0}^{0,l} \right] + \gamma_3 A_\beta^l \langle \psi_\beta \theta \rangle_{>0}^{0,l} - \gamma_4 \left[B_\beta^l \langle \psi_\beta \theta \rangle_{>0}^{0,l} \right.$$

$$\left. \left. + 2 \left(\frac{m}{2kT} \right) \left(F_{B,i}^l \bar{u}_i \langle \theta \rangle_{>0}^{0,l} - F_{B,1}^l \langle \xi_1 \theta \rangle_{>0}^{0,l} - F_{B,2}^l \langle \xi_2 \theta \rangle_{>0}^{0,l} - F_{B,3}^l \langle \xi_3 \theta \rangle_{>0}^{0,l} \right) \right] \right) \tag{B.37}$$

Though not included here, the expressions of Eq. (B.37) can be implemented in code form by generating the desired expressions using e.g., Mathematica or a similar strategy.